

**ADVANCES IN MODAL SUBSTRUCTURING OF GEOMETRICALLY NONLINEAR
ASSEMBLIES**

by

Joseph Daniel Schoneman

A thesis submitted in partial fulfillment of the requirements for the degree of

MASTER OF SCIENCE

(Engineering Mechanics)

at the

UNIVERSITY OF WISCONSIN-MADISON

2016

Date of final oral defense: 8/17/2016

This thesis is approved by the following members of the Final Oral Committee:

Matthew S. Allen, Associate Professor, Engineering Physics

Daniel C. Kammer, Professor, Engineering Physics

Joseph J. Hollkamp, Senior Aerospace Engineer, Air Force Research Laboratory

© 2016 Joseph D. Schoneman

All Rights Reserved

Abstract

The modern practice of structural dynamics is concerned primarily with linear structural models, which are ubiquitous in both academia and industry. These linear models, in conjunction with finite element modeling techniques, enable the analysis of large, complicated structures. Linear reduced order models are also commonly constructed, usually via a small set of the structure's vibration modes; such models offer extreme reductions in computational cost for only a modest compromise in accuracy. However, high performance applications, notably hypersonic aircraft, often push structures into nonlinear deflection regimes. If a system's behavior can no longer be approximated as linear—such as when a beam or a plate deforms on the order of its thickness—modern finite element methods are sufficiently advanced to accurately predict the nonlinear behavior of the structure. This capability comes at great computational cost, however, and nonlinear reduced order models are not nearly as advanced or robust as their linear counterparts.

Although the past few decades have seen the development of techniques to create low-order models of geometrically nonlinear structures, these still cannot be used at industrial scales on large, complex assemblies. A primary limitation to the creation of such nonlinear reduced order models is the large upfront cost associated with their creation; the models are constructed using a series of static load cases to determine the nonlinear force/displacement relationship, and the number of load cases required grows cubically with the number of reduced basis modes. Simple beam and plate structures can easily be modeled using just a few vibration modes and hundreds of load cases, but for complex geometries, model creation costs eventually begin to eclipse the costs required to directly simulate the time history of a full-order structure.

Nonlinear component mode synthesis techniques together with interface reduction strategies provide an opportunity to circumvent load case limitations. By creating a set of nonlinear models of simple components and assembling them in a manner analogous to the assembly of linear substructures, nonlinear models of complicated assemblies may be created. This thesis specifically examines the construction of nonlinear models involving panels supported by stiffeners, a common configuration in aerospace applications. The free-free nature of the panel in its unassembled state presents difficulties in nonlinear reduced order model construction, since the panel exhibits rigid body motion in response to a static load, and its nonlinear stiffness is dependent on attachments to the neighboring structure.

This difficulty is confronted by studying the type of component boundary conditions required to

accurately create reduced order models of assembly components. Three options are examined: Fully fixed boundaries, a statically reduced linear boundary stiffness, and the full order nonlinear stiffness from finite element analysis. Only the latter offers sufficient fidelity for the cases studied here. A further difficulty is presented when component modes which are orthogonal at the assembly level prove to be nearly linearly dependent at the subsystem level. This work proposes two approaches to alleviate such difficulties by using QR and singular value decompositions to obtain alternate load bases. Finally, reduced models based on just a subset of the linear modes included in each component are shown to offer satisfactory accuracy, a finding which expands the scope of nonlinear reduced order modeling techniques.

Contents

Abstract	i
Acknowledgments	vi
Acronyms and Abbreviations	vii
Mathematical Nomenclature	viii
1 Introduction	1
1.1 Motivation	1
1.2 Key Contributions	4
1.3 Thesis Outline	5
2 Overview of Geometric Nonlinearity	7
2.1 Geometric Nonlinearity	7
2.1.1 Nonlinear, Single-Mode Beam Model	8
2.1.2 Application to Random Excitation	12
2.1.3 Response Statistics	14
2.1.4 Case Study: Parametric Thickness Investigation	15
2.2 Nonlinear Reduced Order Models	17
2.2.1 Theoretical Background	17

2.2.2	NLROM Demonstration	21
2.3	Nonlinear Normal Modes	23
2.4	Boundary Condition Dependence	27
2.5	Motivation for Nonlinear Substructuring	29
3	Linear and Nonlinear Component Mode Synthesis	32
3.1	Linear Component Mode Synthesis	32
3.1.1	Craig-Bampton Component Mode Synthesis	33
3.1.2	Characteristic Constraint Modes	36
3.2	Extension to Geometrically Nonlinear Structures	38
3.2.1	Component-Level Nonlinearity	38
3.2.2	Nash's Form of Nonlinear Restoring Force	40
3.2.3	Assembly of Craig-Bampton/Characteristic Constraint Substructures	41
3.2.4	Nonlinear Force Definition with Alternate Basis Vectors	43
3.2.5	Error Metrics	46
3.3	MATLAB Substructuring Toolset	47
3.4	Application	52
3.5	Discussion	56
4	Case Studies in Nonlinear Substructuring	57
4.1	Simply Supported Plates	58
4.1.1	Linear Substructuring	58
4.1.2	Reference Nonlinear Model	61
4.1.3	Nonlinear Substructuring	63
4.2	Panel/Stiffener Model	69
4.2.1	Linear Substructuring	70
4.2.2	Reference Nonlinear Model	73

4.2.3	Nonlinear Substructuring	76
4.2.4	Nonlinear Substructuring with Statically Reduced Interface Stiffness	81
4.2.5	Discussion	87
4.3	Two Plate and Frame Model	88
4.3.1	Linear Substructuring	89
4.3.2	Reference Nonlinear Model	92
4.3.3	Nonlinear Substructuring	93
4.3.4	Discussion	94
4.4	Discussion and Future Prospects	95
5	Future Prospects	100
	Appendices	104
A	Characteristic Constraint Mode Example	105
B	Numerical Substructuring Verification Metrics	110

Acknowledgements

I would first like to thank my advisor, Dr. Matthew Allen, both for his guidance during my time as a graduate student and for the opportunity to work in his group as an undergraduate assistant. I also thank the additional committee members for their time and willingness to evaluate my work.

Professors Allen and Kammer, in addition to their role here, were my instructors for every course I have taken related to dynamics, for which I am extremely grateful. Dr. Hollkamp is responsible for much of the groundwork that underlies this thesis, including several MATLAB and Python codes which carry much of the computational burden of this research.

Personal thanks must also go to my wife, Emily, and our children, who have endured many periods of absence during my pursuit of my education. Their support and confidence have been invaluable in pushing me forward to the completion of this work.

Finally, I must thank the National Science Foundation for its fellowship award, without which this work would not have been possible. The official funding declaration is as follows: This material is based upon work supported by the National Science Foundation under Grant No. DGE-1256259.

Acronyms and Abbreviations

Definitions are given alphabetically.

Abaqus	Abaqus finite element software, ® ABAQUS, Inc.
ABINT	Abaqus Interface MATLAB class
CB	Craig-Bampton
CBICE	Craig-Bampton Implicit Condensation and Expansion MATLAB class
CBSS	Craig Bampton Substructuring MATLAB class
CCSS	Characteristic Constraint Substructuring MATLAB class
CMS	Component Mode Synthesis
CMS.INT	Component Mode Synthesis Integration MATLAB class
CC	Characteristic Constraint mode
DOF	Degrees of Freedom
FE/FEA/FEM	Finite Element/Finite Element Analysis/Finite Element Model
FI	Fixed Interface modes
ICE	Implicit Condensation and Expansion
IR	Inertia Relief
MATLAB	Matrix Laboratory software, ® The MathWorks, Inc.
NLROM	Nonlinear Reduced Order Model
NNM	Nonlinear Normal Mode
PSD	Power Spectral Density
RMS	Root Mean Square
ROM	Reduced Order Model

Mathematical Nomenclature

Nomenclature is given by section and order of appearance.

Section 2.1

ε_x	Axial strain
x, v	Axial and transverse coordinates
u, w	Axial and bending displacements
Π, Π_I, Π_A	Elastic potential energy; bending and axial components theoref
ρ, E, A, I, L	Density, elastic modulus, area, area moment of inertia, and length
$\mathbf{M}(x), \mathbf{N}(x); \mathbf{M}_k, \mathbf{N}_k$	Axial and bending Ritz shape functions; their k^{th} derivatives
\mathbf{u}, \mathbf{w}	Axial and bending shape function amplitudes
$k_u, k_1, k_3; f$	Condensed, linear, and cubic stiffness coefficients; applied force
m_b, m_p	Beam mass and payload mass
y, z	Base coordinate and inertial coordinate
ζ, c	Critical damping ratio and damping coefficient
S_y, S_g	Base excitation PSD ceilings; physical/gravitational acceleration
g	Gravitational acceleration
S_f	Equivalent force PSD acceleration
$\sigma_{w,l}; \sigma_{w,nl}$	Linear and nonlinear formulations of standard deviation
s, S_1, S_2	Stress and stress computation coefficients
$E[\cdot]$	Expected value operator
μ_s, σ_s, RMS_s	Stress mean, standard deviation, and root mean square

Section 2.2

$\mathbf{M}, \mathbf{K}, \mathbf{x}$	Linear mass and stiffness matrices; displacement
$\mathbf{f}_{nl}(\mathbf{x}); \mathbf{f}(t)$	Nonlinear restoring force and applied load vector
ω_i, ϕ_i	Circular natural frequency and modeshape of i^{th} mode
m	Number of retained modes in reduced order model
\mathbf{I}	Identity matrix
$\mathbf{q}, \mathbf{\Lambda}, \mathbf{\Phi}$	Modal amplitudes, modal stiffness matrix, and modal matrix
$\boldsymbol{\theta}(\mathbf{q}), \theta_r$	Modal nonlinear restoring force vector and its r^{th} component
$A_r(i, j, k), B_r(i, j)$	Cubic and quadratic polynomial stiffness coefficients

Section 2.3

$\mathbf{z}, \mathbf{g}(\mathbf{z})$	State space coordinates and system state function
$\mathbf{H}(\mathbf{z}_0, T)$	Shooting function to solve two-point boundary problem
\mathbf{z}_0, T	Initial condition and period associated with potential NNM solution
$\epsilon, \mathbf{z}_{FE}$	Periodicity error, full-order solution of initial state \mathbf{z}_0 at time T

Section 3.1

n, N	Component count/degree of freedom (DOF) count, full-order assembly
$\mathbf{M}^j, \mathbf{K}^j$	Full-order mass/stiffness matrices of the j^{th} component
\mathbf{f}^j	Forcing vector applied to the j^{th} component
\mathbf{x}^j, N^j	Displacement vector and DOF count of the j^{th} component
$\{b\}$	Boundary set of components
N_b^j	Size of boundary set for the j^{th} component
$\{i\}$	Interior set of components
N_i^j	Size of interior set for the j^{th} component
Ψ_{ib}^j	Constraint mode matrix of the j^{th} component (interior DOF only)
Ψ_{ik}^j	Fixed interface mode matrix of the j^{th} component (interior DOF only)
\mathbf{q}_k^j	Fixed interface modal amplitudes of the j^{th} component
\mathbf{T}_{CB}^j	Craig-Bampton (CB) transformation matrix of the j^{th} component
$\mathbf{M}_{CB}^j, \mathbf{K}_{CB}^j$	CB mass and stiffness matrices of the j^{th} component
N_k^j, N_b^j, N_{CB}^j	Count of fixed interface modes, constraint modes, and total DOF in the j^{th} CB model
$\hat{\mathbf{M}}_{CB}, \hat{\mathbf{K}}_{CB}, \hat{\mathbf{q}}_{CB}, \hat{\mathbf{f}}_{CB}$	Unassembled CB mass/stiffness matrices, displacement vector, and force vector
N_k, N_b, N_{CB}	Count of fixed interface modes, constraint modes, and total DOF in the assembly
\mathbf{B}	Signed boolean constraint matrix describing the assembly attachment constraints
N_{constr}, N_A	Count of constraints in the assembly and remaining DOF in the assembled system
\mathbf{L}	Unsigned boolean assembly matrix spanning the null space of \mathbf{B}
$\hat{\mathbf{M}}_A, \hat{\mathbf{K}}_A, \hat{\mathbf{q}}_A, \hat{\mathbf{f}}_A$	Assembled CB mass/stiffness matrices, displacement vector, and force vector

$\hat{\Phi}_A, \hat{\Phi}_{CB}$	Assembled and unassembled modal matrices of the assembly, in CB coordinates
\mathbf{d}	Column-wise sum of \mathbf{L} used to distinguish fixed interface and boundary DOF
$\hat{\Psi}_{CC}$	Global characteristic constraint (CC) modal matrix (boundary DOF only)
\mathbf{q}_{CC}	Characteristic constraint modal amplitudes
N_C	Count of retained characteristic constraint modes
\mathbf{T}_{CC}	CC transformation matrix
$\hat{\mathbf{M}}_{CC}, \hat{\mathbf{K}}_{CC}, \hat{\mathbf{q}}_{CC}, \hat{\mathbf{f}}_{CC}$	CC mass/stiffness matrices, displacement vector, and force vector
$\hat{\Phi}_{CC}$	Modal matrix of the assembly, in CC coordinates

Section 3.2

Φ^j, \mathbf{q}^j	FI and localized CC modal matrix and corresponding modal amplitudes
$\mathbf{f}_{nl}^j(\mathbf{x}^j)$	Nonlinear restoring force associated with the j^{th} component; physical domain
$\bar{\mathbf{M}}^j, \bar{\mathbf{K}}^j, \bar{\mathbf{f}}^j$	Transformed component mass/stiffness matrices and force vector
$\boldsymbol{\theta}^j(\mathbf{q}^j)$	Nonlinear restoring force associated with the j^{th} component; modal domain
$B_r^j(i, k)$	Quadratic restoring force coefficient associated with the r^{th} mode of the j^{th} component
$A_r^j(i, k, l)$	Cubic restoring force coefficient associated with the r^{th} mode of the j^{th} component
$\mathbf{f}_A, \mathbf{f}_B$	Load case applied to nonlinear static FEM for cubic and quadratic coefficients
f_r, f_s, f_v	Load scaling factors applied to modes r, s , and v of a structure
α_r, t	Number of thicknesses to displace a model for r^{th} mode and actual model thickness
$\beta^j(\mathbf{q}^j), \boldsymbol{\alpha}^j(\mathbf{q}^j)$	Quadratic and cubic nonlinear force vectors
$\mathbf{N}_1^j(\mathbf{q}^j), \mathbf{N}_2^j(\mathbf{q}^j)$	Component Jacobian matrices for quadratic and cubic restoring force contributions
$\hat{\mathbf{N}}_1(\hat{\mathbf{q}}_{CC}), \hat{\mathbf{N}}_2(\hat{\mathbf{q}}_{CC})$	Assembled quadratic/cubic Jacobian matrices for full structure

$\hat{\mathbf{q}}_{CC,u}, \mathbf{L}_{CC}$	Unassembled vector of FI/CC coordinates; FI/CC domain assembly matrix
$\hat{\mathbf{N}}_{1,u}(\hat{\mathbf{q}}_{CC}), \hat{\mathbf{N}}_{2,u}(\hat{\mathbf{q}}_{CC})$	Unassembled quadratic/cubic Jacobian matrices for full structure
$\{\hat{\Psi}_{\hat{b}}\}^j$	Characteristic constraint mode partition to component j
\mathbf{Y}	Nonlinear matrix of displacements obtained from finite element solution
$\mathbf{U}^j, \mathbf{S}^j, \mathbf{V}^j$	Singular value decomposition matrices
$\mathbf{U}_1^j, \mathbf{U}_2^j, \mathbf{\Sigma}^j, \mathbf{V}_1^j, \mathbf{V}_2^j$	Singular value decomposition block matrices
$\boldsymbol{\eta}^j, \mathbf{\Gamma}_{SVD}^j, \mathbf{\Gamma}_{QR}^j$	Alternate basis coordinates and transformation matrices; component j
$\mathbf{Q}^j, \mathbf{R}^j$	QR decomposition matrices
$\mathbf{Q}_1^j, \mathbf{Q}_2^j, \mathbf{R}_1^j$	QR decomposition block matrices
$\tilde{\mathbf{N}}_1^j(\boldsymbol{\eta}^j), \tilde{\mathbf{N}}_2^j(\boldsymbol{\eta}^j)$	Component Jacobian matrices computed in alternate basis space
$\epsilon_{disp}, \epsilon_{force}$	Displacement and force NLROM validation metrics

Section 4.2

\hat{a}	Set of assembled boundary degrees of freedom
$\hat{\mathbf{K}}_{\hat{b}\hat{b}}$	Stiffness matrix partition from unassembled CB stiffness matrix
$\mathbf{L}_{\hat{b}\hat{a}}$	Boundary coordinate assembly matrix partition
$\mathbf{L}_{\hat{b}\hat{a}}^{\hat{j}}$	Assembly matrix partition with j^{th} component connectivity zeroed
$\hat{\mathbf{K}}^{\hat{j}}$	Augmented stiffness matrix with component j removed
$\hat{\mathbf{K}}_b^{\hat{j}}$	Boundary stiffness observed by the j^{th} component

Chapter 1

Introduction

1.1 Motivation

Linear analysis techniques are the foundation of modern structural dynamics. Most structures behave linearly at low levels of dynamic excitation, but certain high performance applications require low mass designs to withstand high environmental loads, causing responses in the nonlinear regime. It has long been possible to compute the response of geometrically nonlinear structures in finite element software, but the computational cost is orders of magnitude higher than that for linear analysis of the same structure. State-of-the-art finite element software combined with high performance computing clusters allow for multi-physics simulations with extremely complicated models - millions of degrees of freedom - in a reasonable amount of time: several hours to several days, depending on the model complexity and physics involved. This capability is extremely powerful, but such analysis times still limit the amount of design insight which can be obtained from a model. For applications requiring hundreds or thousands of analyses, such as optimization studies or Monte Carlo uncertainty quantification, day-long simulation times are not acceptable.

Specific motivating cases include skin panels of hypersonic vehicles [1], which undergo severe thermo-acoustic loadings at cruising speeds in excess of Mach 5, as well as the ducted engine assemblies of stealth aircraft, where jet exhaust impinges directly on the structure. More recently, the spaceflight companies Blue Origin and Space Exploration Technologies Corporation have both demonstrated the recovery of suborbital and first-stage orbital boosters, respectively. As launch booster landing and reuse becomes

more prevalent, large-amplitude response of thin-walled booster structures may be a subject of increasing interest. Geometric nonlinearity is also significant in the analysis of joined-wing concepts [2], and in the behavior of extremely lightweight space structures such as solar sails [3].

Another application of interest is the “digital twin” concept under examination by the United States Air Force, which proposes the simulation of an entire aircraft over its flight history in near-real-time [4]. Full-order coupled simulation of the thermal, aerodynamic, and nonlinear structural physics of an aircraft is still barely (if at all) feasible, let alone achievable in real-time.

Nonlinear Reduced Order Models

For these and other scenarios in which rapid analysis of a structure is required, reduced order models (ROMs) are a common solution. A subset of basis vectors are used to model the structure’s dynamics in a reduced space. When the full order structure is treated as linear, a particularly convenient set of equations, which can be used to quickly produce analytical solutions in either the time or the frequency domain, result from this reduction. In the nonlinear case, numerical integration is the only generally applicable method to obtain a solution for a structure’s equations of motion. In this scenario, reducing the order of a model is of even more interest, as it dramatically reduces the cost of integration. The complication lies in accurately representing the nonlinear behavior of the full-order model in the reduced space, a task which is not straightforward to accomplish. Proper model reduction of nonlinear systems is domain-dependent and closely linked to the type of nonlinearity being modeled. In this work, large-deflection nonlinearities of thin structures are considered. The nonlinearity of interest arises when the bending of a beam or plate couples into membrane stretching along the axis of the structure; a full description of the mechanism is given in Section 2.1.

The earliest known presentation of large-deflection Nonlinear Reduced Order Modeling (NLROM) techniques is that by Nash [5] in 1977, with other early work in the field put forward by Segalman & Dorhmann [6], [7], McEwan [8], and Muravyov & Rizzi [9]. A review of work in the field was performed by Mignolet et al. [10] in 2013. Nonlinearities are usually represented as a series of quadratic and cubic terms in the modal coordinates, which are often obtained by leveraging the nonlinear analysis capabilities of commercial finite element (FE) software. A low-order subset (usually below ten) of linear modes is selected for inclusion in the NLROM; a series of nonlinear static finite element analyses then characterizes the nonlinear effects of membrane stretching. Forces (or deflections) are applied in the shapes of the selected modal basis, and the resulting deflections (or forces) from the finite element analysis are used

to determine suitable coefficients for nonlinear terms in the NLROM. The technique used for this study is given by Gordon & Hollkamp in [1] and [11], and described in further detail in Sections 2.2 and 3.2.

Component Mode Synthesis

For complicated structures, such as large structural assemblies or entire vehicles, models of each component are often created independently and later assembled to form a model of the full assembly. The Craig-Bampton (CB) technique [12], with fixed-interface modes to model internal deformations and constraint modes to model boundary deformations, is an extremely common method for so-called Component Mode Synthesis (CMS), although many other techniques exist. In the linear case, substructuring approaches are often used to enable the reuse of repeated components in an assembly, to couple numerical finite element models with experimentally-obtained representations of complex components, or to pass structural models between organizations without exposing proprietary design information. In the nonlinear case presented here, such motivations are secondary; the key objective is to use nonlinear CMS in order to obtain NLROMs that would be infeasible to construct directly from the assembled model. The computational cost of constructing an NLROM grows cubically with the number of basis vectors retained. Models containing several tens of modes become unwieldy to construct, and models containing as few as a hundred modes require so many static load cases that the NLROM is not competitive with full-order time integration, particularly when validation time and the process of selecting NLROM basis vectors is factored in.

If an assembly can be represented using a collection of lower-order NLROMs, however, then the computation requirements become quite reasonable. Kuether [13], [42], [15], demonstrated the application of nonlinear CMS techniques using several examples, most notably a pair of plates pinned about their edges and joined at a common edge. In practice, aerospace structures with fully constrained edges are rare; with the exception of pure monocoque vehicles, it is common for the thin skin panels of a craft to be supported by an underlying frame composed of stringers and longerons. Unfortunately, several challenges arise when attempting to construct a component NLROM of a skin panel that is supported by stiffeners – not only does the free-free nature of the panel in its unassembled state cause challenges for obtaining static finite element solutions, but the nonlinearity in each component is largely dependent on the stiffness of its supporting structure. To accurately model component nonlinearities, this boundary stiffness must be adequately accounted for.

1.2 Key Contributions

The main contributions of this thesis involve an extension of Kuether’s large-deformation CMS approach to models in which the nonlinear components of interest are free-free in their unassembled state. Initially, the distinction appears quite trivial; however, as shown in Chapter 4, modeling issues arise immediately when attempting a straightforward application of the techniques described in [13] to the examples considered here. To circumvent these difficulties, two key modification are presented:

- The boundary stiffness observed by a plate or beam in an assembly must be accurately represented during the NLROM construction process. Neither a fully fixed boundary nor a statically reduced linear stiffness at component interfaces were sufficiently accurate to obtain valid component NLROMs. However, retaining the exact boundary stiffnesses in the form of the full finite element model did yield satisfactory NLROMs for the nonlinear components.
- The natural basis of fixed interface modes and characteristic constraint modes (described in Chapter 3) caused fit problems for one of the models studied. This occurred due to similarity between the fixed interface and characteristic constraint vectors, which led to a poorly conditioned modal matrix and inaccurate NLROM coefficients. Alternate sets of vectors were examined and used as NLROMs bases of each example, with different basis types performing better on each structure studied. While it is not possible to declare a superior type of basis from these results, this work at least demonstrates that it is possible and sometimes necessary to use an alternate basis in constructing NLROMs.

Additionally, the use of component NLROMs with a lower order than the corresponding linear component ROM is demonstrated repeatedly and shown to yield accurate results, as judged by the nonlinear normal modes used here to study NLROM convergence. This practice does not relate directly to the issues described above, but does significantly expand the applicability of nonlinear substructuring, as the number of modes required to obtain accurate linear assembly models to a useful frequency bandwidth may be still push the limits of NLROM construction.

1.3 Thesis Outline

Chapter 2 presents an overview of several key concepts in this thesis which relate to the modeling and behavior of geometrically nonlinear structures. The fundamental mechanism underlying large-deformation geometric nonlinearity of beams and plates is discussed in Section 2.1 and investigated mathematically to derive a nonlinear, single-mode Ritz model for beams with either clamped-clamped or simply-supported boundaries. This model is used to provide further motivation for the study of nonlinear structures by comparing linear and nonlinear response predictions of a thin beam with a centrally mounted payload – as will be shown, the linear analysis significantly overpredicts both displacement and stress response levels, closing off a large portion of the design envelope that remains available when using a nonlinear formulation. The beam/payload model is used for the remainder of the chapter to demonstrate the applicability of non-intrusive NLROM techniques in Section 2.2, the use of nonlinear normal modes (NNMs) to assess NLROM convergence in Section 2.3, and the dependence of large-deflection nonlinearity on axial boundary stiffness in Section 2.4. The chapter closes with further exposition on the motivation to pursue nonlinear CMS methods in Section 2.5.

Chapter 3 provides a self-contained overview of the substructuring/CMS techniques used in this thesis. The linear theory is presented in Section 3.1, with the Craig-Bampton method and use of characteristic constraint modes for interface reduction both described. Section 3.2 provides details on NLROM construction at the component level, describes the basis switching methodology used here to simulate a structure’s nonlinear restoring force with alternate basis vectors, and describes the assembly process to incorporate each component’s nonlinearity within the full assembled model. Section 3.3 covers the MATLAB toolset used for this work, which is fairly sophisticated and should be of further use for continued work in the area of nonlinear CMS. To illustrate the utility of characteristic constraint modes to complex assemblies, Section 3.4 demonstrates Craig-Bampton component mode synthesis as applied to a multi-bay panel model with 17 components, reducing the full-order model in size from over 90,000 degrees of freedom to a mere 120.

Finally, Chapter 4 demonstrates these techniques for three example structures. Section 4.1 first reprises Kuether’s two-plate model from [13] and [14], which has available “truth” NNMs and is used to validate the alternate-basis and low-order NLROM methods used here. Section 4.2 presents a simple, three-component assembly of a thin beam mounted on two stiffeners, demonstrates the fundamental issues associated with modeling such a structure, and examines a series of possible remedies. Once a

working method on this model is demonstrated, the chapter continues with Section 4.3, which moves to a more geometrically complicated example with two plates and an underlying frame structure.

Chapter 5 concludes the thesis with speculation on avenues for future research in the area of non-linear component mode synthesis.

Chapter 2

Overview of Geometric Nonlinearity

This chapter presents an overview of large-deflection geometric nonlinearity as it pertains to thin beams and plates. A qualitative description of the nonlinear mechanism is first shown, followed by a mathematical exposition of axial/bending coupling in an Euler-Bernoulli beam, which is used to demonstrate the physics of interest. A more generally applicable form of nonlinear reduced order model, based on non-intrusive use of commercial finite element codes, is then discussed. The concept and computation of the nonlinear normal mode, which has applications in many different types of nonlinear systems, is described in Section 2.3; application of the NNM to the nonlinear structures of interest in this work is also described. Finally, the effect of boundary condition stiffness on axial/bending nonlinearity is covered in Section 2.4; this topic is of particular importance for the results shown in Chapter 4. To conclude the chapter, Section 2.5 describes the motivation for pursuit of nonlinear substructuring techniques.

2.1 Geometric Nonlinearity

The term “geometric nonlinearity” is broad and can refer to any of several phenomena, all of which behave in distinct manners. In this work, the nonlinearity of interest arises from coupling between axial and bending motions in thin beams and plates. As a thin member deforms on the order of its thickness, the overall change in length induces axial deformations, known as “membrane stretching.” A schematic is given for a clamped-clamped beam in Figure 2.1. In beam structures, membrane stretching is entirely a result of the fixed boundaries, and as such only beams which are axially constrained will exhibit this type of large-deformation nonlinearity. For plates, the situation is more complicated, and bending/axial

coupling is present even in the free-free case – see, for instance, the work of Touzé et al. [16] related to the nonlinear dynamics of gongs.

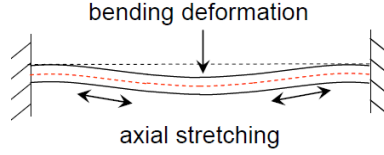


Figure 2.1: *Illustration of axial stretching effects for a clamped-clamped beam. At low deflections, deformation along the neutral axis is negligible; as the deflection increases towards one beam thickness, the axial deformation increases nonlinearly and must be included in the analysis.*

For perfectly flat structures, the membrane stretching behavior is “stiffening” in nature, such that the restoring force is larger than what would be expected from a linearized model. This has various ramifications for performance of thin structures. Most obviously, the actual displacement of a thin, flat structure will be significantly lower than that predicted with a linear model. Since the nonlinearity affects the structure’s restoring force, the resonant frequency will also change as a function of amplitude. Additionally, various bending modes of a structure may couple together through the membrane motions, leading to excitations at frequencies that would not be predicted by linear analysis. These latter two phenomena are best discussed in the context of the nonlinear normal mode, which is formally defined in Section 2.3. Before proceeding, however, the nonlinear stiffening of a beam due to membrane stretch in a single mode will be examined mathematically.

2.1.1 Nonlinear, Single-Mode Beam Model

The objective here is to demonstrate basic aspects of the nonlinear behavior of thin beams via a single-mode Ritz/Galerkin model. It should be emphasized that the nonlinear reduced order models used later in this thesis are generated using non-intrusive methods to interrogate full-order finite element models; the Ritz model developed in this section is used for demonstration only. Other examples of the application of Ritz/Galerkin methods to model nonlinear structures are numerous and include, for example, the modeling of a nonlinear plate by Barone et al. (very similar to the model constructed below) in [17], modeling of cylindrical shells by Amabili et al. in [18], and the aforementioned work of Touzé [16].

As a starting point, take the nonlinear Green-Lagrange measure of axial strain in an Euler-Bernoulli

beam [19].

$$\varepsilon_x = \frac{du}{dx} - v \frac{d^2w}{dx^2} - \frac{1}{2} \left(\frac{du}{dx} - v \frac{d^2w}{dx^2} \right)^2 - \frac{1}{2} \left(\frac{dw}{dx} \right)^2 \quad (2.1)$$

Here, x is the axial coordinate, v the transverse coordinate along the beam section, w the transverse (bending) displacement and u the axial (membrane) displacement. Under the von Kármán kinematic assumption, axial deformations and curvature are small compared to bending rotation, an assumption expressed mathematically as $\frac{1}{2} \left(\frac{du}{dx} - v \frac{d^2w}{dx^2} \right)^2 \simeq 0$. This leads to the quadratic strain equation,

$$\varepsilon_x = \frac{du}{dx} - v \frac{d^2w}{dx^2} - \frac{1}{2} \left(\frac{dw}{dx} \right)^2 \quad (2.2)$$

with the final term the source of nonlinearity in the beam. The elastic potential energy Π of an Euler-Bernoulli beam depends only on the axial strain,

$$\Pi = \frac{1}{2} \int_0^L \int_A \varepsilon_x^T E \varepsilon_x dA dx \quad (2.3)$$

with L the beam length, A the cross-sectional area, and E the elastic modulus of the beam material. For the following discussion, A and E are assumed constant along the length of the perfectly flat beam. Substituting (2.2) into (2.3), evaluating the area integrals, and collecting terms leads to

$$\Pi = \Pi_I + \Pi_A = \frac{EI}{2} \int_0^L \left[\frac{d^2w}{dx^2} \right]^2 dx + \frac{EA}{2} \int_0^L \left[\left(\frac{du}{dx} \right)^2 + \frac{1}{4} \left(\frac{dw}{dx} \right)^4 - \frac{du}{dx} \left(\frac{dw}{dx} \right)^2 \right] dx \quad (2.4)$$

The first term Π_I is the potential energy for the linear case of a beam in bending, and the first term within the integrand of Π_A is the potential energy for a linear, axially loaded bar. Of more interest is the quartic term $\frac{1}{4} \left(\frac{dw}{dx} \right)^4$ and in particular the term $\frac{du}{dx} \left(\frac{dw}{dx} \right)^2$, which causes coupling between bending and axial displacements.

To continue, write the axial and transverse displacements in terms of shape functions such that $u(x) = \mathbf{M}(x)\mathbf{u}$ and $w(x) = \mathbf{N}(x)\mathbf{w}$. These should be considered global shape functions of the structure, i.e. we are pursuing the Ritz/Galerkin method rather than the finite element method. The k^{th} derivative of each shape function with respect to x is denoted by \mathbf{N}_k or \mathbf{M}_k (with the explicit dependence upon x

omitted). For each potential energy term,

$$\begin{aligned}\Pi_I &= \frac{EI}{2} \int_0^L \mathbf{w}^T \mathbf{N}_2^T \mathbf{N}_2 \mathbf{w} dx \\ \Pi_A &= \frac{EA}{2} \int_0^L \left[\mathbf{u}^T \mathbf{M}_1^T \mathbf{M}_1 \mathbf{u} + \frac{1}{4} \mathbf{w}^T \mathbf{N}_1^T \mathbf{w}^T \mathbf{N}_1^T \mathbf{N}_1 \mathbf{w} \mathbf{N}_1 \mathbf{w} - \mathbf{u}^T \mathbf{M}_1^T (\mathbf{w}^T \mathbf{N}_1^T \mathbf{N}_1 \mathbf{w}) \right] dx\end{aligned}\quad (2.5)$$

Due to the coupling inherent in Π_A , it is possible to write the membrane stretching as a function of bending displacement. This is achieved by minimizing Π_A with respect to \mathbf{u} ; inverting to find \mathbf{u} in terms of \mathbf{w} leads to

$$\mathbf{u} = \left[\int_0^L \mathbf{M}_1^T \mathbf{M}_1 dx \right]^{-1} \int_0^L \mathbf{M}_1^T \mathbf{w}^T \mathbf{N}_1^T \mathbf{N}_1 dx \mathbf{w} = \mathbf{K}_u \mathbf{w} \quad (2.6)$$

This process is known as a “condensation” of the axial displacements. A conceptually similar but more general procedure for condensing the axial displacements of complex structures will be discussed in Section 2.2. When considering the full dynamic equations of motion with mass terms included, the condensation process neglects axial accelerations $\ddot{\mathbf{u}}$ as small compared to their transverse counterparts; in practice, this is an acceptable assumption. The matrix \mathbf{K}_u is a linear function of \mathbf{w} but does not depend on \mathbf{u} , only the selected shape functions for the structure. Using (2.6) to eliminate \mathbf{u} , the elastic potential energy terms become

$$\Pi_I = \frac{EI}{2} \int_0^L \mathbf{w}^T \mathbf{N}_2^T \mathbf{N}_2 \mathbf{w} dx$$

$$\Pi_A = \frac{EA}{2} \int_0^L \left[\mathbf{w}^T \mathbf{K}_u^T \mathbf{M}_1^T \mathbf{M}_1 \mathbf{K}_u \mathbf{w} + \frac{1}{4} \mathbf{w}^T \mathbf{N}_1^T \mathbf{w}^T \mathbf{N}_1^T \mathbf{N}_1 \mathbf{w} \mathbf{N}_1 \mathbf{w} - \mathbf{w}^T \mathbf{K}_u^T \mathbf{M}_1^T (\mathbf{w}^T \mathbf{N}_1^T \mathbf{N}_1 \mathbf{w}) \right] dx$$

The derivatives of potential energy with respect to \mathbf{w} are difficult to write for an arbitrary number of coordinates. If, however, only a single mode is assumed for each of $u(x)$ and $w(x)$, then the expressions can be further simplified. Designating w as the sole component of \mathbf{w} , the linear stiffness k_1 and cubic

stiffness k_3 are written in terms of the axial coupling term k_u as

$$\begin{aligned} k_u &= \frac{1}{2} \frac{\int_0^L M_1 N_1^2 dx}{\int_0^L M_1^2 dx} \\ k_1 &= EI \int_0^L N_2^2 dx \\ k_3 &= 2EA \int_0^L \left(k_u^2 M_1^2 + \frac{1}{4} N_1^4 - k_u M_1 N_1^2 \right) dx \end{aligned} \quad (2.7)$$

with a static displacement equation in response to a force f given in the form of a Duffing oscillator;

$$k_1 w + k_3 w^3 = f \quad (2.8)$$

This leads to the final difficulty: While bending shape functions are routinely tabulated in handbooks for beams with various boundary conditions, the shape functions corresponding to their coupled membrane deflections are not obvious. For this purpose, the finite element method is useful. By applying a load in the shape of the first bending mode of a beam and extracting the resultant axial deformations, the membrane deflection shape can be inferred. This procedure is demonstrated in Figure 2.2 for a simply-supported and clamped-clamped beam.

The simply-supported beam can be represented using the well-known bending modeshape $N(x) = \sin(\frac{\pi x}{L})$, with an axial deflection shape $M(x) = \sin(\frac{2\pi x}{L})$ that is just in simple in form. Inserting these functions into (2.7) and evaluating the integrals using MATLAB's symbolic software routine leads to analytical results for the stiffness coefficients, with the expected linear coefficient as $k_1 = \frac{EI\pi^4}{2L^3}$ and a nonlinear coefficient of $k_3 = \frac{AE\pi^4}{8L^3}$. This value is identical to that obtained independently, using alternate methods, by Senturia [20] and Grappasonni [21], for a *clamped-clamped* beam, which is initially disconcerting. Applying the present method to the clamped-clamped case is not as simple, and the approximating modeshapes $N(x) = \frac{1}{2}(1 + \cos(2\pi x/L))$ and $M(x) = \sin(4\pi x/L)$ were too complicated to yield analytical integrals in (2.7). However, numerically evaluating the resultant expression for k_3 led to coefficients which precisely matched the analytical expression obtained for the simply-supported beam, $k_3 = \frac{AE\pi^4}{8L^3}$. Using this model, both the clamped-clamped and simply-supported beam configurations yield identical nonlinear stiffness coefficients, despite the free bending coordinate at the boundaries of the latter case.

Referring to the quadratic strain expression in (2.2), strain in the beam can be written in terms of

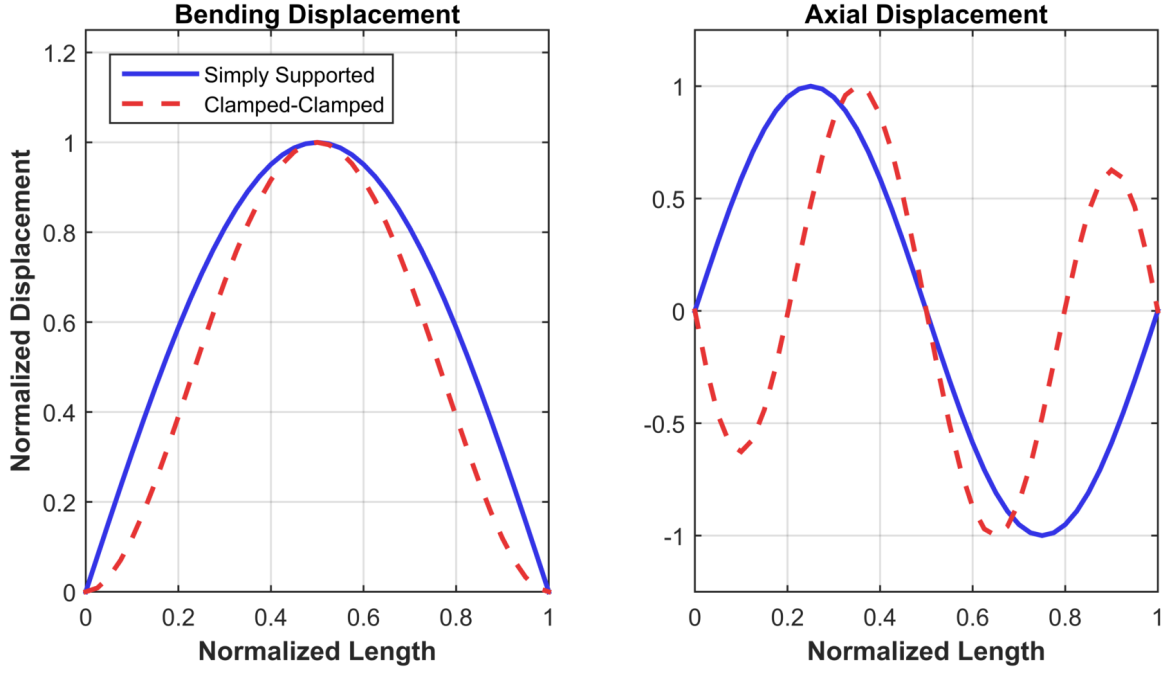


Figure 2.2: *First mode bending deformations (left) and associated membrane deformations (right) for a simply-supported and clamped-clamped beam, obtained by applying a load in the shape of the first bending mode to a nonlinear finite element model of each structure and examining the resultant deformations.*

the bending coordinate w and shape function derivatives as

$$\varepsilon(x) = (M_1 k_u + \frac{1}{2} N_1^2) w^2 - v N_2 w \quad (2.9)$$

By evaluating the selected shape function derivatives at $x = L/2$ and the appropriate value of v , the maximum stress in the beam is easily obtained. Due to the axial stretch, the stress profile across the beam is not antisymmetric, but will be higher on the tensioned side of the beam.

2.1.2 Application to Random Excitation

With an expression for the nonlinear restoring force of a beam available, a random excitation load case is now examined to demonstrate the effect of nonlinearity on the response. A base excitation scenario with a centrally mounted payload on the clamped-clamped beam is considered; see Figure 2.3 for a relevant schematic. The bending displacement w is now defined relative to an inertial coordinate z and base

coordinate y as $w = z - y$, so that the structure's equation of motion is

$$(m_b + m_p)\ddot{y} + c\dot{w} + k_1w + k_3w^3 = 0 \quad (2.10)$$

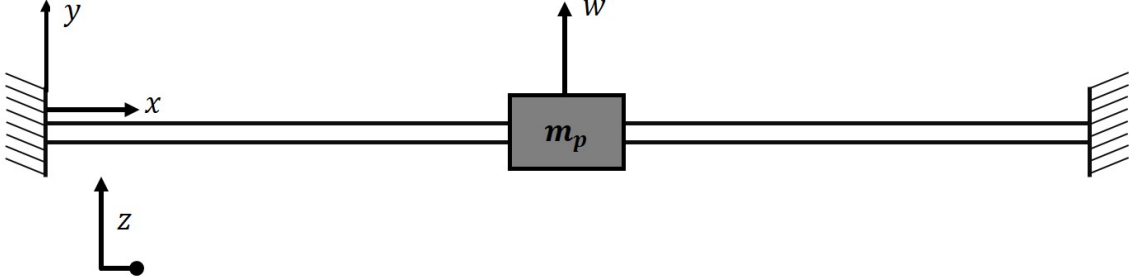


Figure 2.3: Diagram of the base-excitation scenario considered in this section. The beam bending coordinate is w , the base motion coordinate is y , and the inertial coordinate is z ; x corresponds to axial position along the beam.

The effective beam mass is $m_b = \rho A \int_0^L N(x)^2 dx = \frac{3\rho AL}{8}$ for the clamped-clamped beam. The damping coefficient is defined in terms of an assumed modal damping ratio ζ of the beam only, with no payload included, as $c = 2\zeta\sqrt{k_1 m_b}$, and the linear stiffness from (2.7) is $k_1 = \frac{2EI\pi^4}{L^3}$. The nonlinear stiffness remains $k_3 = \frac{AE\pi^4}{8L^3}$. Finally, m_p is the mass of the centrally mounted payload. Re-arranging (2.10) to move the base excitation to the right-hand side leads to

$$(m_b + m_p)\ddot{w} + c\dot{w} + k_1w + k_3w^3 = (m_b + m_p)\ddot{y} \quad (2.11)$$

The base excitation \ddot{y} is defined as a broadband, stationary, Gaussian random process with zero mean and a power spectral density (PSD) ceiling of S_y . The PSD is defined as single-sided with units of acceleration squared per Hertz. For convenience, it is common to specify a PSD ceiling S_g in terms of gravitational acceleration g , in which case $S_y = S_g g^2$ yields the correct forcing level. The resultant PSD ceiling S_f of the equivalent applied force then becomes $S_f = S_g [g(m_b + m_p)]^2$; it is this PSD ceiling which will be of interest in finding the statistics of w from (2.11).

2.1.3 Response Statistics

In the linear case, for $k_3 = 0$, the stationary response will display a Gaussian probability distribution with zero mean and a variance of $\sigma_{w,l}^2 = \frac{S_f}{4k_1c}$ [22]¹. The nonlinear case is, of course, more involved, but a statistical linearization procedure can be used to yield a compact solution. The essence of the statistical linearization method involves assuming that the nonlinear response displays a Gaussian probability distribution and using this assumption to determine the moments of the stationary response. While the resulting moments are often quite accurate, their practical use is hampered by the fact that the true response is not actually Gaussian, thus, common techniques to approximate the likelihood of rare events are not directly applicable. However, the procedure is instructive for purposes of demonstration. Under these assumptions, the nonlinear response of (2.11) is again zero-mean, with a variance given by

$$\sigma_{w,nl}^2 = \frac{k_1}{6k_3} \left[\left(1 + \frac{3k_3 S_f}{ck_1^2} \right)^{1/2} - 1 \right] \quad (2.12)$$

These results can now be used to determine the associated stress statistics, using the strain expression of (2.9). Defining the coefficients $S_1 = -vN_2$ and $S_2 = E(M_1 k_u + \frac{1}{2} N_1^2)$, the stress as a function of bending displacement becomes $s(w) = S_1 w + S_2 w^2$, where s is used for stress rather than the customary σ to avoid confusion with the definitions of variance given above. Note that, in the linear case, S_2 is not defined and the expression is simply linear in w . Taking the expectation of the stress yields

$$E[s(w)] = E[S_2 w^2 - S_1 w] = S_2 E[w^2] - S_1 E[w] = S_2 \sigma_w^2 = \mu_s \quad (2.13)$$

Even though both linear and nonlinear displacement responses are zero-mean, the nonlinear stress has a nonzero mean value. This is a result of the membrane stretching, which yields a positive stress value for both positive and negative values of bending deformation. The stress variance is computed from the second central moment,

$$E[(s(w) - \mu_s)^2] = E[s(w)^2] - (\mu_{s,nl})^2 = E[S_2^2 w^4 + 2S_1 S_2 w^3 + S_1^2 w^2] - (S_2 \sigma_w^2)^2$$

Arriving at (2.12) required an assumption that the response was normally distributed. Applying

¹Both this result and that for the nonlinear case can be found from Example 10.7, page 442 of the reference. Note that Lutes and Sarkani use the convention of a two-sided PSD with units of radians per second in the denominator. If a PSD ceiling given using this convention is denoted as \hat{S}_0 , then the relevant conversion is $S_0 = 4\pi\hat{S}_0$

this property to the stress response as well yields $E[w^4] = 3\sigma_w^4$ and $E[w^3] = 0$, leading to a variance of

$$\sigma_s^2 = 3S_2^2\sigma_w^4 + (S_1^2 - S_2^2\sigma_w^2)\sigma_w^2 \quad (2.14)$$

Finally, the root mean square (RMS) stress is given by $RMS_s = \sqrt{\mu_s^2 + \sigma_s^2} = \sqrt{3S_2^2\sigma_{X,nl}^4 + S_1^2\sigma_{X,nl}^2}$. Again, the linear counterpart to all of these quantities can be obtained by setting $S_2 = 0$, indicating that the linear stress distribution is zero-mean with a variance of $S_1^2\sigma_w^2$.

2.1.4 Case Study: Parametric Thickness Investigation

With analytical expressions for the linear and nonlinear response statistics available, a parametric study with respect to any of the beam's parameters is easily performed. Thickness is the variable of interest here; reducing the thickness not only reduces the mass of the structure, but also serves to emphasize the nonlinear behavior of the beam for a given load level. Key numerical parameters of the scenario considered here are given in Table 2.1. The structure is subjected to a base excitation with a PSD ceiling of $0.32 \text{ } g^2/Hz$, roughly corresponding to the maximum level experienced within the main bay of the Space Transport System (Space Shuttle). Thickness values considered range from 0.5 to 4 mm.

Length [mm]	Width [mm]	Payload Mass [g]
250	25	50
Density [kg/mm ³]	Young's Modulus [MPa]	Fatigue Limit [MPa]
2700	71,000	95

Table 2.1: *Basic parameters of the configuration, shown in Figure 2.3, used for the parametric study below.*

To quantify the resulting design difference between a linear and nonlinear prediction of stress in the beam, a crude performance criteria is established: Two standard deviations of the predicted stress must remain below the material fatigue limit, so that the alternating stress within the beam remains below the limit roughly 95% of the time. Figure 2.4 displays stress and displacement curves as a function of thickness for both the linear and nonlinear formulations.

With its overprediction of response, the linear stress prediction closes off a large portion of the design envelope which is available when using the nonlinear stress prediction. As a result, the linear beam design requires a thickness of 2.44 mm to meet the stress requirements, while the nonlinear design requires only a 1.07 mm thickness – a 56% reduction. Observe that the linear design has still entered the

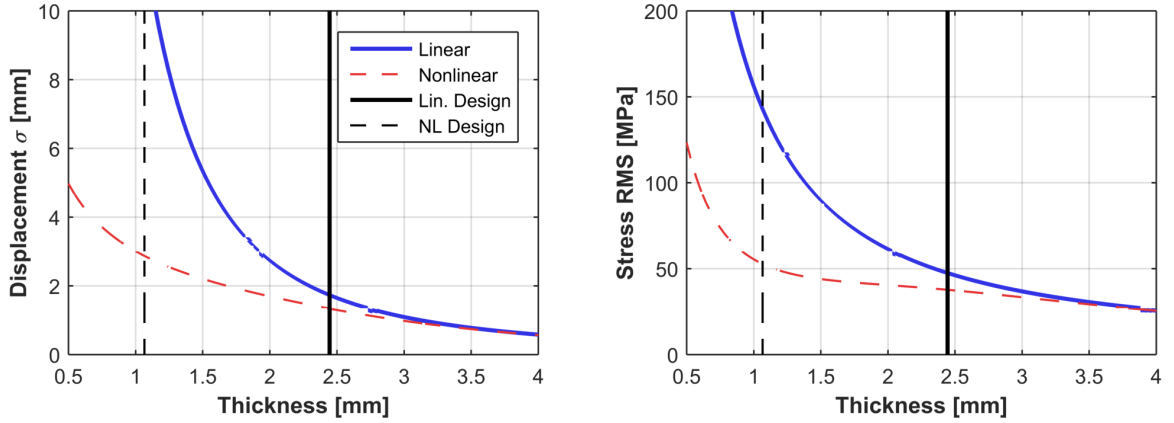


Figure 2.4: Displacement standard deviation and stress RMS for the linear and nonlinear models. Vertical lines correspond to the thickness at which two standard deviations of stress reach the material fatigue limit.

nonlinear deflection regime to some extent, and that if a deflection constraint was placed on the beam so that it remained in the linear regime (by limiting the deflection relative to the thickness, or stipulating a limit on the natural frequency shift under loading), the linear beam design would be even thicker.

To a certain extent, this nonlinear behavior allows designers to make tradeoffs between weight, displacement, and stress. Whereas the nonlinear displacement in Figure 2.4 grows in a more or less linear manner between the thicknesses of 1 and 3 mm, growth of the stress RMS curve levels off almost entirely. In this portion of the design envelope, a reduction in thickness will increase the displacement an appreciable amount while only increasing the stress slightly. Further, this analysis shows that the beam stress is much less sensitive to small variations in thickness than would be expected from a linear analysis. Of course, even if displacement, rather than stress, is the design constraint of interest, the nonlinear formulation still provides much more available design envelope than the linear equations.

It is also instructive to examine the growth of the stress mean and variance separately, as shown in Figure 2.5. At thicknesses below 3.5 mm, the linear and nonlinear predictions begin to diverge, and a nonzero mean stress develops. As the thickness drops further, the linear RMS curve increases more quickly than the mean stress curves, leading to a much lower RMS curve for the nonlinear structure. Recalling that the mean stress corresponds to membrane stretching of the beam, this result has a clear physical explanation: The uniform membrane strain along the beam cross section allows for a much more efficient distribution of strain energy than the linear, antisymmetric strain distribution that results from bending. As such, from roughly 2.5 mm to 1.5 mm, stress is apportioned preferentially to the membrane of the beam, with almost no growth in the alternating stress due to bending. Put more simply, at low

enough levels of thickness, the beam begins to behave in a manner similar to a cable, accepting loads along its axis. Below 1.5 mm, both the mean and standard deviation curves begin to increase in tandem once more.

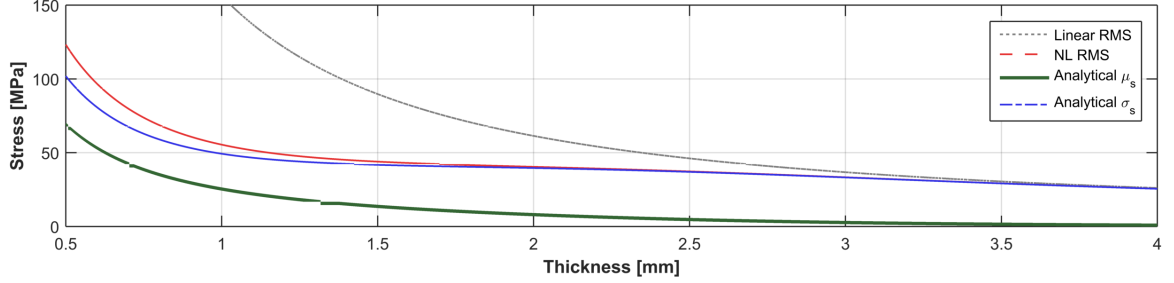


Figure 2.5: Overall RMS stress values of the linear and nonlinear predictions, along with stress mean and standard deviation from the nonlinear predictions.

2.2 Nonlinear Reduced Order Models

All of the above analysis was the result of a simple one-mode Ritz model coupled with basic statistical linearization techniques. To obtain more accurate multi-mode models on more complicated geometries, a general procedure for obtaining nonlinear reduced order models is necessary. In this work, such models are obtained through non-intrusive coupling with the Abaqus nonlinear finite element code. “Non-intrusive” in this context indicates that the FE program is treated as a “black box,” with no access to the internals of the code possible. This situation is intended to represent a commercial environment in which access to specialized internal codes is often limited, and off-the-shelf software is the only available option for analysis.

2.2.1 Theoretical Background

Extraction of a structure’s linear mass and stiffness matrix is a routine practice in modern finite element codes. Deflection-dependent geometric nonlinearities are another matter, however; at best, a tangent stiffness matrix corresponding to a given deformation may be obtained. Rather than use the tangent stiffness matrix to formulate the structure’s nonlinear equations directly, an indirect approach is taken to obtain a useful expression for the nonlinear restoring force. Begin from the conservative full-order

equations of motion for the structure,

$$\mathbf{M}\ddot{\mathbf{x}} + \mathbf{K}\mathbf{x} + \mathbf{f}_{nl}(\mathbf{x}) = \mathbf{f}(t) \quad (2.15)$$

where \mathbf{M} and \mathbf{K} are the system's mass and stiffness matrices, \mathbf{x} is the system deflection (the double overdot denoting second time derivative), $\mathbf{f}(t)$ is an applied external load, and $\mathbf{f}_{nl}(\mathbf{x})$ represents the nonlinear restoring force. The system is transformed to reduced modal space using a subset of m normal modes ϕ_i which satisfy $[\mathbf{K} - \omega_i^2 \mathbf{M}]\phi_i = 0$ and are scaled such that $\phi_i^T \mathbf{M} \phi_i = \mathbf{I}$. For simple beams and plates, m less than 10 is often sufficient – as discussed below, the complexity of the NLROM construction is cubic with respect to m , and can quickly become intractable for large numbers of modes. The transformed equations of motion are

$$\ddot{\mathbf{q}} + \mathbf{\Lambda}\mathbf{q} + \boldsymbol{\theta}(\mathbf{q}) = \boldsymbol{\Phi}^T \mathbf{f} \quad (2.16)$$

with the transformation defined such that $\mathbf{x} = \boldsymbol{\Phi}\mathbf{q}$ and the transformed stiffness matrix $\mathbf{\Lambda}$ is simply a diagonal matrix containing the square of each mode's circular natural frequency, ω_i^2 , on the corresponding diagonal element. The force vector $\boldsymbol{\theta}(\mathbf{q})$ is the modal analogue of the nonlinear restoring force vector; each force component is represented as a combination of quadratic and cubic polynomials in the modal coordinates – this approach is justified when the FE model uses linear elastic materials and the geometric nonlinearities are derived using quadratic strain-displacement relationships [11]. Recall the quadratic strain-displacement relationship of (2.2), which led to a model with a single cubic term; more generally, quadratic terms will appear as well. The r^{th} term in the nonlinear restoring force is written as

$$\theta_r(q_1, q_2, \dots, q_m) = \sum_{i=1}^m \sum_{j=1}^m B_r(i, j) q_i q_j + \sum_{i=1}^m \sum_{j=1}^m \sum_{k=1}^m A_r(i, j, k) q_i q_j q_k \quad (2.17)$$

The arrays A_r and B_r contain cubic and quadratic stiffness coefficients of the nonlinear model; specification of these values forms the essence of the NLROM. Two main approaches are used to determine these coefficients, the “Enforced Displacements” technique and the “Implicit Condensation and Expansion” (ICE) approach. While only the latter is used in this work, both are briefly described below.

Enforced Displacements

The enforced displacement procedure, described by Muravyov and Rizzi in [9], applies a set of displacement shapes to the full-order finite element model, extracts the nodal constraint forces required to maintain the desired shape, and uses the results to formulate a system of *linear equations* in the polynomial coefficients of (2.17). Each displacement shape is a combination of the sums and differences of one, two, or three of the modeshapes in the structure’s modal basis, with the displacement shape scaled such that the structure’s nonlinearity is sufficiently excited. (One thickness of displacement is often used as a general rule.)

Construction of accurate models using the enforced displacement procedure requires a basis set which includes membrane modes of the structure. Locating a particular high-frequency axial mode from a finite element model is a laborious process; instead, the “dual mode” of a particular low-frequency computed can be computed directly and used within the nonlinear basis [23]. Put simply, the dual mode ϕ_d of a bending mode ϕ_b corresponds to the membrane deformations associated with a static, nonlinear FE solution to a load proportional to ϕ_d . For a set of m modes, the enforced displacement procedure requires, per [10],

$$2m + \frac{3m!}{2(m-2)!} + \frac{m!}{6(m-3)!} = \frac{1}{6} (m^3 + 6m^2 + 5m)$$

static load cases, for a cubic order of growth with the number of modes in the basis. A key example of the application of enforced displacement Perez et al. can be found in [24]; in that work, a 90,000 degree-of-freedom multi-bay-panel was accurately modeled using an NLROM containing 49 linear bending modes and 36 dual modes.

Implicit Condensation and Expansion

The ICE method, which may also be referred to as the “applied loads” method, is the conceptual inverse of the enforced displacement method. A series of static loads are applied to the full order finite element model (FEM), each one containing combinations of up to three of the NLROM basis vectors. Were the structure linear, this would cause a deformation in the associated modes only. Due to the nonlinearity, however, the applied force excites a response in other modes of the structure, allow the restoring force coefficients to be determined. Kuether, Brake, and Allen [25] showed that an effective rule of thumb for

selecting force amplitudes is to scale them such that the nonlinear static FE solution deflects 15 to 20 percent less (more) than a purely linear static solution due to the hardening (softening) characteristic of the nonlinearity. Then, the nonlinear response of the structure is obtained from the FE software. This response is used to form a *least squares problem* in terms of the stiffness coefficients, which is solved to find the required coefficients.

Since the finite element program is solving an applied loads problem, the membrane deformations associated with a particular bending mode are implicitly captured and condensed into the basis. As a result, no membrane modes need be included in the basis, which both simplifies the process of basis selection and reduces the number of load cases required to specify the NLROM. Full identification of the coefficients using ICE requires

$$2m + \frac{2m!}{(m-2)!} + \frac{4m!}{3(m-3)!} = \frac{2}{3} (2m^3 - 3m^2 + 4m)$$

static load cases.

A full explanation of the ICE fit process as it pertains to components of a substructure is given in Section 3.2; a description concerning the construction of monolithic NLROMs is omitted here but may be found in [26].

Comparison of Methods

The enforced displacement and ICE methods may seem nearly equivalent to the casual observer, however, a number of subtle differences have significant implications for the analyst. First, finite element analysis using a displacement-controlled procedure is inherently more stable than a force-controlled analysis, meaning the static load cases of the enforced displacement method are less likely to encounter convergence difficulties than their ICE counterparts. Second, the linear system of equations resulting from enforced displacement is also easier to solve and usually better-conditioned than the corresponding least squares procedure of ICE. In terms of number of load cases required to specify the model, the ICE method may seem to have an advantage, as membrane modes are not be included in the basis. However, this is offset by the much more rapid growth in load case count for the ICE method, as shown in Figure 2.6. For example, the multi-bay panel mentioned above would require 109,650 load cases to specify all 89 modes using the basic enforced displacement technique. Assuming that an equivalent NLROM could be generated using ICE with only the 49 bending modes identified by Perez, 152,194 load cases would be

required.

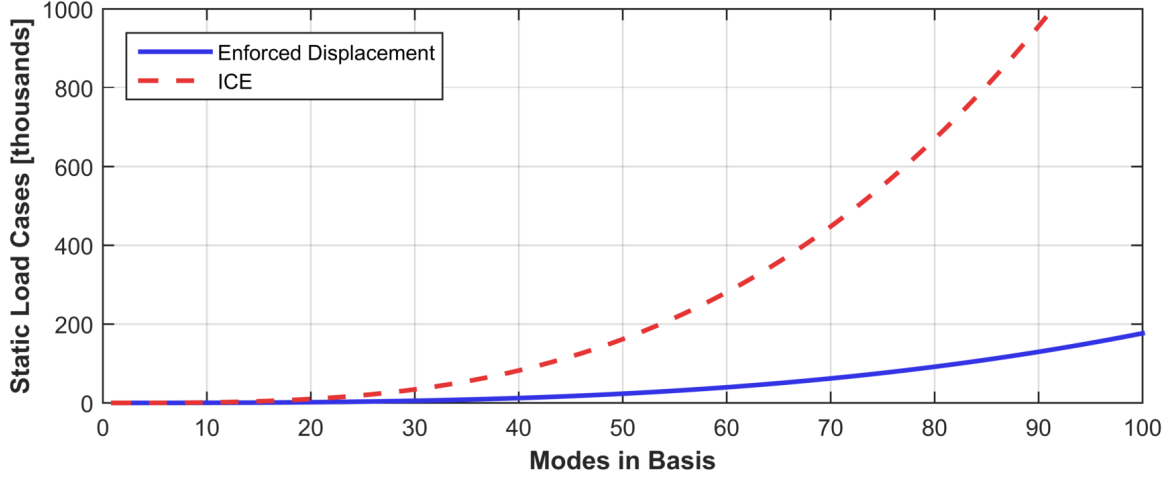


Figure 2.6: *Number of nonlinear static load cases required to specify an NLROM using the enforced displacement and the ICE methods.*

Despite these disadvantages, the ICE method is usually much easier to apply to a given structure, requiring no consideration of dual modes. Further, “cleaning” procedures are often applied to NLROMs generated with enforced displacement, as described in [27]. This procedure entails zeroing out any cubic and quadratic terms which involve only a single membrane mode of the structure, and further complicates the construction process. Since this work is focused on substructuring a collection of relatively simple subcomponents, the straightforward application of the ICE method was selected over the more sophisticated analysis required to apply the enforced displacement procedure.

2.2.2 NLROM Demonstration

To demonstrate the application of some simple nonlinear reduced order models, the beam from Figure 2.3 was meshed in Abaqus using 40 B32 quadratic beam elements, with the payload represented as a point mass at the beam center. A thickness of 1.07 mm, corresponding to the nonlinear design point of Figure 2.4, was specified. A one-mode NLROM containing the first mode only was constructed along with a three mode NLROM containing modes 1, 3, and 7, which were the first three in-plane symmetric modes of the structure. (Modes 2 and 6 were symmetric and not affected by the uniform base excitation, mode 4 was axial motion of the payload, and mode 5 was the first out-of-plane bending mode.) These two models, along with a model using the analytical coefficients from Section 2.1, were simulated using Newmark time integration over a period of 100 seconds. The base excitation power spectrum was cut

off at 500 Hz, well past the beam's first natural frequency of 31.2 Hz. Power spectral densities of the midpoint response for each model, along with that predicted from a linear model of the beam, are shown in Figure 2.7. Key properties of each model and statistics of each response are given in Table 2.2. Based on past experience, the multi-mode NLROM containing the first few symmetric bending modes is sufficiently accurate to replicate the response that would be obtained from a full-order simulation, to include the stresses in the beam (see, for example, the investigation conducted in [28]). As such, an expensive full-order simulation of the structure was not performed for this demonstration.

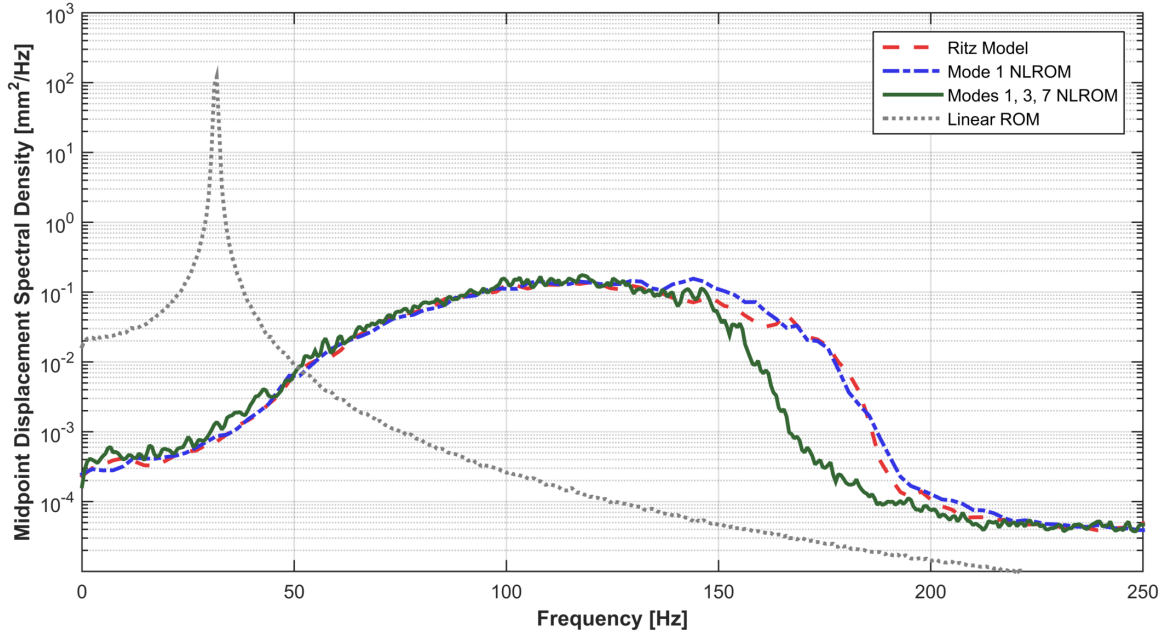


Figure 2.7: *Power spectral densities of the analytical Ritz model from Section 2.1, two NLROMs constructed from a full-order finite element model, and a linearized model of the beam and payload system.*

Key characteristics of a nonlinear structure's response to random loading are observable here. Most critically, the peak spectral density of the nonlinear response is three orders of magnitude lower than that of the linear response prediction. Additionally, the nonlinear responses have all spread significantly in frequency, as if damping in the structure had increased significantly. The spread is a result of the nonlinear stiffness in the system, rather than added damping – one might think of the structure's instantaneous natural frequency as a random function of time, the envelope of which is represented by the spread power spectrum. Also note that stiffening in the structure has shifted the overall resonance from the linear natural frequency by a factor of four. As a result of these phenomena, the nonlinear response standard deviations are one quarter that of the linear result.

Comparing the different nonlinear models, the two single-mode predictions appear quite similar to

Model	k_2	k_3	Stat. Lin σ_w [mm]	Numerical σ_w [mm]
Ritz	–	1.480	2.864	3.025
Mode 1 NLROM	-1.631E-03	1.388	2.910	3.245
Modes 1, 3, 7 NLROM	-2.456E-03	1.362	2.923	3.046
Linear ROM	–	–	11.933	12.441

Table 2.2: *Key parameters of each model simulated to obtain the spectral densities in Figure 2.7. The k_2 and k_3 coefficients correspond to stiffness values for the first bending mode as given in Equation (2.10). The “Stat. Lin” column corresponds to computation made using the statistical linearization approach of Eq. (2.12), neglecting the insignificant k_2 values for each NLROM model. Recall that σ_w refers to the standard deviation of the bending coordinate w .*

each other, although the statistics of each response are somewhat different. The multi-mode NLROM occupies a significantly reduced space along the frequency axis, and has a lower overall variance. It is believed that this behavior is a result of energy transfer to higher modes of the system, although a precise understanding of such phenomena is still an area of active research. Table 2.2 supports this hypothesis: The three-mode NLROM exhibits a lower nonlinear stiffness than the other two models, and would be expected to yield a higher σ_w than its counterparts as a result (note that the statistical linearization value for this NLROM remains a single-mode prediction, using the mode one cubic stiffness only). This is not the case, however: inclusion of additional modes in the basis reduces the midpoint response. Also observe that, in line with the theoretical expectation that a fixed, flat structure display no quadratic component of nonlinearity, the quadratic coefficients of both NLROMs were identified as several orders of magnitude lower than the cubic coefficients.

Finally, note that the statistical linearization approach yields values that are in line with those obtained through direct numerical simulation, with a 5-10% underprediction in each case. Additionally, the fully analytical Ritz model variance prediction of 2.86 mm is within 6% of the numerically simulated multi-mode NLROM response of 3.05 mm. Considering the roughly 400% error resulting from using a linear formulation of the structure, as opposed to a nonlinear model, a 6% error for an analytical prediction of nonlinear response is fairly insubstantial.

2.3 Nonlinear Normal Modes

Direct-time integration of NLROMs with random loadings, as performed above, is a natural method for validating models, but other techniques exist. Harmonic forcings may be used, or the structure may be released from some initial condition and the response examined in the time domain. However, methods

focused on validating models via an examination of the response are cumbersome for several reasons:

- Validation is load-dependent, both spatially and in terms of frequency content
- A nonlinear structure must be validated at a variety of energy levels, potentially requiring multiple load cases to be examined
- Response histories of the NLROM are usually compared to those of the full-order FEM, which can be prohibitively expensive to compute

Put another way, a dynamicist would rarely calibrate a linear structural model using a time history; rather, the linear vibration modes would be used to determine the accuracy of a model. The equivalent concept for a nonlinear structure is the nonlinear normal mode, which can be used to provide a *load-independent* validation metric for nonlinear structures.

Two main definitions of the NNM exist. The first, due to Rosenberg, [29], defines an NNM, in essence, as a *vibration in unison* of a system. This can be interpreted as a straightforward generalization of linear normal modes to nonlinear systems, however, it is not rigorously applicable to damped structures. To discuss NNMs in the context of nonconservative systems, Shaw and Pierre define a nonlinear normal mode as an invariant manifold in phase space [30]. Periodic orbits which begin in this manifold remain in it for all time.

The definition used in this work is a slight modification of Rosenberg's definition above, advanced by Kerschen et. al [31]. The requirement for vibration in unison is relaxed, so that an NNM is a *not-necessarily synchronous periodic motion* of the conservative system. Removing the requirement for synchronous motion admits the possibility of internal resonances – periodic solutions in which modes interact when their frequencies reach integer ratios – as NNMs, and is also useful when pursuing numerical computation of nonlinear modes.

In this work, numerical computation of NNMs is performed using the *NNMcont* MATLAB package, available from the University of Liège website² and described in [32]. A brief overview of the basic method in use is given below.

²URL: <http://www.ltas-vis.ulg.ac.be/cmsms/index.php?page=nnm>

Numerical Computation of NNMs

For use with generally applicable algorithms for the numerical continuation of periodic solutions, the nonlinear equations of motion in (2.16) are recast into homogenous state-space form,

$$\dot{\mathbf{z}} = \mathbf{g}(\mathbf{z}) \quad (2.18)$$

where the state vector is $\mathbf{z} = [\mathbf{q}^T \dot{\mathbf{q}}^T]^T$ and the state function is

$$\mathbf{g}(\mathbf{z}) = \begin{Bmatrix} \dot{\mathbf{q}} \\ -(\Lambda \mathbf{q} + \boldsymbol{\theta}(\mathbf{q})) \end{Bmatrix}$$

To emphasize the dependence of the solution on the initial conditions \mathbf{z}_0 , solutions at a time t are written as $\mathbf{z}(t, \mathbf{z}_0)$. Then, a two-point boundary problem is solved using a periodicity condition,

$$\mathbf{H}(\mathbf{z}_0, T) = \mathbf{z}(T, \mathbf{z}_0) - \mathbf{z}_0 \quad (2.19)$$

\mathbf{H} is referred to as a *shooting function* and, when driven to zero for a minimal period T , the resulting state vector \mathbf{z}_0 corresponds to the initial condition of an NNM of the system. NNMcont uses a shooting method to obtain such solutions, with the system response integrated numerically for a given period and set of initial conditions, and the Newton-Raphson scheme used for shooting corrections. A key feature of this algorithm is the requirement for the Jacobian of the state function $\mathbf{g}(\mathbf{z})$; for the NLRoms in use here, this can be found directly from (2.17). Additionally, a “phase condition” is required to fully specify the problem. The default phase condition implemented in NNMcont, which specifies that all initial velocities begin at zero, is used here.

Numerical Examples

For a system containing m degrees of freedom, there exist at least m nonlinear normal modes which originate at the structure’s linear modes. These are considered to be the fundamental NNMs of the system, and are the only type which will be discussed here. At low amplitudes, the NNMs are equivalent to the linear normal modes; as the energy in the system increases, however, the nonlinear periodic response begins to diverge from the linear prediction, in both frequency and initial state. For NLRoms

containing multiple modes, internal resonances may also manifest. These occur when the frequencies of two modes reach integer multiples of each other. For instance, a “1:3 resonance” is a common occurrence, and is observed when the natural frequency of a higher mode becomes three times that of a lower mode. Internal resonances can be difficult to compute or observe, and in the work presented here, it is only the main branch of each fundamental NNM “backbone” that is given consideration. If the backbone branches of two models are commensurate with each other, it is then assumed that the two models are dynamically equivalent.

A common visualization for the NNM is the frequency-energy plot (FEP), which tracks the variation of the resonant frequency as a function of energy present in the structure. FEP’s allow an easy understanding of the basic characteristics of a nonlinear system (i.e. whether the structure hardens or softens and to what extent it does so) and also allow ready identification of any internal resonances present. The first NNMs (emanating from mode 1) of the analytical Ritz model and two NLROMs from Section 2.2 are plotted in Figure 2.8. The increase of natural frequency with energy indicates a stiffening response, with the frequencies of each model increasing from 31 to roughly 38 Hz at deflection amplitudes of one thickness, denoted by the vertical dashed line. As the energy levels increase, it is clear that the analytical model is somewhat stiffer than the single-mode NLROM, which is itself stiffer than the three-mode NLROM. Of course, these differences pale in comparison to the frequency differential with the linear model, which is represented by a dashed horizontal line.

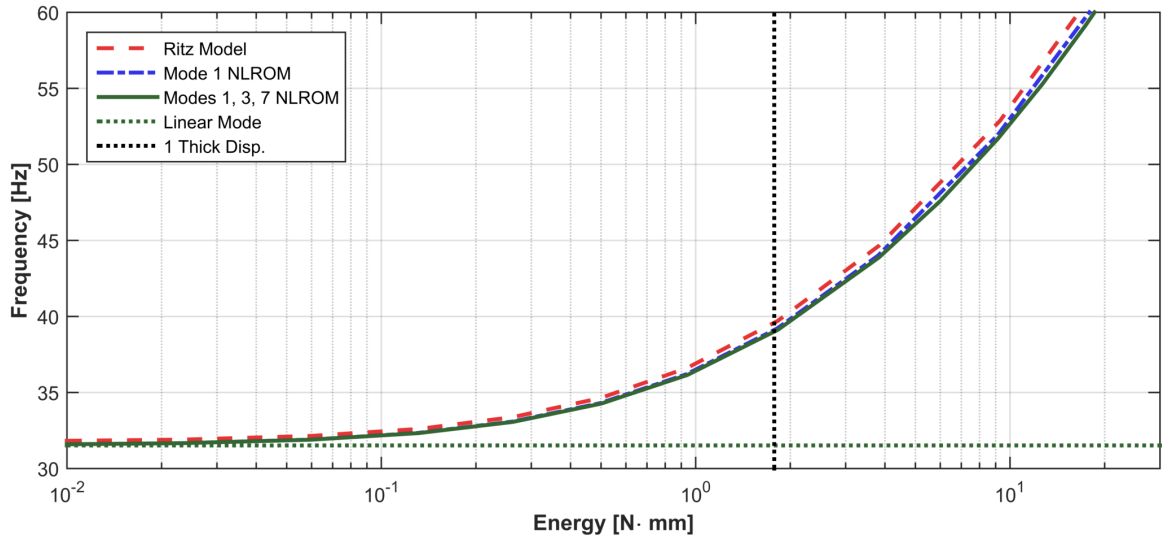


Figure 2.8: *Nonlinear normal modes of the analytical Ritz model from Section 2.1 and two NLROMs constructed from a full-order finite element model. The horizontal dashed line corresponds to the linear natural frequency of the beam’s first mode, while the vertical dashed line displays strain energy present in the beam at one thickness of displacement.*

Even though NNMs are defined with respect to the homogeneous, conservative equations of motion, they do have an intimate connection with the response of the associated damped and forced responses. For example, the NNM backbone represents a “worst-case” response to periodic forcing at a given frequency [33]. In [34], the relationship between stationary random response and nonlinear normal modes was examined qualitatively, and it was determined that the probability distribution of energy within a structure can be used along with a frequency-energy plot to accurately bracket the frequency spread of the response spectrum. This observation demonstrates that NNMs are closely linked with the forced, damped response of a structure. Continued examination of the link between NNMs and system response is an area of active research, but not considered further in this thesis.

Instead, NNMs will be used throughout Chapter 4 to evaluate the accuracy of various substructured NLROMs. The NNM framework provides an elegant method to evaluate the dynamics of a nonlinear system across a wide range of energy levels. A further advantage is the ease of comparing the NNM generated from a reduced order model with the full-order model. Given any point along the frequency-energy curve, the initial conditions \mathbf{z}_0 and period T can be supplied to a finite element model and integrated directly. The resulting output, designated \mathbf{z}_{FE} , can then be used to obtain a “periodicity error” condition ϵ , defined as

$$\epsilon = \frac{\|\mathbf{z}_0 - \mathbf{z}_{FE}\|}{\|\mathbf{z}_0\|} \quad (2.20)$$

with values on the order of one percent generally taken as acceptable.

It is also possible, albeit time-consuming, to compute NNMs directly from full-order finite element geometry [35], but such an approach is not pursued here. Application of the periodicity condition is demonstrated in Section 4.2.3, and the use of nonlinear normal mode backbones to compare various NLROMs is ubiquitous throughout Chapter 4.

2.4 Boundary Condition Dependence

The nonlinearities discussed above arise from membrane stretching along the axis of the beam in question. Clearly, the amount of nonlinearity displayed by a beam or a plate will be closely linked to the in-plane boundary conditions of a structure, which are usually not of interest for linear analysis of beams and plates in bending. The structure considered above was fully constrained along its axis, which is

not a physically realizable condition. To investigate the influence of axial boundary stiffness on beam nonlinearity, a modified finite element model was constructed, as shown in Figure 2.9. A grounded spring of stiffness k was oriented along the axis at each end of the beam. The transverse and rotational boundary conditions remained fully fixed, so that this alteration would not affect the linear modes of the structure. The effect of this spring stiffness on nonlinear behavior was assessed by constructing a series of first-mode NLROMs with a variety of values for k . The results below are reported in terms of the ratio k/k_b , where $k_b = AE/L$ is the basic axial stiffness of the beam.

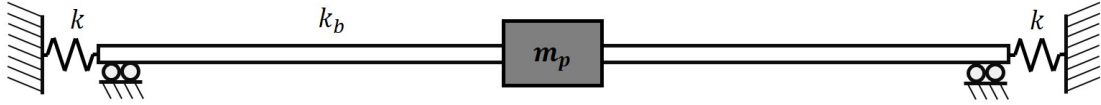


Figure 2.9: *Diagram of the modified beam with variable stiffness axial boundary conditions at each end. The transverse and rotational boundaries remain fully fixed.*

The axial deflection shapes corresponding to a loading of the beam in the shape of the first mode are shown in Figure 2.10 with four different values of k/k_b , along with the shape function for a fully fixed boundary.

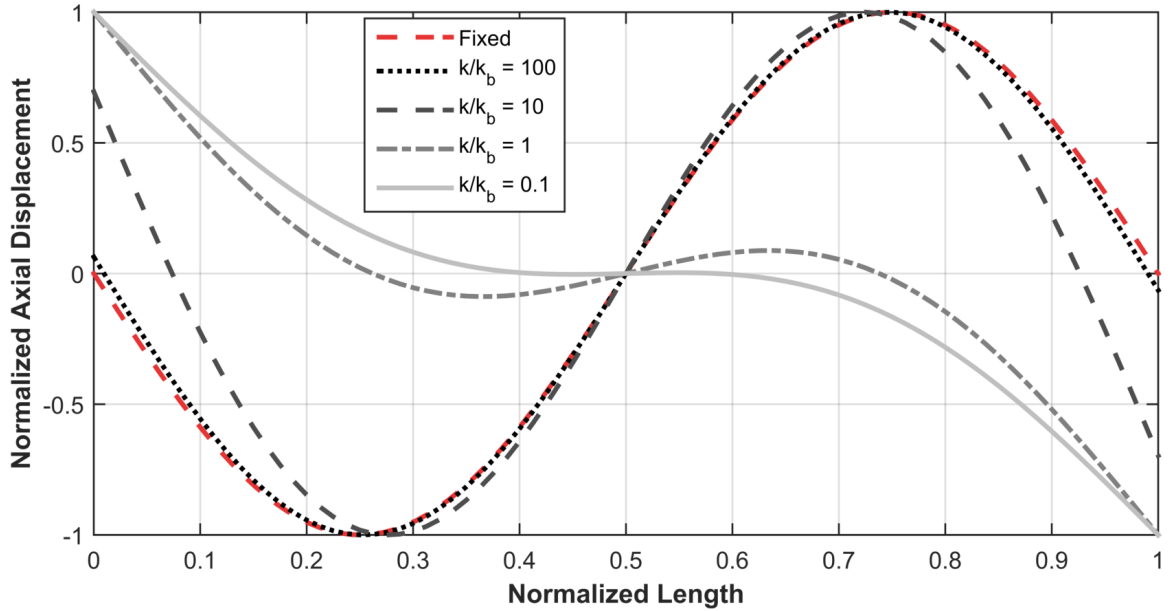


Figure 2.10: *Normalized shape function of axial displacement for a variety of stiffness ratios k/k_b along with the shape function for a fully fixed axial boundary.*

Between the ratios of $k/k_b = 10$ and $k/k_b = 1$, a rapid shift in the form of the shape functions occurs, with the maximum deflection moving from $x/L \approx 0.25$ and $x/L \approx 0.75$ to the endpoints as they

become free to deform. The effect of this changing shape on the stiffness coefficients is shown in Figure 2.11. Between the ratios pictured in Figure 2.10, the cubic stiffness coefficient drops by roughly an order of magnitude. As the stiffness ratio continues to drop, the coefficient eventually settles four orders of magnitude further, towards an essentially negligible value of 10^{-4} . This value is on the same order as the “theoretically zero” quadratic coefficients in Table 2.2.

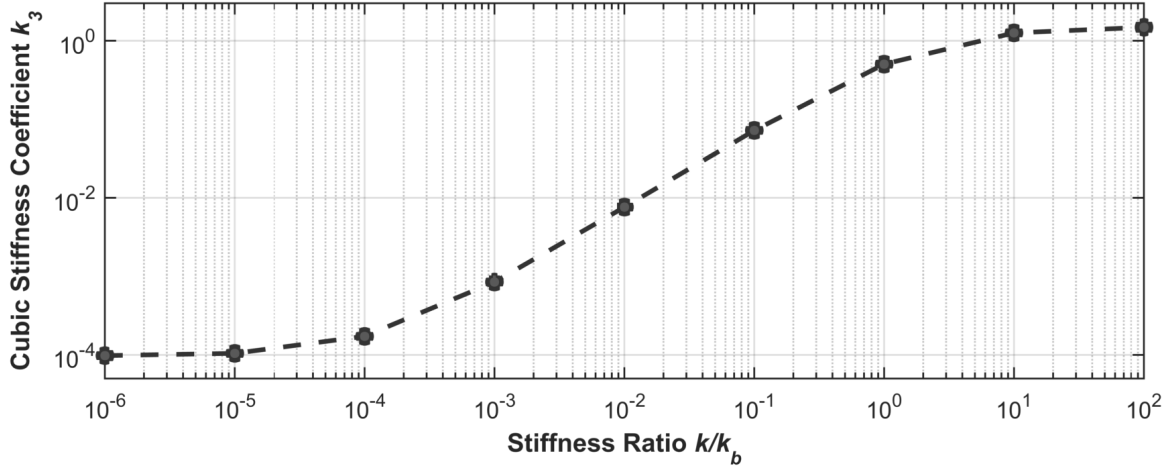


Figure 2.11: *Displacement standard deviation and stress RMS for the linear and nonlinear models. Vertical lines correspond to the thickness at which the stress RMS*

With single-mode NLROMs available, an assessment of their nonlinear dynamics was made using the NNMs of these models, shown in Figure 2.12. The NNM for $k/k_b = 100$ lies quite close to its fully fixed counterpart, and is comparable to the more accurate NNM of the multi-mode NLROM in Figure 2.8. The $k/k_b = 10$ model is still comparable in its dynamics, but, as with the shape functions, a rapid shift occurs below this stiffness ratio. At the energy levels where the stiff-boundary models have doubled in frequency to 60 Hz, the low-stiffness model with a ratio of $k/k_b = 0.1$ has increased a mere 4 Hz, or roughly 10%.

The influence of boundary conditions on NLROM stiffness, and the important ramifications of this subject for nonlinear substructuring, will become apparent in Chapter 4 and is discussed in further detail beginning with Section 4.2.3.

2.5 Motivation for Nonlinear Substructuring

The use of NLROMs for simple plate and beam structures has become fairly routine, and with care, even complex structures can be modeled successfully, as in the multi bay panel modeled in [24]. However,

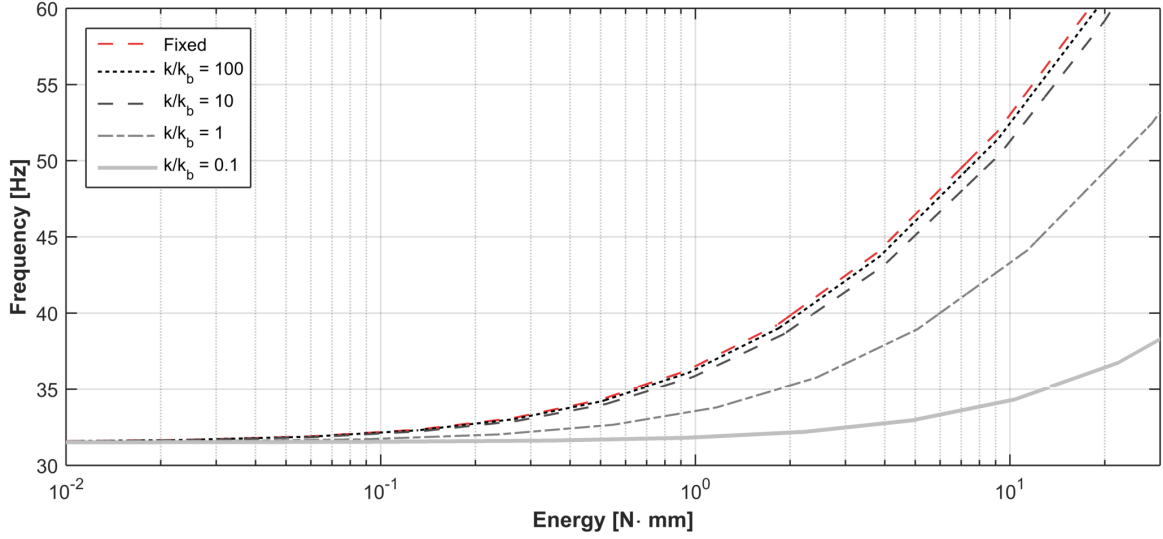


Figure 2.12: *Nonlinear normal modes of five beams corresponding to the shape functions shown in Figure 2.10.*

that case potentially represents the limits of what can be achieved with current NLROM methods, as it required an in-depth study into the appropriate bending modes and associated dual modes to be included in the deformation basis and, once the modes were selected, needed thousands of static load cases for full specification. Due to the cubic order of growth that both the enforced displacement and ICE methods exhibit, the prospect of developing NLROMs for even more complicated structures is not promising. If industrial-scale assemblies or vehicles are to be modeled with NLROMs, a different approach is required.

Component mode synthesis (CMS) of geometrically nonlinear structures is a potential solution. After constructing relatively simple NLROMs of an assembly's components, the nonlinear models can be assembled to obtain the equations of motion of the full structure. Due to the order of growth of load case counts, constructing a large number of low-order NLROMs requires fewer load cases than constructing a single high-order nonlinear model. Further, the substructuring framework allows components to be updated on an individual basis, rather than requiring a full re-specification of the assembly model. Determining sensitivities to changes in geometry or material properties also becomes a simpler task when performed at the component, rather than the assembly, level. Due to the wide range of temperatures and flight conditions experienced by hypersonic vehicles, the ability to quickly adapt the model to such changes will be of critical importance in the operational application of these reduced order models.

Kuether demonstrated nonlinear CMS on a variety of assemblies using the Craig-Bampton models and the primal assembly technique [14]. An immediate challenge associated with this method is the

large number of boundary degrees of freedom that are required to model any type of realistic structure – the boundary deformations must be included in the NLROM basis, thus, components with tens or hundreds of boundary constraint modes cannot be modeled efficiently. To circumvent this issue, “characteristic constraint modes,” first described by Castanier [36], were used to reduce the boundary degrees of freedom to a manageable count. Chapter 3 gives the mathematical development required for use of Craig-Bampton CMS with characteristic constraint modes, along with an explanation of the assembly process for nonlinear models.

Chapter 3

Linear and Nonlinear Component Mode Synthesis

This chapter reviews the familiar mathematical development of Craig-Bampton component mode synthesis using fixed-interface and constraint modes, presents the more recent enhancement of characteristic constraint modes for interface reduction, and finally discusses the recent extension of CMS techniques to geometrically nonlinear structures. Additional details of the NLROM construction process, as it pertains to components of a larger assembly, are also presented. Section 3.3 details the MATLAB tools used to perform the substructuring operations in this thesis, while their application to linear substructuring of a complex model is demonstrated in Section 3.4 to illustrate the utility of the characteristic constraint interface reduction.

3.1 Linear Component Mode Synthesis

The theoretical development of characteristic constraint modes follows easily from the Craig-Bampton component mode synthesis technique [12], so the latter is quickly reviewed. The system of interest consists of n components and a total of N degrees of freedom (DOF). The j^{th} component is represented in full-order form by the undamped equation of motion (3.1)

$$\mathbf{M}^j \ddot{\mathbf{x}}^j + \mathbf{K}^j \mathbf{x}^j = \mathbf{f}^j \quad (3.1)$$

with mass matrix \mathbf{M}^j , stiffness matrix \mathbf{K}^j , forcing vector \mathbf{f}^j , and physical displacement vector \mathbf{x}^j with N^j degrees of freedom. The double-overdot operator refers to the second derivative of each element with respect to time. Damping is omitted from this formulation, however, linear damping terms may easily be included. A variety of methods exist to calculate damping, but the most common rely on estimation or measurement of a damping ratio ζ for each mode. In the substructuring context, the damping ratios of each component may be estimated individually and assembled to obtain a system damping matrix, or the damping may be added using modes of the full assembly. Since the NNM validation metric used in this thesis operates on the conservative model of the structure, no further consideration is given to damping.

It should also be noted that the forcing vector \mathbf{f}^j is not fully general, but usually assumed to operate only on the interface DOF of each structure. The reason for this is related to the static reduction of Equation 3.2 and described below. The simplest method to circumvent this limitation is by specifying “boundary” nodes at points where loads must be applied; again, since NNMs are load-independent and do not require application of external loads, no such procedure is required here.

3.1.1 Craig-Bampton Component Mode Synthesis

The Craig-Bampton CMS technique reduces the order of (3.1) while placing it in a form amenable to substructuring with other components in the system. First, the coordinates are partitioned to a *boundary* set $\{b\}$ of size N_b^j , which contains all degrees of freedom eligible for attachment, along with an *interior* set $\{i\}$ of size N_i^j , which contains the remaining degrees of freedom in the component. The partitioned equation of motion is

$$\begin{bmatrix} \mathbf{M}_{ii}^j & \mathbf{M}_{ib}^j \\ \mathbf{M}_{bi}^j & \mathbf{M}_{bb}^j \end{bmatrix} \begin{Bmatrix} \ddot{\mathbf{x}}_i^j \\ \ddot{\mathbf{x}}_b^j \end{Bmatrix} + \begin{bmatrix} \mathbf{K}_{ii}^j & \mathbf{K}_{ib}^j \\ \mathbf{K}_{bi}^j & \mathbf{K}_{bb}^j \end{bmatrix} \begin{Bmatrix} \mathbf{x}_i^j \\ \mathbf{x}_b^j \end{Bmatrix} = \begin{Bmatrix} \mathbf{0}_i^j \\ \mathbf{f}_b^j \end{Bmatrix}$$

In most cases $N_i^j \gg N_b^j$, so a first objective is to reduce the size of the internal degree of freedom vector. To capture the deformation of internal variables due to deflections at the boundaries, a *static reduction* is performed. Noting from the partition above that under a static loading, $\mathbf{K}_{ii}^j \mathbf{x}_i^j + \mathbf{K}_{ib}^j \mathbf{x}_b^j = \mathbf{0}_i^j$, the interior degrees of freedom may be written in terms of the boundary degrees of freedom as $\mathbf{x}_i^j = -(\mathbf{K}_{ii}^j)^{-1} \mathbf{K}_{ib}^j \mathbf{x}_b^j = \boldsymbol{\Psi}_{ib}^j \mathbf{x}_b^j$, or

$$\begin{Bmatrix} \mathbf{x}_i^j \\ \mathbf{x}_b^j \end{Bmatrix} = \begin{bmatrix} \boldsymbol{\Psi}_{ib}^j \\ \mathbf{I}_{bb}^j \end{bmatrix} \mathbf{x}_b^j \quad (3.2)$$

where Ψ_{ib}^j forms the set of *constraint modes* associated with component j and \mathbf{I}_{bb}^j is an $N_b^j \times N_b^j$ identity matrix. The transformation (3.2) is known as a *Guyan* (or *static*) reduction; as mentioned above, it is only valid if no loads are applied internally so that the deformation of interior points depends only on loads and deformations at the component boundaries. Under these conditions, the transformation forms an exact reduced order model for the linear static case, but will lose accuracy when dynamics of the internal degrees of freedom are excited. To include these dynamics in the model, the interior points are written in terms of a modal reduction $\mathbf{x}_i^j = \Psi_{ik}^j \mathbf{q}_k^j$, where the modal matrix Ψ_{ik}^j is obtained through modal analysis of the constrained dynamic system

$$\begin{aligned} \mathbf{M}_{ii}^j \ddot{\mathbf{x}}_i^j + \mathbf{K}_{ii}^j \mathbf{x}_i^j &= \mathbf{0}_i^j \\ \left[\mathbf{M}_{ii}^j - \omega^2 \mathbf{K}_{ii}^j \right] \Psi_{ik}^j &= \mathbf{0}_i^j \end{aligned} \quad (3.3)$$

and truncated to include only the first N_k^j modes; these modal amplitudes are denoted by \mathbf{q}_k^j . Since (3.3) is precisely the equation of motion obtained by fixing all boundary DOF of the component, the resulting modes are referred to as fixed interface (FI) modes. Taken together with the static reduction performed earlier, the full displacement vector of the system is

$$\begin{Bmatrix} \mathbf{x}_i^j \\ \mathbf{x}_b^j \end{Bmatrix} = \begin{bmatrix} \Psi_{ik}^j & \Psi_{ib}^j \\ \mathbf{0}_{bk}^j & \mathbf{I}_{bb}^j \end{bmatrix} \begin{Bmatrix} \mathbf{q}_k^j \\ \mathbf{x}_b^j \end{Bmatrix} = \mathbf{T}_{CB}^j \begin{Bmatrix} \mathbf{q}_k^j \\ \mathbf{x}_b^j \end{Bmatrix} \quad (3.4)$$

which is referred to as the *Craig-Bampton* reduction of each component. With this transformation in hand, the system matrices themselves are transformed to Craig-Bampton coordinates using $\mathbf{M}_{CB}^j = (\mathbf{T}_{CB}^j)^T \mathbf{M}^j \mathbf{T}_{CB}^j$ and $\mathbf{K}_{CB}^j = (\mathbf{T}_{CB}^j)^T \mathbf{K}^j \mathbf{T}_{CB}^j$. Each reduced model has a total size of $N_{CB}^j = N_k^j + N_b^j$.

Once Craig-Bampton models of each component are obtained, they must be assembled to form the full structure. It is convenient to begin with the unassembled equations of motion by gathering the

block-diagonal system matrices and DOF vectors into

$$\begin{aligned}
 \hat{\mathbf{M}}_{CB} &= \begin{bmatrix} \mathbf{M}_{CB}^1 & & & \\ & \mathbf{M}_{CB}^2 & & \\ & & \ddots & \\ & & & \mathbf{M}_{CB}^n \end{bmatrix} & \hat{\mathbf{K}}_{CB} &= \begin{bmatrix} \mathbf{K}_{CB}^1 & & & \\ & \mathbf{K}_{CB}^2 & & \\ & & \ddots & \\ & & & \mathbf{K}_{CB}^n \end{bmatrix} \\
 \hat{\mathbf{q}}_{CB} &= \begin{bmatrix} \mathbf{q}_k^1 \\ \mathbf{x}_b^1 \\ \mathbf{q}_k^2 \\ \mathbf{x}_b^2 \\ \vdots \\ \mathbf{q}_k^n \\ \mathbf{x}_b^n \end{bmatrix} & \hat{\mathbf{f}}_{CB} &= \begin{bmatrix} \mathbf{0}_k^1 \\ \mathbf{f}_b^1 \\ \mathbf{0}_k^2 \\ \mathbf{f}_b^2 \\ \vdots \\ \mathbf{0}_k^n \\ \mathbf{f}_b^n \end{bmatrix}
 \end{aligned} \tag{3.5}$$

yielding the equations of motion

$$\hat{\mathbf{M}}_{CB} \hat{\mathbf{q}}_{CB} + \hat{\mathbf{K}}_{CB} \hat{\mathbf{q}}_{CB} = \hat{\mathbf{f}}_{CB} \tag{3.6}$$

Note that system matrices, generalized coordinate vectors, and modal matrices corresponding to the full system are distinguished by the overhat notation. The number of modal and boundary DOF in the unassembled system is $N_k = \sum_{j=1}^n N_k^j$ and $N_b = \sum_{j=1}^n N_b^j$, respectively. The total number of DOF in the unassembled system is $N_{CB} = N_k + N_b$.

Since many of the boundary DOF in $\hat{\mathbf{q}}_{CB}$ are coupled, (3.6) is not useful for computation (but *is* often useful for post-processing, due to the straightforward ordering of each DOF). Several methods are available for system assembly; here, the *primal assembly technique* [37] is used. From the known constraints between various boundary nodes in the system, a sparse, signed, Boolean constraint matrix \mathbf{B} can be formed. \mathbf{B} will have size $N_{constr} \times N_{CB}$, where N_{constr} is the number of constraints in the model. By construction, $\mathbf{B}\hat{\mathbf{q}}_{CB} = \mathbf{0}$, so it must admit a null space. The matrix \mathbf{L} is the unsigned Boolean matrix which spans the null space of \mathbf{B} , and has size $N_{CB} \times N_A$, where N_A denotes the count of remaining DOF in the assembled system.

The system (3.6) is assembled using the \mathbf{L} matrix by writing $\hat{\mathbf{q}}_{CB} = \mathbf{L}\hat{\mathbf{q}}_A$, where $\hat{\mathbf{q}}_A$ are the N_A independent, assembled degrees of freedom of the system. Transforming the unassembled system

matrices as $\hat{\mathbf{M}}_A = \mathbf{L}^T \hat{\mathbf{M}}_{CB} \mathbf{L}$ and $\hat{\mathbf{K}}_A = \mathbf{L}^T \hat{\mathbf{K}}_{CB} \mathbf{L}$ leads to the assembled system equations of motion (3.7).

$$\hat{\mathbf{M}}_A \hat{\mathbf{q}}_A + \hat{\mathbf{K}}_A \hat{\mathbf{q}}_A = \hat{\mathbf{f}}_A \quad (3.7)$$

Vibration modes of the assembly can be computed by solving the generalized eigenvalue problem for $\hat{\mathbf{M}}_A$ and $\hat{\mathbf{K}}_A$, leading to the modal matrix $\hat{\Phi}_A$. As mentioned, it is often more convenient to perform postprocessing in terms of the unassembled coordinate system, which corresponds to the unassembled modal matrix denoted here as $\hat{\Phi}_{CB} = \mathbf{L} \hat{\Phi}_A$. Finally, physical displacements of the system can be recovered on a part-by-part basis using (3.4), or globally by forming a block diagonal matrix in terms of the individual transformation matrices \mathbf{T}_{CB}^j .

3.1.2 Characteristic Constraint Modes

While the assembled system size N_A will be significantly lower than that of the full-order system N , in many cases the number of boundary DOF N_b will be significantly larger than the number of fixed interface modes N_k . The characteristic constraint (CC) mode concept involves performing a secondary modal reduction on the boundary nodes, further reducing the size of the assembled model. There are two differing approaches to the use of characteristic constraint modes. The modal reduction may either be performed globally, on the assembled system (3.7), as first shown by Castanier [36]. The reduction may also occur locally, prior to assembly, on each component system (3.4), as demonstrated by Hong et. al [38]. Only the former approach is covered here, since it is simpler to implement for complicated assemblies.

To continue from the assembled Craig-Bampton system, knowledge of the modal and boundary DOF indexing in $\hat{\mathbf{q}}_A$ is required, but not immediately apparent since boundary DOF may couple to any of several components via the transformation applied to $\hat{\mathbf{q}}_{CB}$. To obtain the DOF ordering, flatten the matrix \mathbf{L} , summing along columns, to obtain a vector of integers \mathbf{d} with size $1 \times N_A$. Then, define two sets:

$\{\hat{k}\} = \{d_i : d_i = 1\}$ are the DOF indices of the fixed interface modes.

$\{\hat{b}\} = \{d_i : d_i > 1\}$ are the DOF indices of the assembled boundary nodes.

Note that this approach is only valid if all boundary DOF in the model are attached, otherwise, only

constrained boundary DOF are included in the set $\{\hat{b}\}$. Once these indices are obtained, partition the assembled system matrices to the set $\{\hat{b}\}$ and perform a modal analysis to obtain the characteristic constraint modal matrix $\hat{\Psi}_{CC}$.

$$\left[(\hat{\mathbf{M}}_A)_{\hat{b}\hat{b}} - \omega_{CC}^2 (\hat{\mathbf{K}}_A)_{\hat{b}\hat{b}} \right] \hat{\Psi}_{CC} = 0 \quad (3.8)$$

The characteristic modal matrix is truncated to the first N_C modes; then, the boundary displacements are written in terms of the characteristic constraint modes as $\mathbf{q}_{\hat{b}} = \hat{\Psi}_{CC} \mathbf{q}_{CC}$. Thus, the transformation between the Craig-Bampton system (3.7) and the Characteristic Constraint system is

$$\begin{Bmatrix} \mathbf{q}_{\hat{k}} \\ \mathbf{q}_{\hat{b}} \end{Bmatrix} = \begin{bmatrix} \mathbf{I}_{\hat{k}\hat{k}} & \mathbf{0}_{\hat{k}C} \\ \mathbf{0}_{C\hat{k}} & \hat{\Psi}_{CC} \end{bmatrix} \begin{Bmatrix} \mathbf{q}_{\hat{k}} \\ \mathbf{q}_{CC} \end{Bmatrix} = \mathbf{T}_{CC} \hat{\mathbf{q}}_{CC} \quad (3.9)$$

where \mathbf{T}_{CC} is the characteristic constraint transformation matrix from CB coordinates and $\hat{\mathbf{q}}_{CC}$ is the global characteristic constraint DOF vector. Note the ordering of DOF, in particular, the re-ordering required for the CB DOF vector. To reduce the system to the CC description $\hat{\mathbf{M}}_{CC}$ and $\hat{\mathbf{K}}_{CC}$, partitioned system matrices are transformed according to

$$\hat{\mathbf{M}}_{CC} = \mathbf{T}_{CC}^T \begin{bmatrix} (\hat{\mathbf{M}}_A)_{\hat{k}\hat{k}} & (\hat{\mathbf{M}}_A)_{\hat{k}\hat{b}} \\ (\hat{\mathbf{M}}_A)_{\hat{b}\hat{k}} & (\hat{\mathbf{M}}_A)_{\hat{b}\hat{b}} \end{bmatrix} \mathbf{T}_{CC} \quad \hat{\mathbf{K}}_{CC} = \mathbf{T}_{CC}^T \begin{bmatrix} (\hat{\mathbf{K}}_A)_{\hat{k}\hat{k}} & (\hat{\mathbf{K}}_A)_{\hat{k}\hat{b}} \\ (\hat{\mathbf{K}}_A)_{\hat{b}\hat{k}} & (\hat{\mathbf{K}}_A)_{\hat{b}\hat{b}} \end{bmatrix} \mathbf{T}_{CC} \quad \hat{\mathbf{f}}_{CC} = \begin{bmatrix} \hat{\mathbf{0}}_k \\ \mathbf{T}_{CC}^T (\hat{\mathbf{f}}_A)_{\hat{b}} \end{bmatrix}$$

This resulting system has size $N_{CC} = N_k + N_C$, with equations of motion given in (3.10).

$$\hat{\mathbf{M}}_{CC} \hat{\mathbf{q}}_{CC} + \hat{\mathbf{K}}_{CC} \hat{\mathbf{q}}_{CC} = \hat{\mathbf{f}}_{CC} \quad (3.10)$$

An eigenvalue analysis can be performed on $\hat{\mathbf{M}}_{CC}$ and $\hat{\mathbf{K}}_{CC}$ to obtain the modes of the system $\hat{\Phi}_{CC}$. Due to the partitioning used to obtain the characteristic constraint mode description, transforming back to the Craig-Bampton modal description is a multi-step process:

1. Transform to the assembled, partitioned CB matrix using $\tilde{\Phi}_A = \mathbf{T}_{CC} \hat{\Phi}_{CC}$.
2. “Unpartition” to the assembled CB matrix $\hat{\Phi}_A$ using an inverse sort procedure¹
3. Transform to the unassembled space using $\hat{\Phi}_{CB} = \mathbf{L} \hat{\Phi}_A$

¹This is best described programatically: In MATLAB, stack the DOF sets $\{\hat{k}\}$ and $\{\hat{b}\}$ in a column vector and recover their sort indices: $[\sim, sortIdx] = sort([kIdx; bIdx]);$ the resulting vector of indices is applied to $\hat{\Phi}_A$ to obtain $\hat{\Phi}_A$.

From the unassembled Craig-Bampton models, physical displacements can be recovered as described before.

3.2 Extension to Geometrically Nonlinear Structures

The substructuring approach is now extended to admit geometrically nonlinear restoring forces. The monolithic approach shown in Section 2.2 is first described in terms of the component-level models in use here, and an explanation of the ICE method as implemented in this work is presented. The assembly procedure itself follows, along with a primer on the use of alternate basis vectors to represent the nonlinear restoring force vector.

3.2.1 Component-Level Nonlinearity

Now, consider the application of the aforementioned substructuring techniques to structures involving nonlinear forces. Each conservative component equation of motion is now

$$\mathbf{M}^j \ddot{\mathbf{x}}^j + \mathbf{K}^j \mathbf{x}^j + \mathbf{f}_{nl}^j(\mathbf{x}^j) = \mathbf{f}^j \quad (3.11)$$

with $\mathbf{f}_{nl}^j(\mathbf{x}^j)$ a nonlinear restoring force vector associated with the geometric nonlinearity of the system. Given a modal reduction matrix and corresponding set of generalized coordinates $\mathbf{x}^j = \mathbf{\Phi}^j \mathbf{q}^j$, where $\mathbf{\Phi}^j$ is a vector of FI and component-localized CC modes and \mathbf{q}^j are their modal coordinates, the reduced system becomes

$$\bar{\mathbf{M}}^j \ddot{\mathbf{q}}^j + \bar{\mathbf{K}}^j \mathbf{q}^j + \boldsymbol{\theta}^j(\mathbf{q}^j) = \bar{\mathbf{f}}^j \quad (3.12)$$

The transformed load vector is $\bar{\mathbf{f}}^j = (\mathbf{\Phi}^j)^T \mathbf{f}^j$ and the reduced system matrices are $\bar{\mathbf{M}}^j = (\mathbf{\Phi}^j)^T \mathbf{M}^j (\mathbf{\Phi}^j)$ and $\bar{\mathbf{K}}^j = (\mathbf{\Phi}^j)^T \mathbf{K}^j (\mathbf{\Phi}^j)$. For Craig-Bampton models using characteristic constraint modes, $\mathbf{\Phi}^j$ will contain the component's fixed-interface modes along with the local partition of the system's characteristic constraint modes; in this case the reduced mass matrix will not be diagonal. The component stiffness matrix is not necessarily diagonalized by the local partition of system CC modes, but the block corresponding to the fixed interface modes will at least be diagonal.

The nonlinear force, when transformed to the modal domain, becomes $\boldsymbol{\theta}^j(\mathbf{q}^j) = (\mathbf{\Phi}^j)^T \mathbf{f}_{nl}^j(\mathbf{\Phi}^j \mathbf{q}^j)$.

The physical-coordinate form of this force, \mathbf{f}_{nl}^j , is never actually considered. Instead, as in Chapter 2, the r^{th} term in the nonlinear modal restoring force vector is written as follows:

$$\theta_r^j(q_1^j, q_2^j, \dots, q_m^j) = \sum_{i=1}^m \sum_{k=1}^m B_r^j(i, k) q_i^j q_k^j + \sum_{i=1}^m \sum_{k=1}^m \sum_{l=1}^m A_r^j(i, j, k) q_i^j q_k^j q_l^j \quad (3.13)$$

The summation index m indicates the number of basis vectors in Φ^j . The arrays A_r^j and B_r^j contain quadratic and cubic stiffness coefficients of the nonlinear model; specification of these coefficients gives a complete determination of the NLROM. As discussed in Chapter 2, two key approaches exist to perform this task; the Implicit Condensation and Expansion method [39] is used here. A series of static loads are applied to the full order model, each one a linear combination of the basis vectors in Φ^j . These are pre-multiplied by the stiffness matrix to better isolate individual modes. The vectors \mathbf{f}_A , used to identify cubic stiffness coefficients, and \mathbf{f}_B , used to identify quadratic stiffness coefficients, are defined in terms of basis vectors of index r , s , and v as

$$\begin{aligned} \mathbf{f}_A &= \frac{1}{3} \mathbf{K}^j [f_r \{\Phi^j\}_r + f_s \{\Phi^j\}_s + f_v \{\Phi^j\}_v] \\ \mathbf{f}_B &= \frac{1}{2} \mathbf{K}^j [f_r \{\Phi^j\}_r + f_s \{\Phi^j\}_s] \end{aligned} \quad (3.14)$$

with a separate load scaling term f_r , f_s , and f_v for each mode in the basis. The indices r , s , and v need not be unique, and the fractional factors are included so that loadings including, e.g., three instances of the r^{th} mode, will have an effective scaling factor of f_r rather than $3f_r$. Selection of these load scaling terms is critical for an accurate fit of the nonlinear coefficients, since low loadings will not sufficiently exercise the structural nonlinearities, while high loadings will lead to convergence issues in the FEA solution. Kuether et al. [25] showed that an effective rule for selecting force amplitudes is to scale them such that the nonlinear static FE solution deflects 15 to 20 percent less (more) than a purely linear static solution due to the hardening (softening) characteristic of the nonlinearity. Loads pushing the linear model of the structure to a one thickness displacement often satisfy this criteria. Thus, the load scaling factors can be defined using the thickness t , a deflection scaling factor α_r , and the set of single-mode loadings. For the r^{th} mode,

$$\begin{aligned}\mathbf{K}^j \mathbf{x}^j &= f_r \mathbf{K}^j \{\Phi^j\}_r \\ \alpha_r t &= \max |\mathbf{x}^j| = \max |f_r \{\Phi^j\}_r| \\ f_r &= \frac{\alpha_r t}{\max |\{\Phi^j\}_r|}\end{aligned}$$

The resulting nonlinear deflection for each single-mode load case with the load scaling factor f_r can be compared to the value $\alpha_r t$, and α_r adjusted as needed until the linear/nonlinear ratio approaches 0.8 or 1.2.

Once the scaling factors are determined, a full set of load cases is generated and supplied to a nonlinear FEA code. The required number of load cases to specify all of the A_r^j and B_r^j coefficients has a cubic order of growth; the exact count can be determined from

$$2m + \frac{2m!}{(m-2)!} + \frac{4m!}{3(m-3)!} = \frac{2}{3}(2m^3 - 3m^2 + 4m)$$

3.2.2 Nash's Form of Nonlinear Restoring Force

The polynomial expression (3.13) is an explicit description of the nonlinear restoring force on a mode-by-mode basis, but a more compact representation is available due to Nash [5]. By defining the quadratic and cubic nonlinear force vectors as

$$\begin{aligned}\beta^j(\mathbf{q}^j) &\Rightarrow \beta_r^j(\mathbf{q}^j) = \sum_{i=1}^m \sum_{k=1}^m B_r^j(i, k) q_i^j q_k^j \\ \alpha^j(\mathbf{q}^j) &\Rightarrow \alpha_r^j(\mathbf{q}^j) = \sum_{i=1}^m \sum_{k=1}^m \sum_{l=1}^m A_r^j(i, j, k) q_i^j q_k^j q_l^j\end{aligned}$$

and taking the Jacobian of each so that $\mathbf{N}_1^j(\mathbf{q}^j) = \nabla \beta^j(\mathbf{q}^j)$ and $\mathbf{N}_2^j(\mathbf{q}^j) = \nabla \alpha^j(\mathbf{q}^j)$, the component equation of motion can be written

$$\bar{\mathbf{M}}^j \ddot{\mathbf{q}}^j + \left[\bar{\mathbf{K}}^j + \frac{1}{2} \mathbf{N}_1^j(\mathbf{q}^j) + \frac{1}{3} \mathbf{N}_2^j(\mathbf{q}^j) \right] \mathbf{q}^j = \mathbf{0}$$

This also allows easy specification of the restoring force Jacobian, which is simply

$$\left[\bar{\mathbf{K}}^j + \mathbf{N}_1^j(\mathbf{q}^j) + \mathbf{N}_2^j(\mathbf{q}^j) \right]$$

and the elastic potential energy of the component

$$(\mathbf{q}^j)^T \left[\frac{1}{2} \bar{\mathbf{K}}^j + \frac{1}{6} \mathbf{N}_1^j(\mathbf{q}^j) + \frac{1}{12} \mathbf{N}_2^j(\mathbf{q}^j) \right] \mathbf{q}^j$$

These forms are amenable to assembly within a substructure of multiple components.

3.2.3 Assembly of Craig-Bampton/Characteristic Constraint Substructures

To proceed with actual assembly of the nonlinear forces, we must apply a procedure which differs somewhat from the linear assembly process. The full assembly equations of motion are

$$\hat{\mathbf{M}}_{CC} \hat{\mathbf{q}}_{CC} + \left[\hat{\mathbf{K}}_{CC} + \frac{1}{2} \hat{\mathbf{N}}_1(\hat{\mathbf{q}}_{CC}) + \frac{1}{3} \hat{\mathbf{N}}_2(\hat{\mathbf{q}}_{CC}) \right] \hat{\mathbf{q}}_{CC} = \hat{\mathbf{f}}_{CC} \quad (3.15)$$

in which $\hat{\mathbf{N}}_1(\hat{\mathbf{q}}_{CC})$ are $\hat{\mathbf{N}}_2(\hat{\mathbf{q}}_{CC})$ the assembled nonlinear Jacobian matrices which we seek. Recall that the characteristic constraint degrees of freedom are written in terms of the component fixed interface modal amplitudes \mathbf{q}_k^j and the global characteristic constraint modal amplitudes \mathbf{q}_{CC} ,

$$\hat{\mathbf{q}}_{CC} = \begin{Bmatrix} \mathbf{q}_k^1 \\ \mathbf{q}_k^2 \\ \vdots \\ \mathbf{q}_k^n \\ \mathbf{q}_{CC} \end{Bmatrix}$$

Each characteristic constraint mode will enter the displacements of all components in the assembly.

An “unassembled” vector of FI/CC coordinates can also be written:

$$\hat{\mathbf{q}}_{CC,u} = \begin{Bmatrix} \mathbf{q}_k^1 \\ \mathbf{q}_{CC} \\ \mathbf{q}_k^2 \\ \mathbf{q}_{CC} \\ \vdots \\ \mathbf{q}_k^n \\ \mathbf{q}_{CC} \end{Bmatrix} = \begin{Bmatrix} \mathbf{q}^1 \\ \mathbf{q}^2 \\ \vdots \\ \mathbf{q}^n \end{Bmatrix}$$

The assembled and unassembled coordinate vectors are related by $\hat{\mathbf{q}}_{CC} = \mathbf{L}_{CC}\hat{\mathbf{q}}_{CC,u}$. \mathbf{L}_{CC} is an assembly matrix operating in the FI/CC domain, and can be constructed easily since all fixed interface modes are independent of each other and all characteristic constraint modes are constrained. This assembly matrix provides a framework for assembling the nonlinear restoring forces of each component. Similar to assembly of the linear system matrices, unassembled Jacobian matrices are block diagonal in terms of the component Jacobians,

$$\hat{\mathbf{N}}_{1,u}(\hat{\mathbf{q}}_{CC,u}) = \begin{bmatrix} \mathbf{N}_1^1(\mathbf{q}^1) & & & \\ & \mathbf{N}_1^2(\mathbf{q}^2) & & \\ & & \ddots & \\ & & & \mathbf{N}_1^n(\mathbf{q}^n) \end{bmatrix} \quad \hat{\mathbf{N}}_{2,u}(\hat{\mathbf{q}}_{CC,u}) = \begin{bmatrix} \mathbf{N}_2^1(\mathbf{q}^1) & & & \\ & \mathbf{N}_2^2(\mathbf{q}^2) & & \\ & & \ddots & \\ & & & \mathbf{N}_2^n(\mathbf{q}^n) \end{bmatrix}$$

The assembled Jacobian matrices are written

$$\begin{aligned} \hat{\mathbf{N}}_1(\hat{\mathbf{q}}_{CC}) &= \mathbf{L}_{CC}^T \hat{\mathbf{N}}_{1,u}(\mathbf{L}_{CC}\hat{\mathbf{q}}_{CC,u})\mathbf{L}_{CC} \\ \hat{\mathbf{N}}_2(\hat{\mathbf{q}}_{CC}) &= \mathbf{L}_{CC}^T \hat{\mathbf{N}}_{2,u}(\mathbf{L}_{CC}\hat{\mathbf{q}}_{CC,u})\mathbf{L}_{CC} \end{aligned} \tag{3.16}$$

Finally, the component transformation matrix Φ^j corresponding to the fixed interface/characteristic constraint mode coordinates \mathbf{q}^j must be specified. The fixed interface modes are available directly, but the component's characteristic constraint mode deformations are available only in terms of the global

set of constraint modes. To obtain the CC mode partition associated with the j^{th} component, the CC mode matrix must be partitioned to that component's constraint mode degrees of freedom, so that $\mathbf{x}_b^j = \{\hat{\Psi}_b\}^j \mathbf{q}_{CC}$. The component's physical degrees of freedom are then

$$\begin{Bmatrix} \mathbf{x}_i^j \\ \mathbf{x}_b^j \end{Bmatrix} = \begin{bmatrix} \Psi_{ik}^j & \Psi_{ib}^j \{\hat{\Psi}_b\}^j \\ \mathbf{0}_{bk}^j & \{\hat{\Psi}_b\}^j \end{bmatrix} \begin{Bmatrix} \mathbf{q}_k^j \\ \mathbf{q}_{CC} \end{Bmatrix} = \Phi^j \mathbf{q}^j \quad (3.17)$$

The transformation matrix Φ^j in (3.17) specifies the set of basis vectors used to perform the non-linear coefficient fit. The overall process for computing and assembling an NLROM is summarized:

- After the FI/CC substructuring procedure, partition the characteristic mode matrix and supply Φ^j to each component.
- Set the load scaling factors f_r so that each single-mode load case, having the shape $\mathbf{K}^j \{\Phi^j\}_r$, yields a nonlinear static deflection which differs from a linear static prediction by 15 to 20 percent. Linear displacements of one thickness provide a good starting point.
- Compute all possible permutations of the load cases from (3.14), supply as static loads to a non-linear FEA program, and curve fit coefficients of the NLROM according to (3.13). Each NLROM is now available at the component level.
- The nonlinear restoring force is assembled at each timestep for simulation. Each component NLROM is supplied with the fixed interface and CC displacements \mathbf{q}^j to compute the component Jacobian matrices; these are then assembled using (3.16) and supplied to the equations of motion (3.15) to advance the system state.

Note from the last point that a nonlinear model of the full system is never explicitly created. A full assembly procedure could be accomplished with the aid of symbolic algebra software, however, such an approach is not taken in this work.

3.2.4 Nonlinear Force Definition with Alternate Basis Vectors

A critical aspect of the ICE algorithm is the process used to estimate nonlinear displacements resulting from the load cases of (3.14). Suppose the matrix of displacements, obtained from an FE code, is denoted by \mathbf{Y} . When the load basis Φ^j is orthogonal through the stiffness matrix so that $(\Phi^j)^T \mathbf{K}^j \Phi^j =$

$\mathbf{\Lambda}$ where $\mathbf{\Lambda}$ is a diagonal matrix with nonzero determinant, then a left pseudo-inverse of $\mathbf{\Phi}^j$ can be written so that $[\mathbf{\Lambda}^{-1}(\mathbf{\Phi}^j)^T \mathbf{K}^j] \mathbf{\Phi}^j = \mathbf{I}$ and the modal displacements associated with the loading are $\mathbf{q}^j = [\mathbf{\Lambda}^{-1}(\mathbf{\Phi}^j)^T \mathbf{K}^j] \mathbf{Y}$.

Unfortunately, orthogonality cannot be guaranteed for the basis vectors used here, which involve partitions of the system CC modes to individual components. As such, MATLAB's *pinv* routine was used generate a Moore-Penrose psuedo-inverse of $\mathbf{\Phi}^j$ to estimate modal amplitudes from the nonlinear FE results. It may be the case that $\mathbf{\Phi}^j$ is poorly conditioned – the localized CC modes may very closely resemble fixed interface modes of that component, for instance – which causes difficulty in finding an accurate solution for the modal amplitudes. The problem is exacerbated when displacements from the nonlinear FEA model must be approximated by a fixed set of linear structural modes, since the nonlinear model may respond in an unpredictable manner. When the modal coefficients for a given set of forces cannot be accurately estimated, the least squares routine used to construct (3.13) does not provide accurate estimates of the nonlinear restoring force coefficients, and the resulting NLRom is inaccurate or even unstable.

To circumvent this issue, alternate sets of basis vectors can be used in the static curve fit procedure. These sets should still span the subspace described by the fixed interface and localized CC modes, but display orthogonality with respect to each other for better conditioning and more accurate estimation of the modal response amplitudes. Two strategies are presented here and examined in Chapter 4, the singular value decomposition (SVD) and the QR decomposition.

Singular Value Decomposition

First, consider the singular value decomposition, which decomposes the $N^j \times m$ matrix $\mathbf{\Phi}^j$ into the product

$$\mathbf{\Phi}^j = \mathbf{U}^j \mathbf{S}^j (\mathbf{V}^j)^T = \begin{bmatrix} \mathbf{U}_1^j & \mathbf{U}_2^j \end{bmatrix} \begin{bmatrix} \mathbf{\Sigma}^j & \mathbf{0} \\ \mathbf{0} & \mathbf{0} \end{bmatrix} \begin{bmatrix} (\mathbf{V}_1^j)^H \\ (\mathbf{V}_2^j)^H \end{bmatrix} \quad (3.18)$$

The matrices of interest from the decomposition are \mathbf{U}_1^j (size $N^j \times m$; spans the column space of $\mathbf{\Phi}^j$), $\mathbf{\Sigma}^j$ (diagonal with size $m \times m$, contains the nonzero singular values of $\mathbf{\Phi}^j$), and $(\mathbf{V}_1^j)^H$ (size $m \times m$, spans the row space of $\mathbf{\Phi}^j$). With these, the basis vectors can be written

$$\mathbf{U}_1^j \boldsymbol{\Sigma}^j (\mathbf{V}_1^j)^H = \boldsymbol{\Phi}^j$$

and the physical displacement vector becomes

$$\mathbf{x}^j = \boldsymbol{\Phi}^j \mathbf{q}^j = \mathbf{U}_1^j \boldsymbol{\Sigma}^j (\mathbf{V}_1^j)^H \mathbf{q}^j$$

By introducing the coordinate transformation $\boldsymbol{\eta}^j = \boldsymbol{\Gamma}_{SVD}^j \mathbf{q}^j$ and letting $\boldsymbol{\Gamma}_{SVD}^j = \boldsymbol{\Sigma}^j (\mathbf{V}_1^j)^H$, the transformed basis vectors are contained in \mathbf{U}_1^j :

$$\mathbf{x}^j = \mathbf{U}_1^j \boldsymbol{\eta}^j$$

Loads in the shape of \mathbf{U}_1^j can be applied to the nonlinear static model in order to extract coupling coefficients written as functions of the modal amplitudes η_r^j .

QR Decomposition

Similarly, the QR transformation can be used to obtain an orthogonal basis of the FI/CC subspace. With this method, the initial matrix $\boldsymbol{\Phi}^j$ can be written

$$\boldsymbol{\Phi}^j = \mathbf{Q}^j \mathbf{R}^j = \begin{bmatrix} \mathbf{Q}_1^j & \mathbf{Q}_2^j \end{bmatrix} \begin{bmatrix} \mathbf{R}_1^j \\ \mathbf{0} \end{bmatrix} \quad (3.19)$$

so that

$$\mathbf{x}^j = \boldsymbol{\Phi}^j \mathbf{q}^j = \mathbf{Q}_1^j \mathbf{R}_1^j \mathbf{q}^j$$

where \mathbf{Q}_1^j is orthogonal and \mathbf{R}_1^j is upper triangular. Writing the amplitudes as $\boldsymbol{\eta}^j = \boldsymbol{\Gamma}_{QR}^j \mathbf{q}^j$ and $\boldsymbol{\gamma}_{QR}^j = \mathbf{R}_1^j$, the transformed basis vectors are contained in \mathbf{Q}_1^j :

$$\mathbf{x}^j = \mathbf{Q}_1^j \boldsymbol{\eta}^j$$

Static loads can be applied in the shape of the basis vectors of \mathbf{Q}_1^j and used to evaluate the nonlinear

restoring force coefficients in terms of those shapes.

Assembly and Integration

In either case, the full assembly is still integrated using the FI/CC coordinates, so at each timestep, each component's nonlinear restoring force is computed by:

- Transforming from FI/CC coordinates to decomposition coordinates using $\boldsymbol{\eta}^j = \boldsymbol{\Gamma}^j \mathbf{q}^j$ (with $\boldsymbol{\Gamma}^j$ corresponding to either $\boldsymbol{\Gamma}_{SVD}^j$ or $\boldsymbol{\Gamma}_{QR}^j$)
- Using the identified coefficients to compute Jacobian matrices in the decomposed space; $\tilde{\mathbf{N}}_1^j(\boldsymbol{\eta}^j)$ and $\tilde{\mathbf{N}}_2^j(\boldsymbol{\eta}^j)$, with overtilde denoting that these matrices do not operate on FI/CC coordinates.
- Transforming the component Jacobian matrices back to FI/CC space as shown below in (3.20)

$$\begin{aligned}\mathbf{N}_1^j(\mathbf{q}^j) &= (\boldsymbol{\Gamma}^j)^T \tilde{\mathbf{N}}_1^j(\boldsymbol{\eta}^j) \boldsymbol{\Gamma}^j \\ \mathbf{N}_2^j(\mathbf{q}^j) &= (\boldsymbol{\Gamma}^j)^T \tilde{\mathbf{N}}_2^j(\boldsymbol{\eta}^j) \boldsymbol{\Gamma}^j\end{aligned}\tag{3.20}$$

The linear model of each component remains in the untransformed FI/CC space. Once each component's nonlinear restoring force is evaluated, assembly proceeds as usual via (3.16).

3.2.5 Error Metrics

Finally, a note on NLROM evaluation is in order. As mentioned, the nonlinear normal mode provides an excellent method for validation of reduced order models; however, a preliminary method to immediately estimate the quality of an NLROM fit is also helpful. For this purpose, two metrics are defined – a *displacement error* measure and a *force error* measure. Given an arbitrary modal matrix $\boldsymbol{\Phi}$, a set of applied loads \mathbf{F} , and the resulting displacements from nonlinear FEA \mathbf{Y} , the estimated modal displacements are $\mathbf{q} = \boldsymbol{\Phi}^\dagger \mathbf{Y}$, with $(\cdot)^\dagger$ the pseudo-inverse operator. The residual displacement error from this estimate is

$$\epsilon_{disp} = \frac{\|\boldsymbol{\Phi} \mathbf{q} - \mathbf{Y}\|}{\|\mathbf{Y}\|}\tag{3.21}$$

The true nonlinear restoring force is obtained by subtracting the projected applied force from the

linear restoring force: $\mathbf{f}_{nl} = \mathbf{\Phi}^T \mathbf{F} - \bar{\mathbf{K}} \mathbf{q}$. This is compared to the nonlinear force generated by the NLROM, $\boldsymbol{\theta}_{nl}(\mathbf{q})$, to obtain a residual force error.

$$\epsilon_{force} = \frac{\|\boldsymbol{\theta}_{nl}(\mathbf{q}) - \mathbf{f}_{nl}\|}{\|\mathbf{f}_{nl}\|} \quad (3.22)$$

These two metrics will be used extensively in Chapter 4 below.

3.3 MATLAB Substructuring Toolset

Taking together the Craig-Bampton substructuring, characteristic constraint mode reduction, generation of component nonlinear models, and model assembly/integration leads to a complicated set of mathematical operations that must be performed. Typically, the MATLAB computing environment is used with a script-driven, “functional” programming style that puts the user in direct control of the model reduction process. This approach is well-suited for application to relatively simple problems, but becomes untenable and prone to error when handling assemblies with large numbers of components. Rather than use a functional approach, the results in this work were obtained using an object-oriented framework that automates many aspects of the linear and nonlinear substructuring procedure. Fundamentals of object-oriented programming as it applies to MATLAB may be found in the online documentation [40].

Since the toolset is quite flexible for modification and may be of interest to future researchers in the area of nonlinear substructuring, its function and use is described here. An example application follows.

The toolset consists of five key MATLAB classes, shown in Figure 3.1. The system is best visualized from the “ground up,” as arranged in the image. The user interacts almost exclusively with the CCSS module at top center; the other classes are designed to automatically interact with each other in the background. A brief description of each class is given below; full listings of class properties and methods can be found by examining the source code documentation.

ABINT - Abaqus Interface Module

Both the linear and nonlinear substructuring procedures require the use of full-order finite element codes. In this thesis, Abaqus is used exclusively. The ABINT class handles all analysis requests to the FE code and returns all results. It also stores basic model information for a particular structure. Since all model

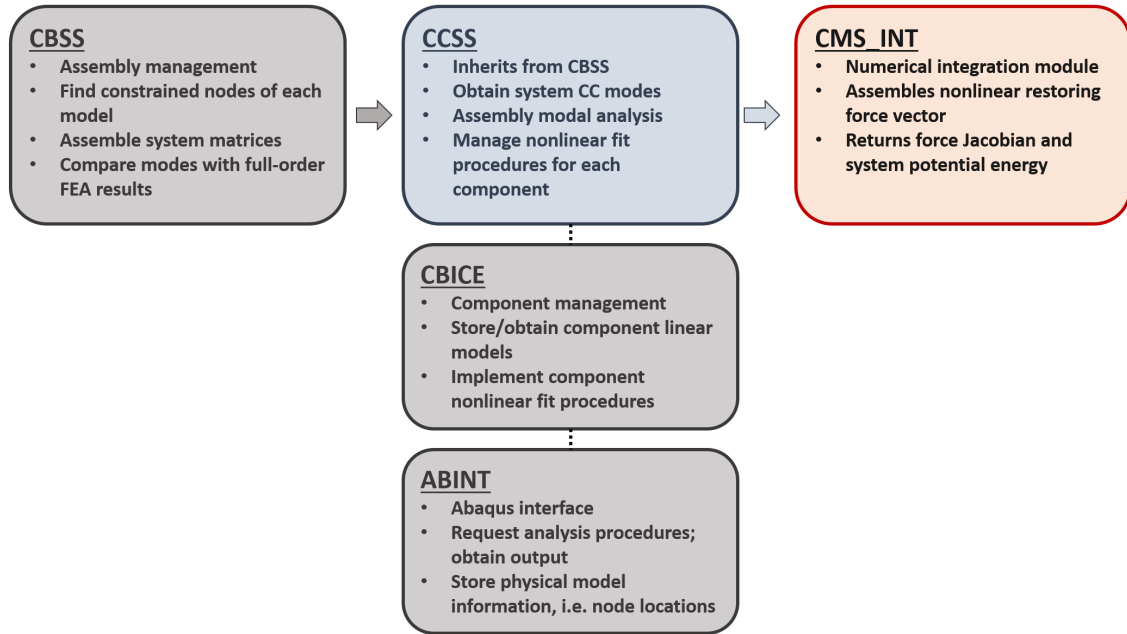


Figure 3.1: *MATLAB* class modules used in this work. The user interacts most frequently with the blue *CCSS* module; the others interact automatically in the background.

data is stored within the MATLAB class, model geometry, material parameters, etc. can be easily modified to perform sensitivity analysis of a structure.

The core functionality of ABINT is contained in the *writeInp* method, which uses the stored model data to write an Abaqus-readable input deck. Once this deck is written, it is included in follow-on analysis decks which the class will also write, before invoking the Abaqus solver for the problem of interest. Only a very small subset of Abaqus' capabilities – those directly applicable to modal substructuring, along with nonlinear static and unforced dynamic procedures – are currently available, although the set may be easily expanded should other solution routines be necessary. The Python program used to read model database data was obtained from the Air Force Research Laboratory, whose support in this matter is greatly appreciated.

The other critical method contained within ABINT is *readInp*, which reads an existing Abaqus input file and stores the data so that the model may be saved for later use. Reading is performed in two stages: First, ABINT requests a “datacheck” of the input deck to be read. The datacheck procedure parses the input job and forms an output database containing the model data, but does not execute any analysis. The resulting output database is then opened and scanned using Python to obtain element and node definitions along with listings of element and node sets. Since other critical model information,

such as section definitions, are difficult to obtain from the output database, ABINT then scans the input file directly for any definitions of interest and stores these in plain text form.

A critical feature of ABINT is that boundary conditions are treated as independent of the model data and are not stored. A set of boundary conditions must be specified in the function call when requesting a particular analysis. This provides the routine with added flexibility and is, of course, practically a necessity when performing substructuring procedures that may need to analyze the same basic structure under a variety of different boundary condition types.

Finally, note that users may easily replace ABINT with another, equivalent interface to a different finite element procedure by maintaining the same method prototypes and replacing the implementation as necessary. This well-defined modularity is a key benefit of the object-oriented approach.

CBICE - Craig Bampton Implicit Condensation/Expansion Module

A level above ABINT lies the CBICE class, which handles the substructuring procedures (both linear and nonlinear) for each component in an assembly. Each CBICE must be constructed using an existing ABINT object, automatically associating a CBICE instance with a given component.

CBICE serves as the link between ABINT and the full assembly. During the linear substructuring procedure, CBICE calculates fixed interface and constraint modes of its associated component and assembles them into a Craig-Bampton representation for use by the assembly. CBICE also performs the NLROM construction procedure for each component, based on a set of deformations which are supplied in terms of the component's free interface and constraint modes. Basis vector transformation, force scale determination, and nonlinear coefficient estimation all occur within this class.

CBSS - Craig Bampton Substructuring Module

CBSS is written to handle assembly-level substructuring, along with “administrative” functions, such as placement of each component, determination of the appropriate degrees of freedom to be coupled, and verification of the computed assembly modes with those of a full-order finite element model.

After creation, CBICE components are added to the CBSS object by specifying their location, any natural boundary conditions pertaining to the component, any eligible nodes for connection to other components in the model, and the number of fixed interface modes to retain – either by specification of a mode count or a frequency range. After all components are added, the *makeConnections* method

scans an array of eligible nodes and determines, based on physical proximity, which nodes should be constrained to each other. Once the connections are determined so that the boundary conditions of each component are known, component-level CB models are created by the CBICE objects stored within CCSS.

The method *buildCBSystem* assembles the components. The array of nodal constraint is first used to create the sparse \mathbf{B} constraint matrix, and MATLAB's *null* routine with the optional "rational" flag is used to generate a corresponding sparse \mathbf{L} matrix. While it is not necessary to actually construct an \mathbf{L} matrix, MATLAB's sparse matrix routines are quite advanced. The use of the actual sparse matrix, rather than a loop-based indexing procedure, is not only computationally more efficient (MATLAB's loop control structures are often the cause of performance bottlenecks) but drastically reduces the potential for errors in the assembly code, reducing debugging time. The computational cost of finding a sparse matrix inverse is a small price to pay for these benefits. A non-standard MATLAB function *spspaces* may be located on the MATLAB file exchange in order to very quickly determine the null space of a large sparse matrix, however, the procedure re-orders coordinates in a manner which is problematic. The built-in *null* function was sufficient for the purposes of this work.

Once the assembly matrix is constructed, the block diagonal system matrices are created and transformed into assembled system matrices. At this point, a modal analysis of the system may be performed in Craig Bampton coordinates. The alternate MATLAB function *eigs*, rather than the more customary *eig*, is used for eigenvalue analysis; *eigs* is intended for use on large sparse matrices where only a subset of the modes are of interest. In this case, the appropriate number of "smallest magnitude" eigenvalues are requested, along with their corresponding eigenvectors. To validate the results of a modal analysis performed with the routine, a full-order output database file may be loaded using *loadOdb* and used to assess frequency errors and perform a MAC check of the substructured and finite element modes with the *makeMac* method. There is no direct correspondence between node indexing in the finite element model and that of the substructured assembly, so nodes are compared based on their proximity to each other.

Since nonlinear reduced order modeling is not feasible for Craig Bampton models with traditional constraint modes, due to the large mode count required, no NLROM capabilities are implemented in CBSS. These are saved for its child class, CCSS.

CCSS - Characteristic Constraint Substructuring Module

CCSS inherits from CBSS, leaving the bulk of the linear substructuring machinery to its parent class. The only linear substructuring procedure implemented in CCSS is the *buildCCSystem*, which partitions the system appropriately, performs secondary modal analysis of the assembly boundaries, and applies the characteristic constraint reduction to the boundary nodes of the assembly. Once this is achieved, modal analysis of the transformed CC system proceeds as usual, and the results may be validated as described above for CBSS.

All nonlinear modeling of the components is channeled through CCSS. First, the method *initNLSys-tem* initializes the assembly by giving all components a default nonlinear model of the appropriate size with coefficients of zero. Then, a variety of *addNLPart* functions may be used to specify a nonlinear fit; these differ in terms of the basis and boundary conditions used – Chapter 4 explains the various options in detail. The CBICE models contained within CCSS do not have knowledge of the global CC modes of the structure, so the appropriate CC mode partitions must be supplied to each component for use within the nonlinear fit routine. CCSS also, when necessary, determines the equivalent static stiffness of the structure boundaries and supplies the resulting values for use as grounded spring boundary conditions. See Section 4.2.3 for a description of this procedure.

CCSS does not contain a provision for validation of the nonlinear model, since the NNM computation procedure is fairly involved and uses a standalone code (*NNMcont*, see Section 2.3). To avoid passing large amounts of model data unnecessarily, a lightweight class *CMS_INT* handles numerical integration of the CCSS nonlinear model.

CMS_INT - Numerical Integration Module

Very little of the CCSS model data is required to perform numerical integration of the nonlinear system; the only requirements are a reduced mass and stiffness matrix, the nonlinear polynomial coefficients of each component, and some basic information regarding the number of fixed interface modes per component and number of CC modes in the assembly (for integration of nonconservative systems, information related to damping is, of course, also necessary). *CMS_INT* accepts a CCSS model as an object and obtains the required information for use *within* a numerical integration routine. In addition to storing the linear mass and stiffness matrices, *CMS_INT* contains methods which will return the nonlinear restoring force, nonlinear force Jacobian, and nonlinear strain energy of the beam as a function of displacements,

as described by the set of fixed interface and CC coordinates.

3.4 Application

To demonstrate the utility of characteristic constraint modes, substructuring is performed on a moderately complex panel/stiffener structure. The assembled structure of interest is a 3×3 multi-bay panel originally studied by Przekop, Rizzi, and Groen in 2006 [41] with follow-on study by Perez et al. in 2012 [24]. The nine skin panels are overlaid on four hat stiffeners, which are themselves overlaid on four S-stiffeners. The S-stiffeners are fully clamped at each end, with no other boundaries applied to the model (this is a departure from the boundary conditions used in the earlier studies). All nodes of each panel are tied in all degrees of freedom to the supporting structure, leading to a large number of attachment degrees of freedom.

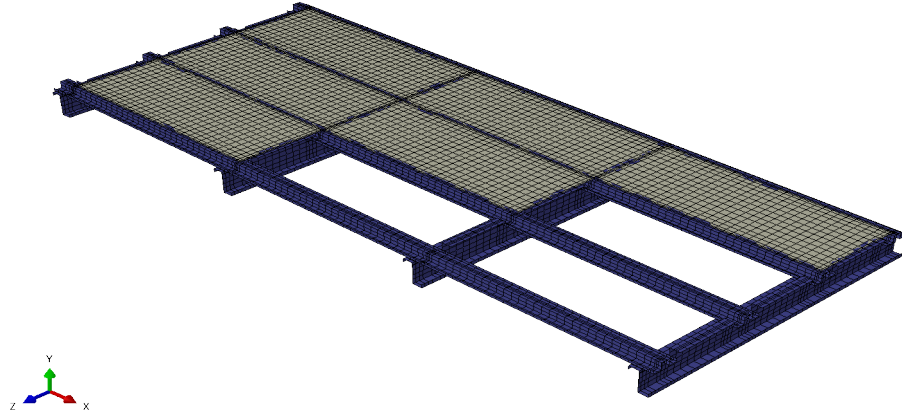


Figure 3.2: *Mesh of the multi-bay panel model; nearest three panels hidden to expose the underlying support structure.*

The entire structure is aluminum with an elastic modulus of 10.5Msi, Poisson's ratio of 0.33, and density of $2.614 \cdot 10^{-4} \frac{\text{lb} \cdot \text{s}^2}{\text{in}} (slinch)$. The model consists predominantly of S4R linear shell elements, with varying thicknesses between components; attachments between the support structures are realized using short B31 elements (representing rivet connections) with a 0.05 inch length and 0.02 inch diameter. The overall length, width, and height of the model are 58, 25, and 3 inches respectively; each panel has a size of 18.75 by 7.5 inches. Properties of the mesh are given in Table 3.1. In a second departure from the mesh used in [41] and [24], the B31 elements between the support structure and the panels are omitted to facilitate the use of characteristic constraint modes. This decision was made to avoid the possibility

of dynamically unimportant single-beam modes dominating the characteristic constraint mode matrix.

Part	Nodes	Elements		DOF	Shell Thickness [in]
		S4R	B31		
S-Stiffener	931	768	53	5586	0.05
Hat Stiffener	1598	1470	8	9588	0.04
Panel	578	528	–	3468	0.05
Total	15178	13704	244	91068	–

Table 3.1: *Mesh properties of the multi-bay panel shown in Figure 3.2.*

A full-order Abaqus model was used as a baseline for comparison with the substructuring techniques. Figure 3.3 depicts four key modeshapes of the assembly. The first mode (115 Hz) corresponds to independent bending of all panels; as the mode number increases, bending localizes to different areas of the panel, as shown in mode 6. Mode 10, at 192 Hz, shows the first occurrence of independent second-mode bending of each panel. Finally, mode 19 at 245 Hz exhibits large-scale bending of the hat stiffeners. The characteristic constraint mode model constructed below targets a frequency range up to 250 Hz (encompassing the first 20 modes of the structure), so higher modes are of no further interest.

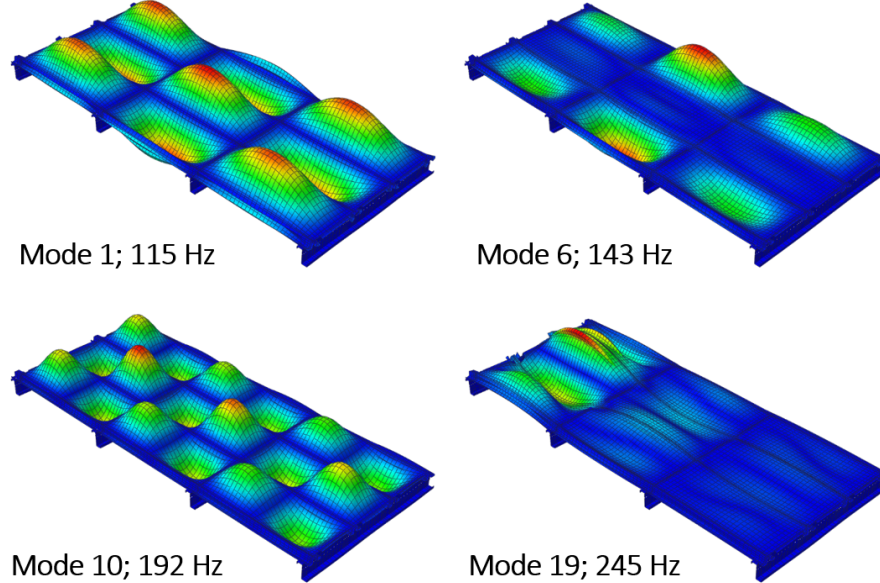


Figure 3.3: *Selected modeshapes of the full-order multi-bay panel.*

A traditional Craig-Bampton model with independent constraint modes was first constructed as a baseline. Five fixed interface modes per component were selected – due to the disparities in natural frequency between the panel and stiffeners, a uniform frequency range selection led to either too many

panel modes or too few stiffener modes. A summary of the Craig-Bampton CMS model is given in Table 3.2.

Part	Freq. Range [Hz]	FI Modes	Boundary DOF
S-Stiffener	[0, 1000]	5	210
Hat Stiffener	[0, 750]	5	648
Panel	[0, 600]	5	516
Total		85	8076
Constraints	4836	Assembled DOF	3325

Table 3.2: *Craig-Bampton substructure properties of the multi-bay panel components and full structure.*

Once the modal analysis of the Craig-Bampton system was performed, the modes were expanded to physical space and compared to full-order Abaqus results. A modal assurance criterion (MAC) check was then performed between the two sets of modes, and a frequency comparison made based on the results of the MAC. (Frequencies were compared according to matching MAC values, rather than in direct sequential order.) The results of this procedure for the first 35 modes are shown in Figure 3.4. Numerical tabulation of these results for the first 20 modes is given in Appendix B, Table B.1.

Overall, the comparisons are quite close, with most frequency errors below 1% and all below 2% through the first 35 modes (up to 300 Hz). Several pairs of close modes either flip completely – the 7/8 and 16/17 set of modes, for instance – or merge into each other slightly, as with modes 19 through 23. However, the system is still of fairly high order, with the 3,325 remaining DOF amounting to 3.7% of the original model DOF. While this is a large reduction of DOF overall, it still remains an appreciable fraction of the original problem size; for present-day models of more representative size (perhaps 10 million degrees of freedom for an assembly), a reduced-order model containing only 1% of the initial DOF count would still be larger than the entire multi-bay panel example presented here. Of the 3,325 DOF in the model, 3,240, or 97%, are boundary degrees of freedom.

With such a large fraction of DOF located in the boundary set, the model can be dramatically reduced in size using characteristic constraint modes. 35 characteristic constraint modes were selected in order to maintain accuracy below 250 Hz. Results of the modal comparison are shown visually in Figure 3.5 and tabulated in Table B.2.

The resulting modes of the assembly are overall quite similar to those obtained from the Craig-Bampton procedure. The close-mode interchanges have disappeared entirely, and the frequency errors are not only comparable, but generally lower in size than those of the default Craig Bampton model.

Mode 7 yields both the highest frequency error and lowest MAC value up until mode 19 at 244 Hz, the top of the target frequency range. Above mode 25, at 272 Hz, the model falls apart completely. It is likely that the more accurate mode ordering and lower frequency errors are due to better numerical conditioning of the problem when the interface size is reduced.

The characteristic constraint model contains a total of 120 degrees of freedom, down from 3,325 in the Craig-Bampton model. This puts the final DOF count as 0.13% of the full-order DOF count, a much more significant reduction of order.

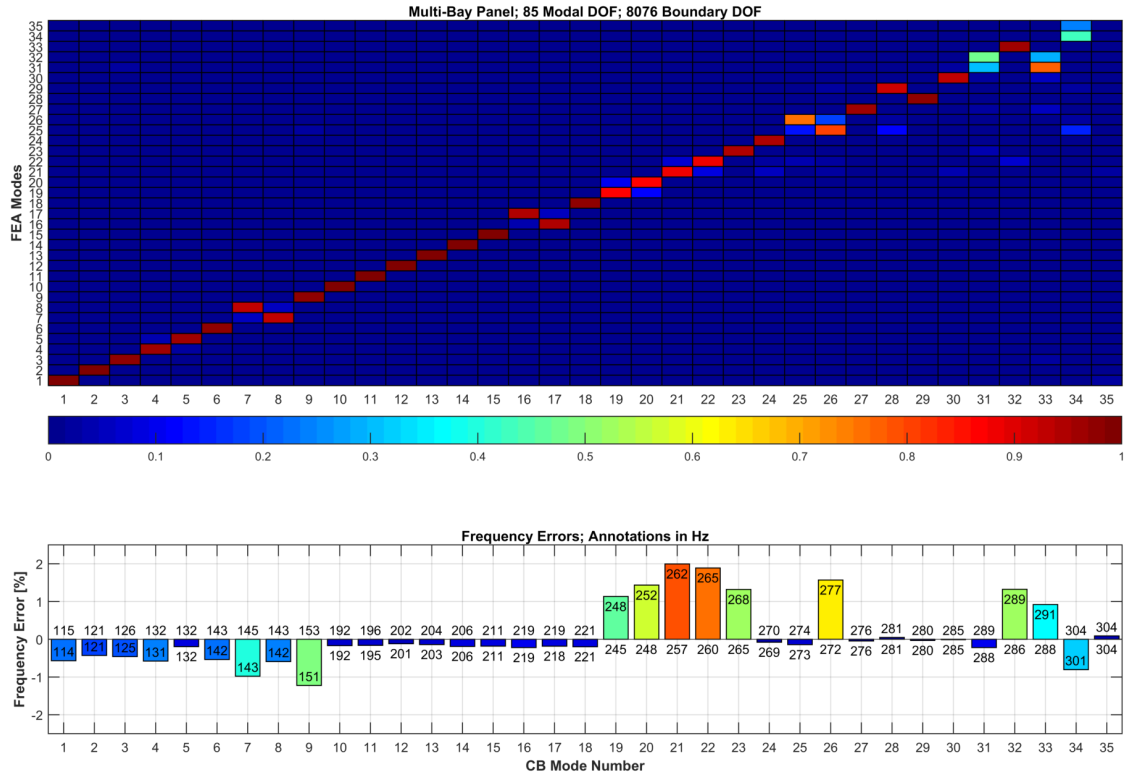


Figure 3.4: Modal assurance criterion and frequency error comparisons between full-order and Craig-Bampton modal analyses. Frequencies are compared in accordance with the maximum MAC value of each mode; frequency values along the horizontal axis are full-order values while those adjacent to error bars are the substructured values.

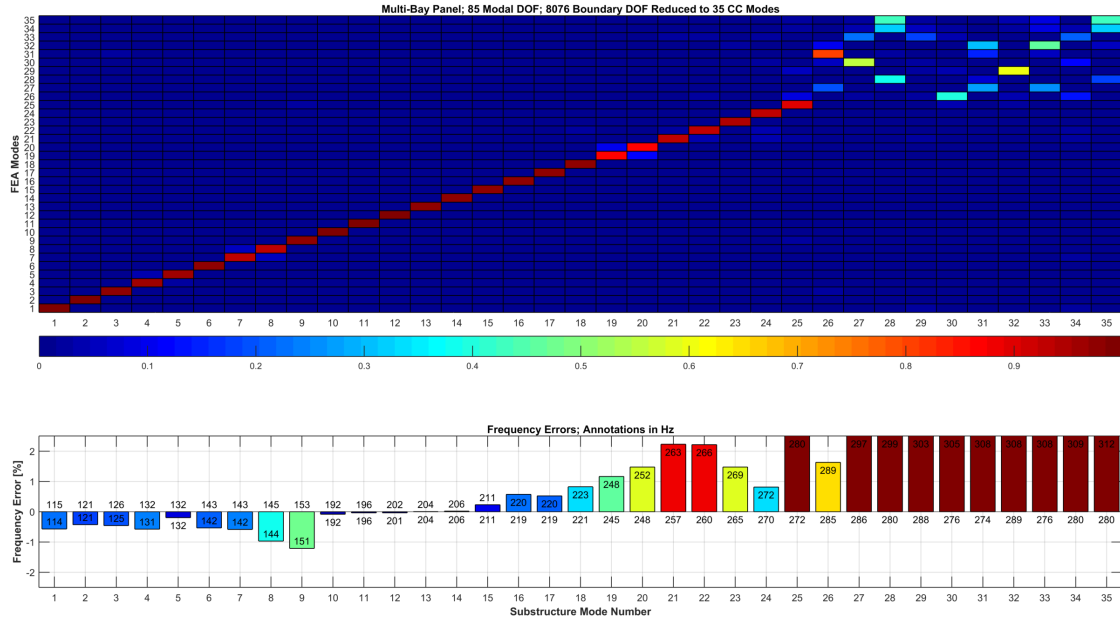


Figure 3.5: *Modal assurance criterion and frequency error comparisons between full-order and characteristic constraint modal analyses. Frequencies are compared in accordance with the maximum MAC value of each mode; frequency values along the horizontal axis are full-order values while those adjacent to error bars are the substructured values.*

3.5 Discussion

The multi-bay panel example above provides a convincing demonstration of the utility of characteristic constraint modes to dramatically reduce the number of interface degrees of freedom in a Craig-Bampton substructure. With five fixed interface modes per component and 3,240 constraint modes for the structure as a whole, each component of the traditional Craig-Bampton assembly would require 45 billion static load cases for specification of a nonlinear model.

Unfortunately, while the 35 characteristic constraint modes of the reduced-interface model is a much more reasonable quantity, this mode count still requires a fairly infeasible 82,240 load cases per component. Since the number of DOF in the assembly cannot be further reduced without beginning to sacrifice accuracy, help must come from another direction: The basis of fixed interface and characteristic constraint modes must be altered to capture the key deformations of each component in a smaller subset of vectors, or the component NLROMs must be constructed in a manner that simply omits some of the less important fixed interface/characteristic constraint modes. These approaches are studied in Chapter 4 on three much simpler assemblies.

Chapter 4

Case Studies in Nonlinear Substructuring

With the mathematics established for both linear and nonlinear aspects of the Craig-Bampton substructuring approach used here, specific case studies are now examined. The first of these, a two-plate system where each component is pinned about each edge, is identical to the system examined by Kuether [42] in 2014 and is used for verification of the MATLAB routines in use here, along with proof-of-concept for the SVD and QR alternate force bases discussed in Section 3.2.4.

Following the two-plate example, an assembly involving a pair of stiffeners supporting a beam is examined. This structure is intended to represent a truncated panel/stiffener section that might be found on an aircraft, and presents several difficulties not encountered with the first example. Finally, a model featuring two plates and an underlying support structure is considered.

The models constructed in this section are all evaluated using only their first nonlinear normal mode. In general, higher NNMs of a model should be checked to determine the accuracy of the NLROM at higher frequencies, but the assumption made in this chapter is that a modeling technique which generates a valid NLROM for the first NNM of a structure can also generate valid NLROMs for higher NNMs. Checking only the first NNM allows a relatively small subset of modes to be included in the nonlinear restoring force, which reduces the computational cost of repeatedly generating reduced order models using different approaches. It is critical to note that NLROMs which use only a subset of the modes of a component still maintain all of the modes in their linear models. For example, if a component

modeled with five fixed interface modes and ten characteristic constraint modes uses only the first three FI modes in its nonlinear basis, the 15×15 mass and stiffness matrices of the component will be retained in full, while the nonlinear restoring force vector will contain zero values for all but the first three modal force components.

Each section below is broken into subsections discussing the linear substructuring, construction of a reference nonlinear “truth” model, and nonlinear substructuring; brief discussion on the results of each model follows. This chapter concludes with a summary of lessons learned from the examples studied.

4.1 Simply Supported Plates

4.1.1 Linear Substructuring

The two plates are simply supported at all edges and coupled in rotational degrees of freedom along their interface. A summary of the material and structural properties is given in Table 4.1, while a summary of the mesh properties is given in Table 4.2.

Young’s Modulus [ksi]	Density [<i>slinch</i> /in ³]	Thickness [inch]
29,700	$27.36 \cdot 10^{-4}$	0.031

Table 4.1: *Material and structural properties of the plate substructure components.*

Part	Nodes	S4R Elements	DOF
9“ × 9” Plate	1369	1296	8214
9“ × 6” Plate	925	864	5550
Assembly	2257	2160	13542

Table 4.2: *Mesh properties of the plate substructure components.*

Kuether found that an accurate nonlinear ROM of this assembly could be constructed for the first three NNMs by retaining fixed interface modes up to 750 Hz along with the first four characteristic constraint modes. That validation process is not repeated here, instead, it will be quickly verified that the mode selections yield a satisfactory linear model before proceeding. The twelve fixed interface modes of the 9×9 plate and seven fixed interface modes of the 9×6 plate are shown in in Tables 4.3 and 4.4.

The four retained fixed interface modes are shown in Table 4.5. Note the similarity between each plate’s first fixed interface mode and the first characteristic constraint mode. The resemblance disappears as the CC frequency increases and the displacements localize to the interface.

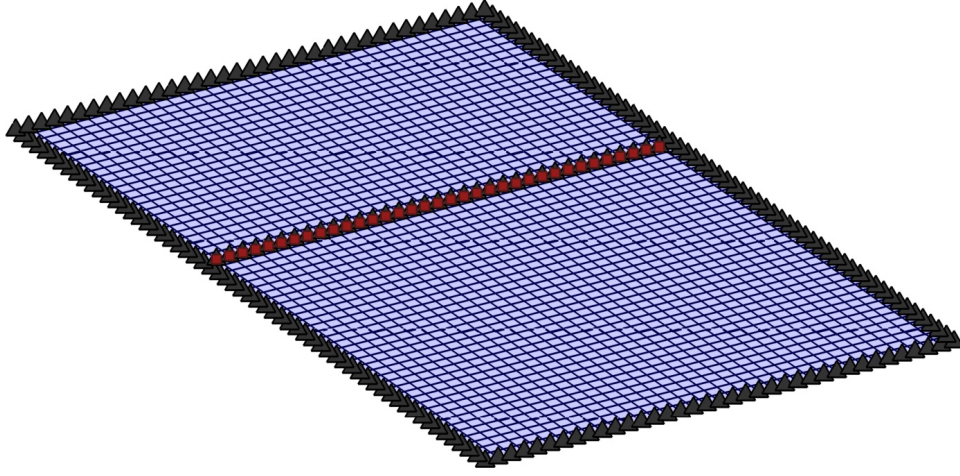


Figure 4.1: *Assembled two-plate model. Black triangles denote boundary conditions (all pinned in this case) while red squares denote coupling points (all rotational degrees of freedom).*

Table 4.3: *Fixed interface modes of the 9×9 plate. Interface is located towards the top-left of each pane.*

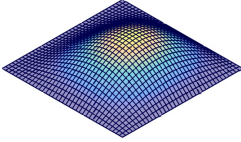
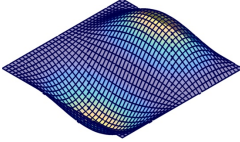
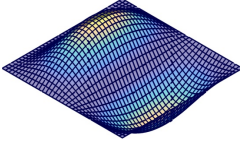
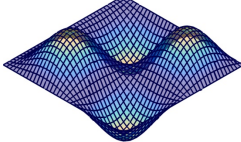
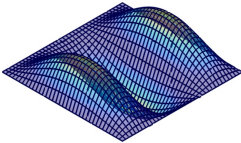
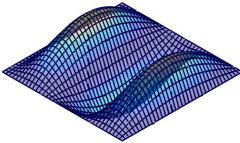
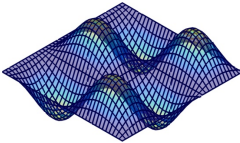
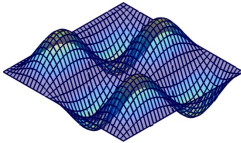
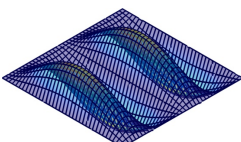
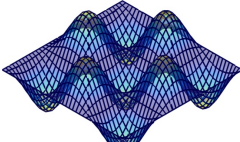
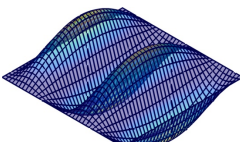
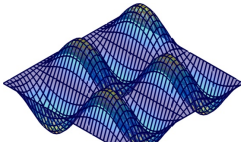
			
Mode 1: 87.1 Hz	Mode 2: 190.6 Hz	Mode 3: 216.6 Hz	Mode 4: 317.7 Hz
			
Mode 5: 371.4 Hz	Mode 6: 420.3 Hz	Mode 7: 494.6 Hz	Mode 8: 521.5 Hz
			
Mode 9: 630.0 Hz	Mode 10: 696.1 Hz	Mode 11: 700.6 Hz	Mode 12: 749.8 Hz

Table 4.4: *Fixed interface modes of the 9×6 plate. Interface is located towards the bottom-right of each pane.*

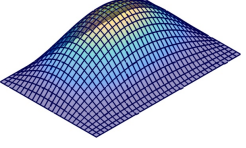
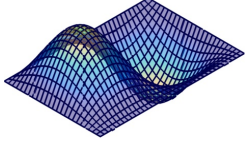
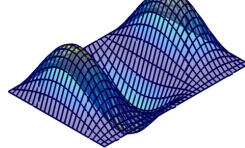
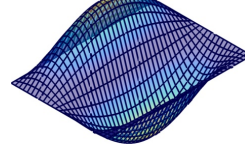
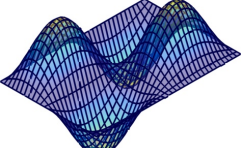
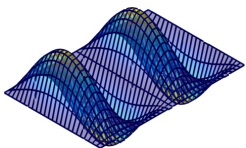
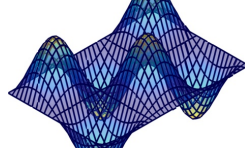
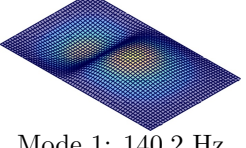
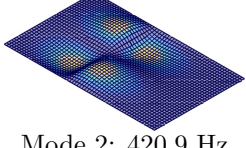
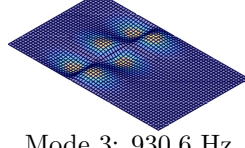
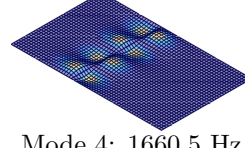
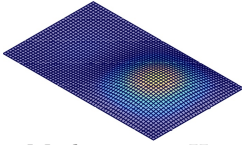
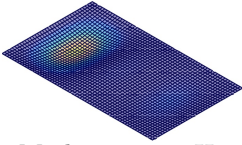
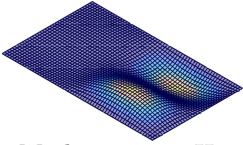
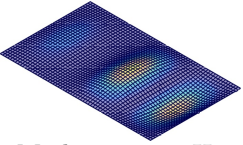
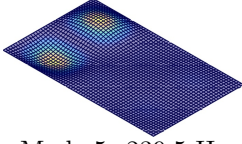
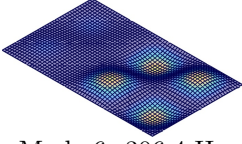
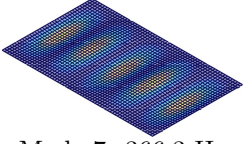
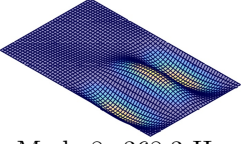
			
Mode 1: 156.8 Hz	Mode 2: 254.4 Hz	Mode 3: 430.1 Hz	Mode 4: 449.5 Hz
			—
Mode 5: 547.0 Hz	Mode 6: 685.2 Hz	Mode 7: 717.4 Hz	

Table 4.5: *Characteristic constraint modes of the assembled model.*

			
Mode 1: 140.2 Hz	Mode 2: 420.9 Hz	Mode 3: 930.6 Hz	Mode 4: 1660.5 Hz

Modes of the assembled system are shown in Table 4.6. A modal assurance criterion (MAC) check and frequency error check are provided in Figure 4.2. Frequency errors remain below 0.4% up to 470 Hz at Mode 11, and the MAC remains predominantly diagonal with the exception of mode switching between 15 and 16 (these are not “close modes”, as evident from inspection of the truth frequencies.) The assembly loses all accuracy above 750 Hz, as expected from the frequency range of fixed interface modes selected. Tabulated values for the modal comparisons are given in Appendix B, Table B.3.

Table 4.6: *Vibration modes of the assembled model, computed with the fixed-interface and characteristic constraint modes shown in Tables 4.3, 4.4, and 4.5*

			
Mode 1: 78.4 Hz	Mode 2: 135.1 Hz	Mode 3: 185.7 Hz	Mode 4: 203.0 Hz
			
Mode 5: 239.5 Hz	Mode 6: 306.4 Hz	Mode 7: 366.3 Hz	Mode 8: 368.3 Hz

4.1.2 Reference Nonlinear Model

A “truth” reduced order model can be easily constructed from a finite element model of the full assembly using subsets of the first few linear vibration modes. The backbone curves of three such models are shown in Figure 4.3, along with an NNM backbone computed from Kuether’s model, which was itself verified relative to the full-order finite element model; the trailing portion of this NNM collection corresponds to an internal resonance that was not fully computed. The three assembly NLROM backbones were computed using a step size that skipped this internal resonance, and otherwise agree well with the curve from Kuether’s model. For the remainder of this section, the five mode assembly NLROM is used as a basis for comparison with the substructured models.

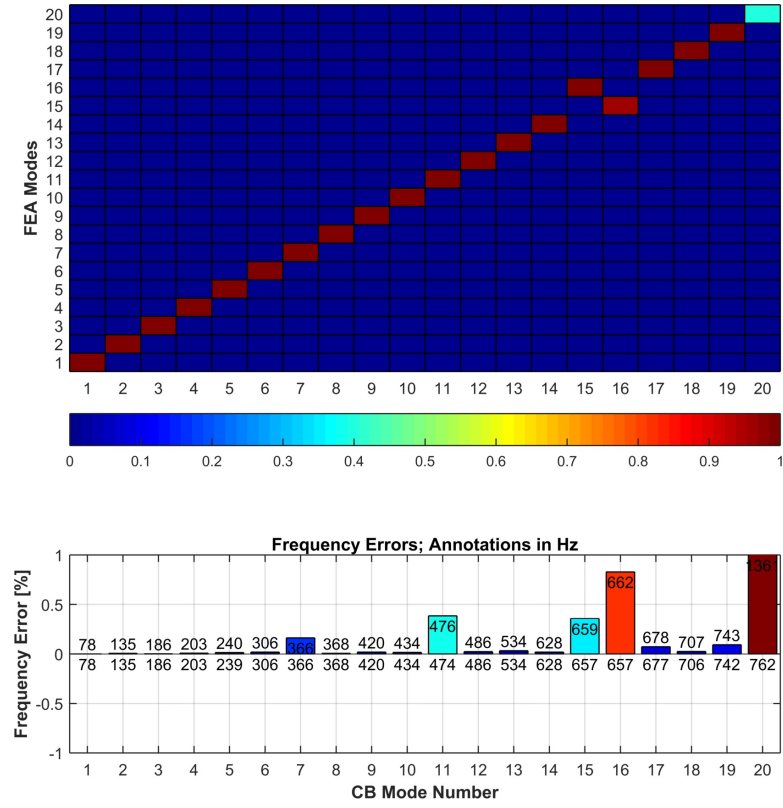


Figure 4.2: (Top): Cross-MAC between full-order FEA truth modes and substructure modes. (Bottom): Frequency errors between truth and substructure modes, based on matching MAC value; frequency values along the horizontal axis are full-order values while those adjacent to error bars are the substructured values.

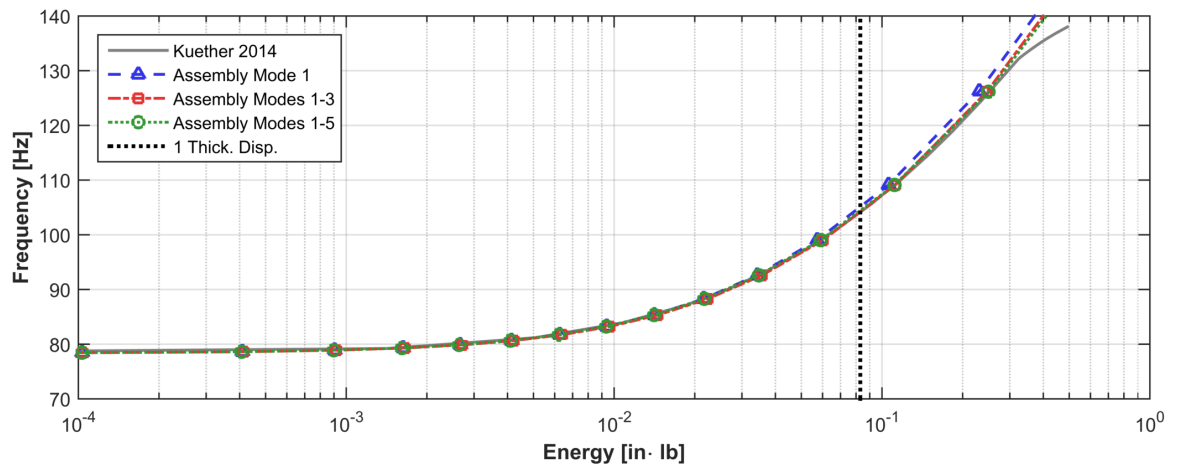


Figure 4.3: NNM backbone curves computed using NLROMs computed from a full assembly finite element model of the plates (first three curves) along with a curve computed using Kuether's substructured model from [42].

4.1.3 Nonlinear Substructuring

Prior to constructing any substructured NLROMs, three potential sets of basis vectors are investigated: The “natural” FI/CC set used by Kuether, the SVD transformation vectors described in (3.18), and the QR vectors described by (3.19). These transformations are not strictly necessary for this particular example, but are demonstrated here to display their viability and gain familiarity for the case studies to follow. General comparisons of the characteristics of each set of vectors are made using the “modal assurance criterion,” which is intended to measure consistency between sets of modeshapes, but is used here to determine to what extent the vectors in each basis set resemble on another. For example, in Figure 4.4, a cross-MAC of the FI/CC basis with the SVD basis (left) and QR basis (right) reveals that each factorization results in significantly different sets of basis vectors. Note that in Figure 4.4 along with the comparisons to follow, the FI/CC mode indices are absolute, with the CC mode indices following the FI mode indices. Thus, for the 9×9 panel and its 12 FI modes, CC mode 1 is index 13, CC mode 2 is index 14, etc.

The SVD mode set is ordered by singular value; it turns out that this sorting is opposite the natural order of the fixed-interface modes. The only similar modes are SVD vectors 12 and 13, which correspond most closely to FI mode 1 and CC mode 1, respectively. It is interesting to note that singular vector 16 does not show a strong relationship to *any* of the fixed interface or characteristic constraint modes. The QR basis vectors, on the other hand, bear much more resemblance to the expected ordering of the fixed-interface modes. Indeed, the first 12 QR vectors are precisely the fixed-interface modes; only the localized CC modes of the component are modified by the QR factorization. QR vector 13 bears little resemblance to any of the FI/CC mode set; the final three CC vectors are modified to a lesser extent.

Three orthogonality metrics of interest are now examined for each basis set:

- *Unweighted* orthogonality of the basis vectors with respect to each other, i.e. a “self-MAC” computation.
- Orthogonality weighted through the stiffness matrix. Since the vectors are not normalized to unity with respect to the stiffness matrix, for display, each column of the resulting matrix is normalized with respect to the largest magnitude element of that row.
- *Unweighted* cross-orthogonality (i.e. a “cross-MAC” check) between the basis vectors and the displacements resulting from application of single-mode loadings in a nonlinear FEA code. The

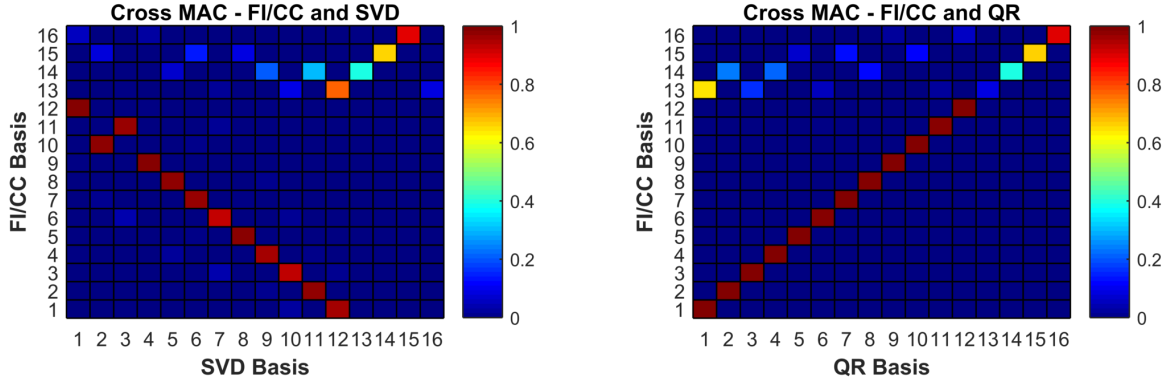


Figure 4.4: *Cross-MAC between the FI/CC modes and (left) the SVD-transformed basis (right) the QR-transformed basis. 9×9 panel only. Modal indices are absolute, with the CC mode indices following the FI mode indices, i.e. for the 9×9 panel and its 12 FI modes, CC mode 1 is index 13, CC mode 2 is index 14, etc.*

intent of this procedure is to compare, in physical space, the shape of each basis vector with the resulting nonlinear displacement from each load; displacement vectors that are difficult to distinguish will result in poor estimates of modal displacement for the NLROM fit procedure.

Each of these quantities are plotted for both plates in Figures 4.5-4.7.

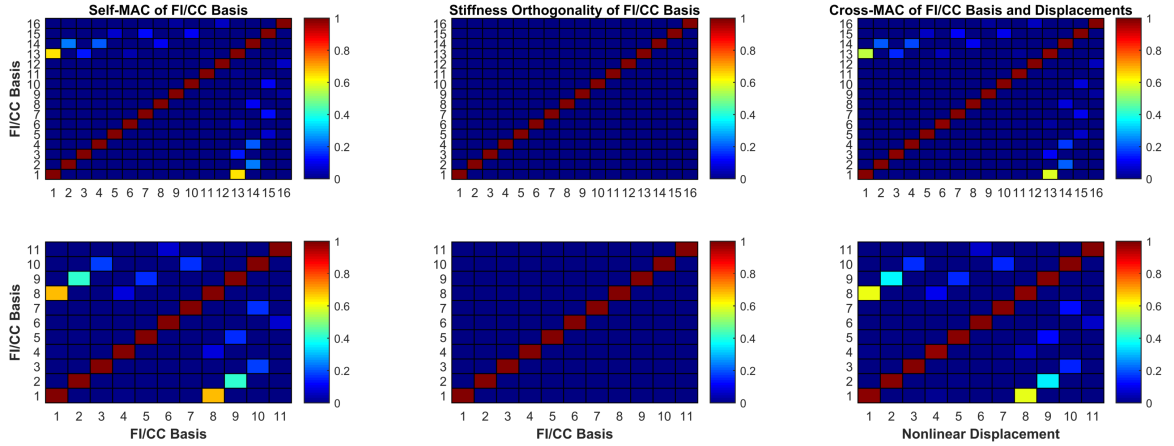


Figure 4.5: *Examination of the FI/CC basis set. Top row corresponds to the 9×9 plate, bottom row the 9×6 plate. (Left): Self-MAC. (Center): Orthogonality check through the stiffness matrix. (Right): Cross-MAC between basis vectors and resulting nonlinear static deformations. Mode indices are absolute, with the CC mode indices following the FI mode indices. Thus, for the 9×9 panel and its 12 FI modes, CC mode 1 is index 13, CC mode 2 is index 14, etc.*

As mentioned previously, the set of FI and CC modes is not necessarily orthogonal with respect to the stiffness matrix, although in this case it appears to be nearly so. The resulting single-mode displacements are not orthogonal to the load basis, either. In contrast, the SVD and QR vectors are

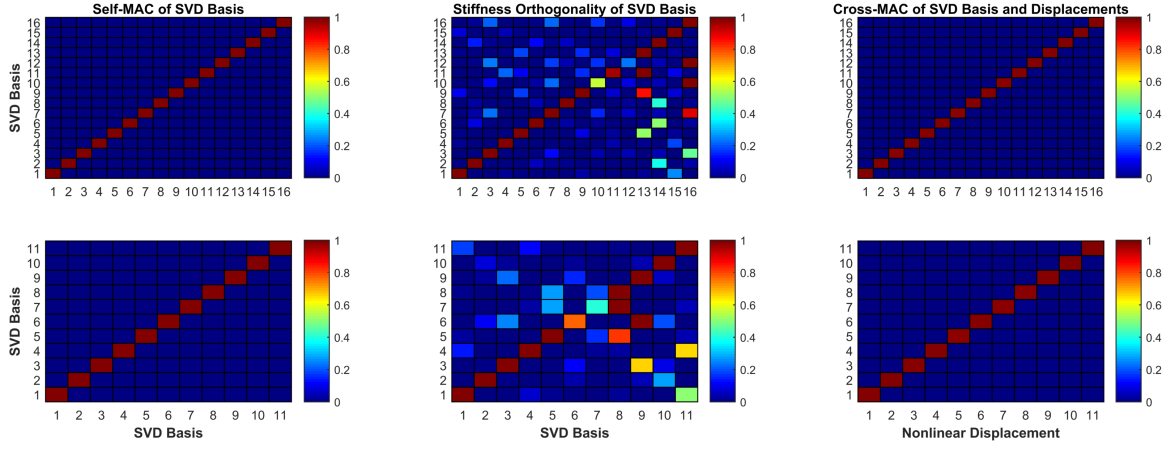


Figure 4.6: *Examination of the SVD basis set. Top row corresponds to the 9×9 plate, bottom row the 9×6 plate. (Left): Self-MAC. (Center): Orthogonality check through the stiffness matrix. (Right): Cross-MAC between basis vectors and resulting nonlinear static deformations. Mode indices are absolute, with the CC mode indices following the FI mode indices. Thus, for the 9×9 panel and its 12 FI modes, CC mode 1 is index 13, CC mode 2 is index 14, etc.*

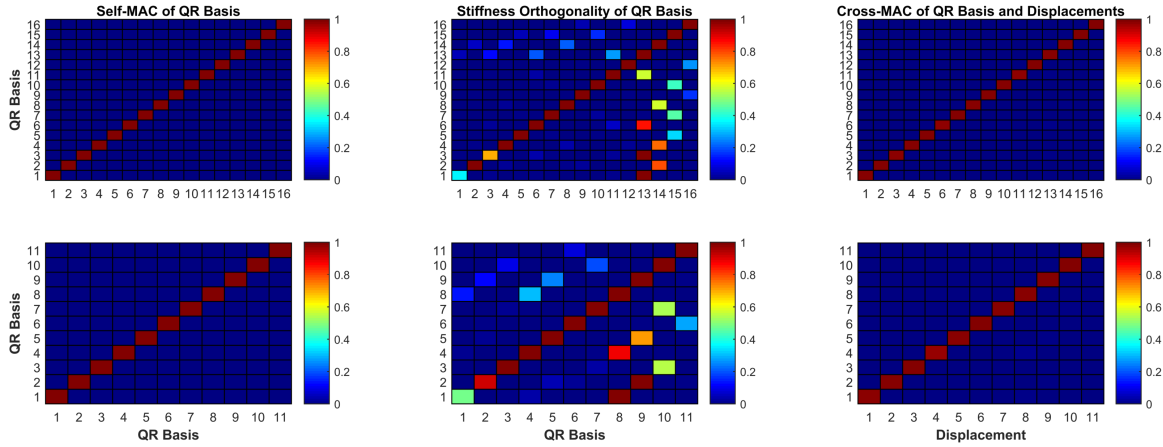


Figure 4.7: *Examination of the QR basis set. Top row corresponds to the 9×9 plate, bottom row the 9×6 plate. (Left): Self-MAC. (Center): Orthogonality check through the stiffness matrix. (Right): Cross-MAC between basis vectors and resulting nonlinear static deformations. Mode indices are absolute, with the CC mode indices following the FI mode indices. Thus, for the 9×9 panel and its 12 FI modes, CC mode 1 is index 13, CC mode 2 is index 14, etc.*

orthogonal to each other, but not through the stiffness matrix. It is somewhat surprising that the nonlinear static displacements from these latter two sets of basis vectors are orthogonal with the force inputs – the ease of distinguishing the resulting displacements from each other emphasizes the objective of applying SVD and QR reductions.

Full-Basis Models

Nonlinear reduced order models containing the full count of fixed-interface and characteristic constraint modes for each component were constructed using each of the three basis types discussed above. Two numerical metrics used to provide an initial estimate of NLROM quality are the *displacement residual* and *force residual error* defined in Equations (3.21) and (3.22) respectively. The former is a measure of how accurately an estimated set of modal displacements is able to recreate the specified set of static deflections. The latter describes how well a set of identified nonlinear coefficients are able to recreate the necessary internal force vector to maintain specified static deflections at a known force level. While neither measure guarantees an accurate NLROM, poor performance on either metric often indicates a poor choice of basis vectors or set of load cases. The percentage errors of each subcomponent NLROM for each basis selection is give in Table 4.7. The error metrics are quite similar for all three basis selections.

Basis Type	9 x 9 Plate			9 x 6 Plate		
	ϵ_{disp} [%]	ϵ_{force} [%]	Load Cases	ϵ_{disp} [%]	ϵ_{force} [%]	Load Cases
FI/CC	1.77	0.526	4992	1.52	0.388	1562
SVD	1.76	0.583		1.53	0.479	
QR	1.73	0.721		1.52	0.477	

Table 4.7: *Fit properties of full-basis NLROMs using FI/CC, SVD, and QR bases.*

For a model of this size, coefficient determination took several hours on a standard desktop machine, and increasing the size of the basis set beyond the 12 fixed interface modes and 4 characteristic constraint modes of the 9×9 plate would have been prohibitive.

Nonlinear normal mode validation of each resulting NLROM was performed on the first NNM only. Full-basis results are shown in Figure 4.8. Along with the NLROM computed from a full-order assembly, the NNM computed from Kuether’s model is also shown. All substructured models agree completely over the depicted energy range, with all four diverging from the assembly ROM at 135 Hz. (This divergence may correspond to an internal resonance of the system not captured by the assembly NNM, but is not investigated further.) These results serve as a baseline for comparisons below.

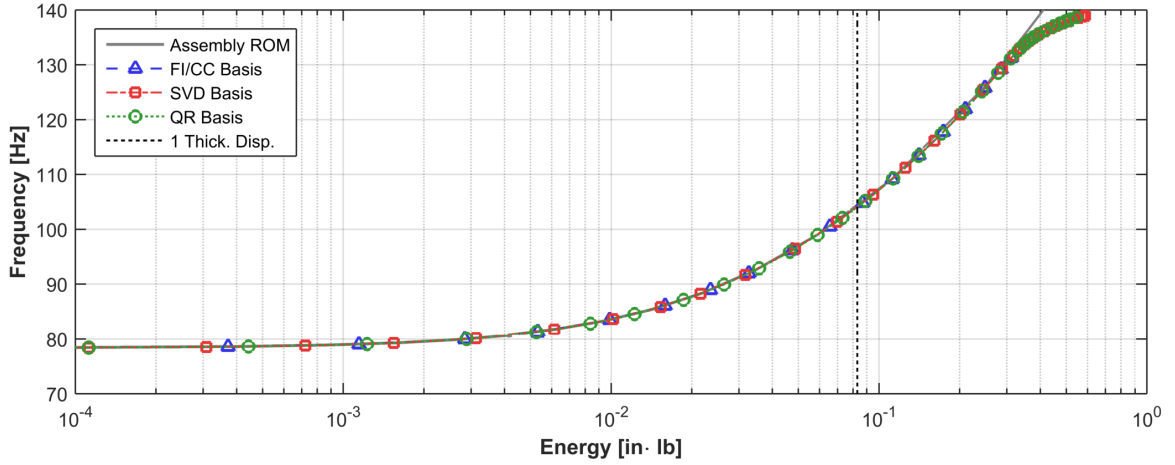


Figure 4.8: *NNMs computed using ROMs constructed from full FI/CC, SVD, and QR bases.*

Reduced Basis Models

From the number of load cases required to construct the NLROMs above, it is clear that smaller basis sets are of interest. In monolithic NLROMs, it is quite common to select only a few vibration modes of the structure (almost always less than ten, sometimes as low as two or three) to serve as a basis for the nonlinear forcing. Intuitively, one might expect that this practice could be imitated by selecting only the lowest few modes of the relatively large fixed-interface set, leaving the higher FI modes purely linear. This was achieved by removing individual modes from the basis set, conducting the nonlinear fit, and computing NNMs of the resulting NLROM. Note that substructure modes were not removed from the linear model, instead, any modes omitted from the basis were simply assigned nonlinear restoring force coefficients of zero.

As Kuether previously demonstrated in [13], attempting to remove all four of the CC modes leads to a model which is far too soft in its first NNM, as shown in Figure 4.9. However, retaining the first three FI modes and only a single CC mode leads to an NNM backbone that matches the assembly result up to 120 Hz, before encountering convergence issues. Including the first five FI modes and first two CC modes allows further convergence, although a spurious internal resonance is observed. A tradeoff between the valid energy range of the NNM and the number of modes in the basis set clearly exists in this instance.

With reduced models performing well using the FI/CC basis, reduction was also examined using the QR basis. The non-sequential behavior of the SVD basis with respect to the FI modes was not desirable and a reduced basis of the singular vectors was not constructed. The resulting NNMs are shown in

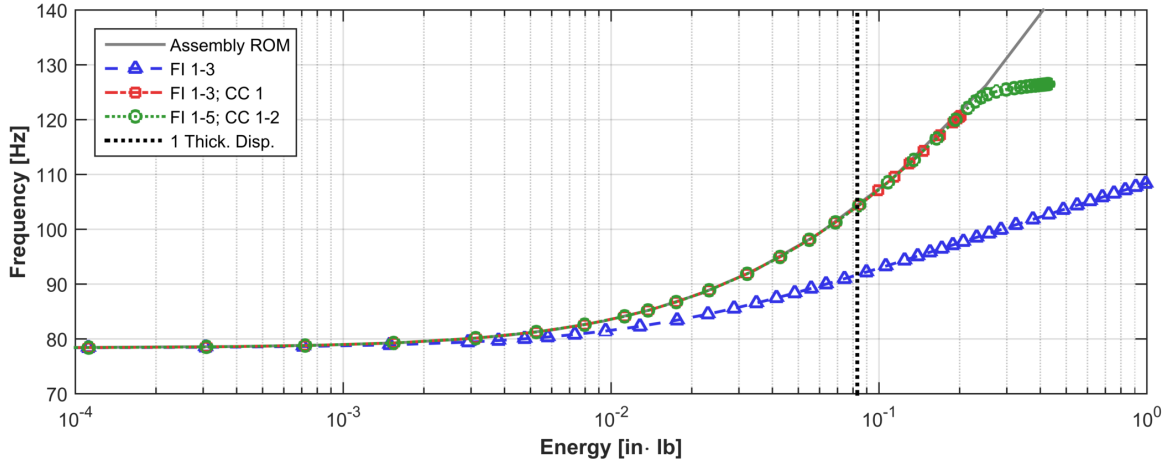


Figure 4.9: NNMs computed using ROMs constructed from the FI/CC basis with various modes removed. Figure legend indicates vectors included in the basis set, i.e. “FI 1-3; CC 1” indicates that fixed interface modes one through three and characteristic constraint mode one were included in each component’s nonlinear basis.

Figure 4.10. Three cases were examined, as described below:

- **Case A:** QR vector 1 (corresponding to FI mode 1) of each plate was included along with the QR vector associated with CC mode 1 – for the 9×9 plate, this was QR vector 13, and for the 9×6 plate, QR vector 8.
- **Case B:** QR vectors 1-3 (corresponding to FI modes 1-3) of each plate were included along with the QR vector associated with CC modes 1-2 – for the 9×9 plate, these were QR vectors 13-14, and for the 9×6 plate, QR vectors 8-9.
- **Case C:** QR vectors 1-5 (corresponding to FI modes 1-5) of each plate were included along with the QR vector associated with CC modes 1-2 – for the 9×9 plate, these were QR vectors 13-14, and for the 9×6 plate, QR vectors 8-9.

For these models, the resulting NNMs were uniformly too stiff, and also displayed spurious resonances prior to reaching the one-thickness displacement level. While it was possible to use alternate basis vectors with a fully populated basis set, reducing the size of that set was not possible for these plates. A contrasting example of the utility of QR vectors, applied to a different model, is presented in Section 4.2.4 below.

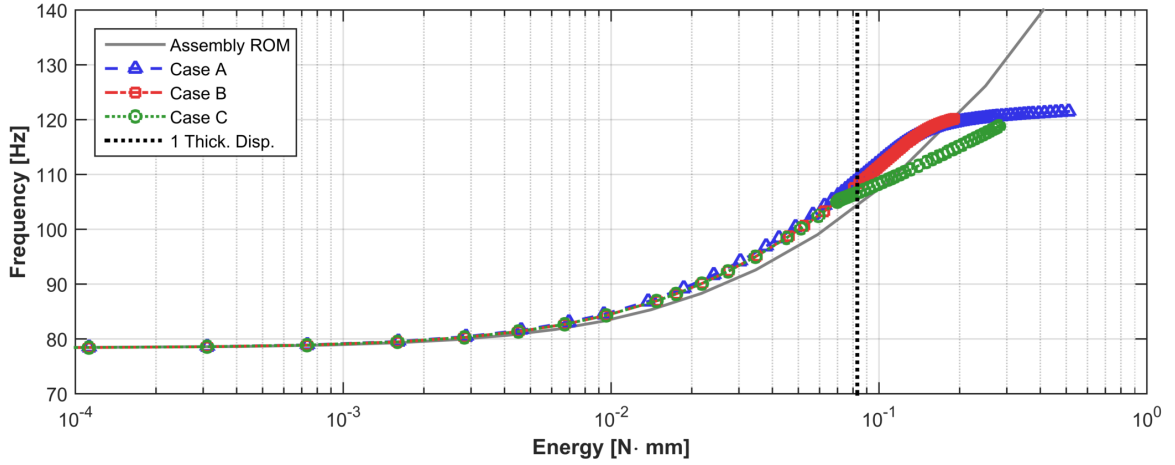


Figure 4.10: *NNMs computed using ROMs constructed from the QR basis with various vectors removed. See the itemized list above for a description of each case displayed in the legend.*

4.2 Panel/Stiffener Model

Realistic aerospace structures are significantly more complicated than the proof-of-concept example presented above. To evaluate the ability of these nonlinear substructuring techniques to handle more representative structures, a second example was formulated. Requirements for this example structure were:

- At least three components, in order to expose any effects related to multiple boundary interfaces.
- A configuration similar to the panel/stiffener construction used on many aircraft.
- A sufficient number of interface degrees of freedom suitable for reduction using characteristic constraint modes.
- Strong nonlinear effects only in the “panel” portion of the model.
- No boundary conditions on the “panel” portion in an unassembled state.

This last item turns out to be the most critical, since the geometric nonlinearity of thin beams and panels is intimately related to the boundary conditions of those structures. Further, the ICE method of NLROM generation is not directly applicable to free-free structures. These difficulties will be discussed in Section 4.2.3. First, an overview of the model and its linear representation is presented.

4.2.1 Linear Substructuring

A truncated section of a panel supported by hat stiffeners meets the above requirements. Structural, material, and mesh properties of the finite element model are summarized in Tables 4.8 and 4.9.

Part	Young's Modulus [MPa]	Density [kg/m ³]	Thickness [mm]
Panel	71000	2700	1.5
Stiffener [Soft]			4.0
Stiffener [Stiff]			

Table 4.8: *Material and structural properties of the truncated panel/stiffener assembly components.*

Part	Nodes	S4R Elements	DOF
Panel	182	150	1092
Stiffener [Soft]	105	84	630
Stiffener [Stiff]			
Assembly	392	318	2352

Table 4.9: *Mesh properties of the truncated panel/stiffener assembly components.*

The fully assembled structure is shown in Figure 4.11. The five retained fixed interface modes of the panel are shown in Table 4.10. Modes one and three are symmetric bending modes, modes two and five are asymmetric bending modes, and mode four is a torsional mode.

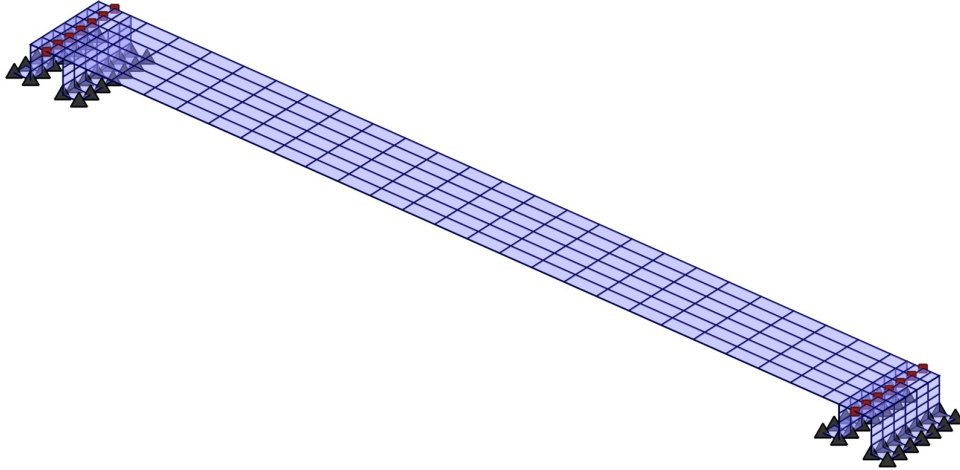
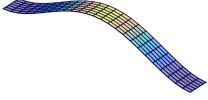
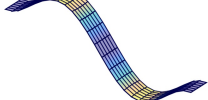
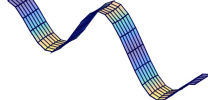
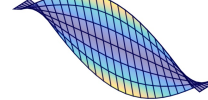
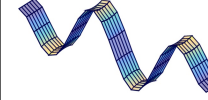


Figure 4.11: *Assembled panel/stiffener model. Black triangles denote boundary conditions (all clamped in this case) while red squares denote coupling points (all degrees of freedom).*

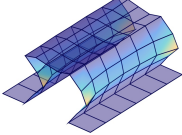
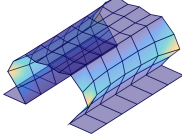
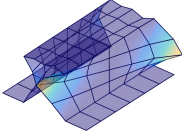
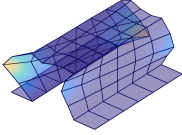
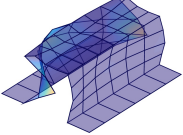
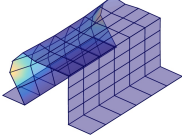
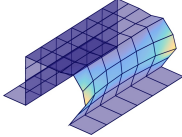
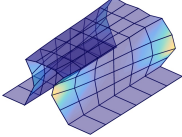
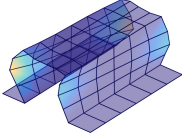
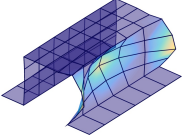
Retained fixed interface modes of the hat stiffeners for soft and stiff assemblies are shown in Table 4.11. Even though these modes are at very high frequencies and begin to push the spatial limitations of the coarse mesh, including five fixed interface modes in each stiffener is necessary in order to obtain

Table 4.10: *Retained fixed interface modes of the panel.*

				
Mode 1: 32.3 Hz	Mode 2: 89.7 Hz	Mode 3: 178.2 Hz	Mode 4: 198.6 Hz	Mode 5: 300.0 Hz

more than a handful of modes for the full assembly.

Table 4.11: *Retained fixed interface modes of the “soft” (top) and “stiff” (bottom) stiffeners.*

Soft Component (1.5 mm Thickness)				
				
Mode 1: 20.2 kHz	Mode 2: 20.2 kHz	Mode 3: 20.4 kHz	Mode 4: 20.4 kHz	Mode 5: 21.9 kHz
Stiff Component (4mm Thickness)				
				
Mode 1: 40.6 kHz	Mode 2: 40.6 kHz	Mode 3: 40.8 kHz	Mode 4: 40.8 kHz	Mode 5: 43.8 kHz

The five retained characteristic constraint modes for each model are shown in Table 4.12. CC mode 1 of each structure is similar to a pinned bending mode – note that the frequency of “soft” CC mode 1 is roughly one quarter the frequency of the “stiff” counterpart. CC mode 4 in each structure is a vertical displacement of the panel on its supports, with the soft structure also showing a rotational displacement of the panel in CC mode 5. By inspection, the most critical modes for panel nonlinearity are CC mode 1 on both structures, mode 2 on the soft structure, and mode 3 on the stiff structure.

Modes of the assembled system are shown in Table 4.13. A modal assurance criterion and frequency error check are provided in Figure 4.12. Frequency errors remain below 0.1% for the first five modes of each structure, after which the substructured models immediately lose all accuracy. Tabulated values for the modal comparisons are given in Appendix B, Tables B.4 and B.5 for the soft and stiff assemblies, respectively.

Table 4.12: *Characteristic constraint modes of the “soft” (top) and “stiff” (bottom) assembled models.*

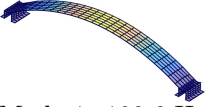
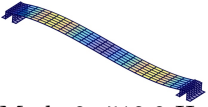
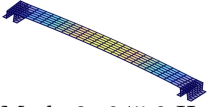
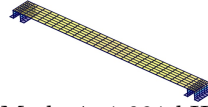
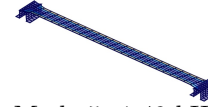
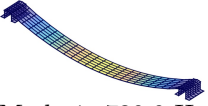
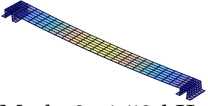
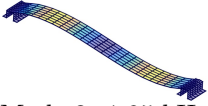
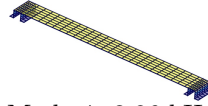
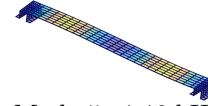
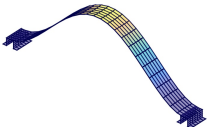
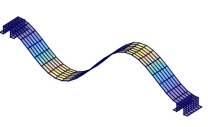
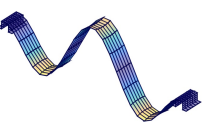
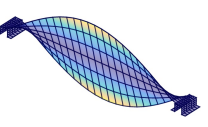
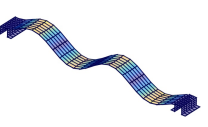
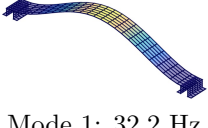
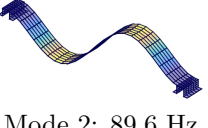
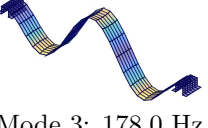
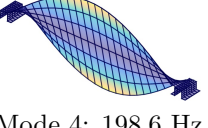
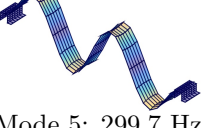
Soft Component (1.5 mm Thickness)				
				
Mode 1: 199.6 Hz	Mode 2: 512.2 Hz	Mode 3: 945.8 Hz	Mode 4: 1.091 kHz	Mode 5: 1.49 kHz
Stiff Component (4mm Thickness)				
				
Mode 1: 730.0 Hz	Mode 2: 1.58 kHz	Mode 3: 1.95 kHz	Mode 4: 3.86 kHz	Mode 5: 4.46 kHz

Table 4.13: *Vibration modes of the assembled model, computed with the fixed-interface and characteristic constraint modes shown in Tables 4.10, 4.11, and 4.12*

Soft Component (1.5 mm Thickness)				
				
Mode 1: 31.9 Hz	Mode 2: 88.5 Hz	Mode 3: 176.0 Hz	Mode 4: 197.2 Hz	Mode 5: 296.0 Hz
Stiff Component (4mm Thickness)				
				
Mode 1: 32.2 Hz	Mode 2: 89.6 Hz	Mode 3: 178.0 Hz	Mode 4: 198.6 Hz	Mode 5: 299.7 Hz

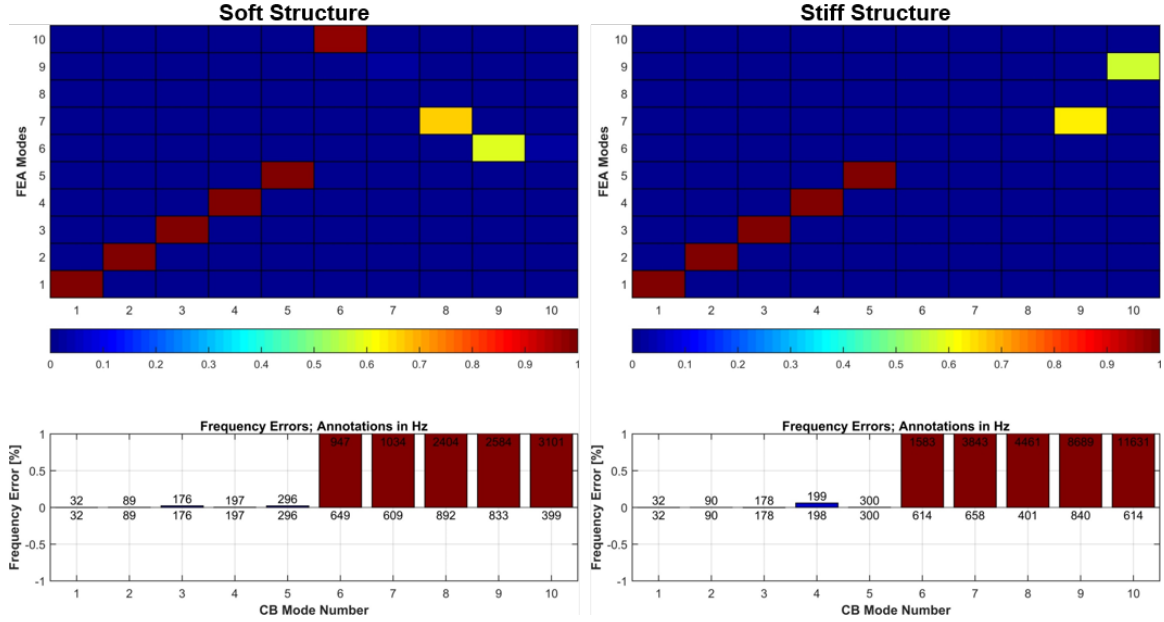


Figure 4.12: (Top): Cross-MAC between full-order FEA truth modes and substructure modes. (Bottom): Frequency errors between truth and substructure modes, based on matching MAC value; frequency values along the horizontal axis are full-order values while those adjacent to error bars are the substructured values.

With the first five modes of each structure accurately represented up to 300 Hz, the Craig-Bampton/Characteristic Constraint substructuring method reduces each model from 2,352 to 20 total degrees of freedom.

4.2.2 Reference Nonlinear Model

Before constructing substructured reduced-order models of the assembly, traditional NLROMs were formed to serve as truth models of the system’s nonlinear dynamics. Reduced order models using mode 1 only, modes 1-3, and modes 1-5 were constructed and used to compute the first nonlinear normal mode of each assembly. NNM convergence and periodicity studies (with “periodicity” defined by Equation (2.20)) of these NLROMs are shown below.

The computed NNM backbones and associated periodicity errors of the stiff assembly are shown in Figure 4.13. The three and five-mode models maintain periodicity errors below 1% over the entire range of interest; error in the one-mode model jumps significantly above the one-thickness displacement level. The bulk of this error is due to the lack of mode three in the initial conditions at these higher energy levels. Soft assembly NNMs and periodicity errors are shown in Figure 4.14. In this case, all three models are accurate below energy levels of $10 \text{ N} \cdot \text{mm}$, after which periodicity errors spike dramatically.

This is due to convergence issues in the finite element model at large displacements; the structure either physically buckles or requires a finer mesh in order to achieve convergence at such high energy levels. This discrepancy aside, the three and five-mode models are accurate up to frequencies of roughly 40 Hz.

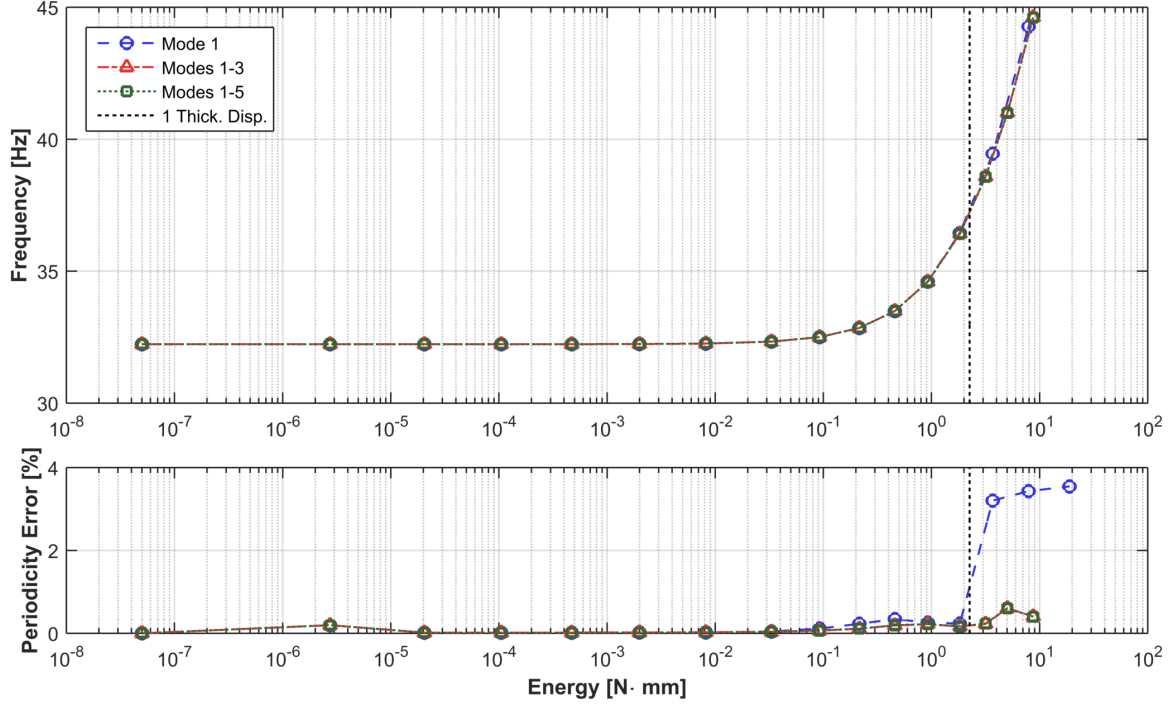


Figure 4.13: (Top) NNMs computed using one, three, and five-mode ROMs of a fully assembled FEA model with “stiff” supports. (Bottom) Periodicity errors associated with each computed backbone curve.

For reference, the soft and stiff model NNMs are plotted together in Figure 4.15, along with an NNM corresponding to a fully-constrained FEA model of the panel only. As expected, this latter model shows the highest amount of nonlinear stiffening with increasing energy, followed closely by the stiff assembly. These two models also have nearly identical linear natural frequencies, indicating that the stiff assembly approximates a “built-in” set of boundary conditions. The soft assembly, by contrast, has a somewhat lower linear natural frequency and displays significantly less nonlinear stiffening – the effects do not appear until higher energy levels, and the frequency increases more slowly than the other two models. These three NNM curves will be used during inspection of the substructured NLROM results below in order to better understand the behavior of each assembled model.

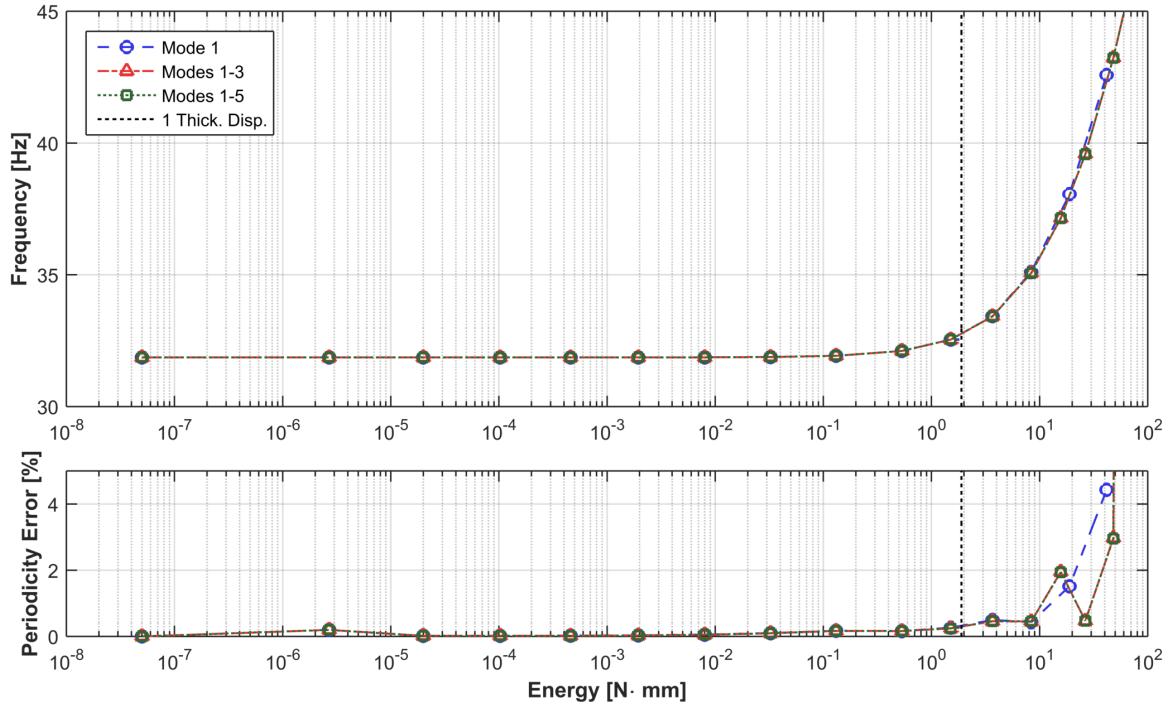


Figure 4.14: (Top) NNMs computed using one, three, and five-mode ROMs of a fully assembled FEA model with “soft” supports. (Bottom) Periodicity errors associated with each computed backbone curve.

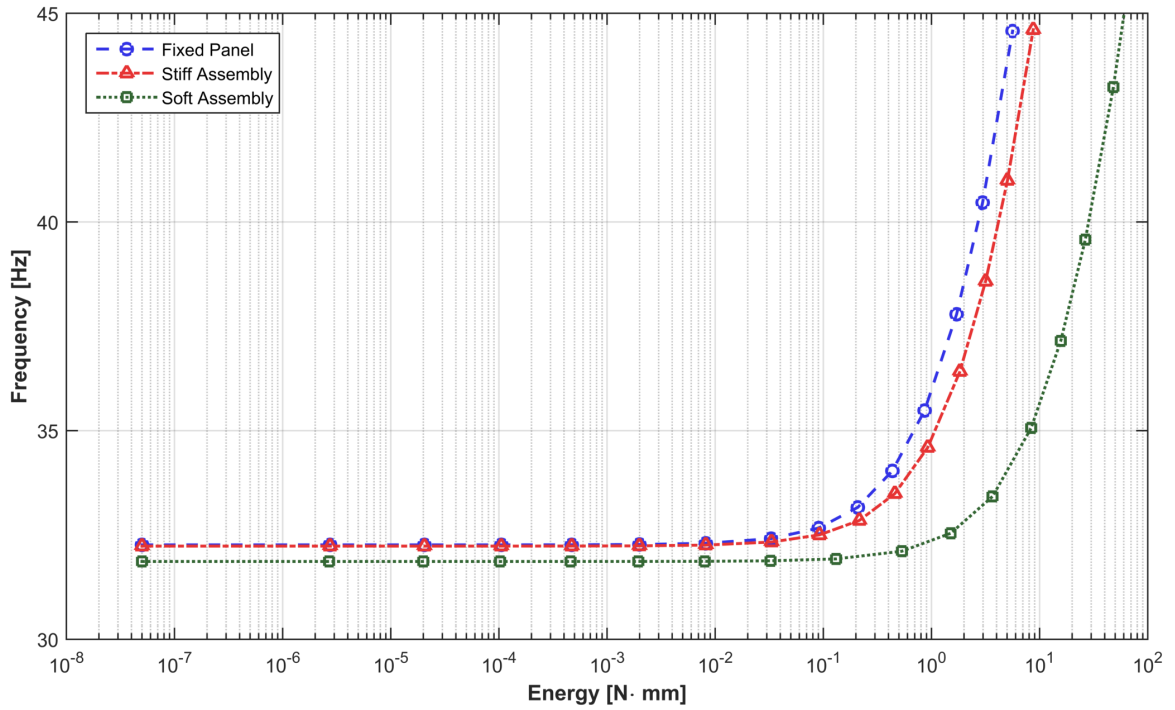


Figure 4.15: Truth NNMs of the soft and stiff assemblies along with a fully-fixed FEA model of the panel only.

4.2.3 Nonlinear Substructuring

Nonlinear substructuring is conducted on the assumption that only the panel component be treated as nonlinear, reducing the number of required load cases to specify each NLROM; this assumption is justified based on the extreme natural frequencies of the stiffeners relative to the panel and assembly modes. Only a subset of the lowest fixed interface and characteristic constraint modes are used to specify the NLROMs, further reducing the number of load cases required for the model. Since the QR transformation yields a more physically intuitive ordering of the basis vectors than the SVD transformation, only the former method is used for the remainder of this chapter, along with the unaltered set of fixed interface and characteristic constraint modes.

The key difficulty associated with this model lies in the panel's lack of boundary conditions in its unassembled state. Immediately this raises an issue with the nonlinear static FEA solutions that must be obtained, since baseline static solvers cannot handle free-free structures. "Inertia relief" (IR) procedures, which allow a static solution by applying forces to eliminate rigid body motion of the structure [43], can overcome this limitation. Unfortunately, the use of inertia relief for the ICE method is not yet well-understood. Further, there is a more critical problem to be overcome: physically, the nonlinearity of the panel will be dominated by its interaction with the supports, a fact that would not be addressed by using an IR solution procedure. The panel's fixed interface modes correspond to an unphysical infinite stiffness at the boundaries, while the characteristic constraint modes are associated with the stiffness of the assembly, statically reduced to the set of boundary nodes. A single, consistent set of boundary conditions must be selected for use in the nonlinear, static FEA routine. It is not possible to use fully-fixed boundary conditions on FI mode load cases and statically reduced boundary conditions on CC modes, since the modal displacements are inherently coupled and their stiffness coefficients must be estimated in concert with each other.

A perspective on this topic is provided by an example given by Kuether [15] in which a pinned beam, with one end on axial rollers, is attached to a single axial spring at the endpoint. As with the system discussed here, the nonlinearity of the beam was dependent on the stiffness of the attached spring, although in [15] a direct application of the ICE method to the FI/CC basis resulted in an accurate NLROM. Two key distinctions between the beam/spring example and the panel/stiffeners example used here must be made:

- For the beam/spring system, the single constraint mode was an axial mode of the beam. Rather

than relying on implicit condensation of membrane stretching in the structure, which generally occurs when using the ICE method, the axial displacement was modeled explicitly via inclusion of a membrane mode in the NLROM basis, which essentially served as a “dual mode” for the system. In the general case (including the system used here), axial modes of the structure *are not* included in the characteristic constraint mode set.

- Since the beam was constrained in three degrees of freedom, it remained statically determinate and could be solved directly in a static FE code with no modifications to the boundary conditions or consideration of an inertia relief routine.

With all of these considerations in mind, it is clear that some combination of alternate procedures must be devised to properly handle the panel in this example. Three possible solutions are examined in the sections below. First, to illustrate the issues caused by inaccurate boundary conditions, an NLROM was constructed using only the fixed-interface modes with fully constrained boundary conditions. Next, NLROMs were constructed using both FI and CC modes with an approximation of the linear assembly stiffness applied to the boundaries of the panel. This approximation was achieved by statically reducing the assembly stiffness to each boundary degree of freedom on the panel and applying the resulting stiffness values as a set of grounded springs at each degree of freedom. Finally, an “*in situ*” technique was used, with loads applied to the panel on a full finite element model of the assembly.

Fixed Interface Nonlinear Substructuring

As a starting point, models with fixed interface modes only were constructed. The fully-fixed boundary conditions associated with these FI modes were used here. While it was possible to include CC modes in the force basis by applying appropriate force vectors to the finite element model, the fully-fixed boundary conditions would not have admitted constraint deformation, leading to CC mode nonlinear coefficients approaching infinity. The non-physical boundaries on the panel should not be expected to yield an accurate nonlinear fit in any case, so the omission of CC modes is no cause for concern here.

NLROMs containing the first three fixed interface modes of the panel were constructed for the stiff and soft assemblies, with the resulting NNMs shown in Figure 4.16. NNMs of monolithic NLROMs corresponding to the fully-fixed panel and the relevant assembly are also shown in each pane of the figure.

In both cases, the FI-only NNM backbone tracks closely with the panel-only backbone, indicating

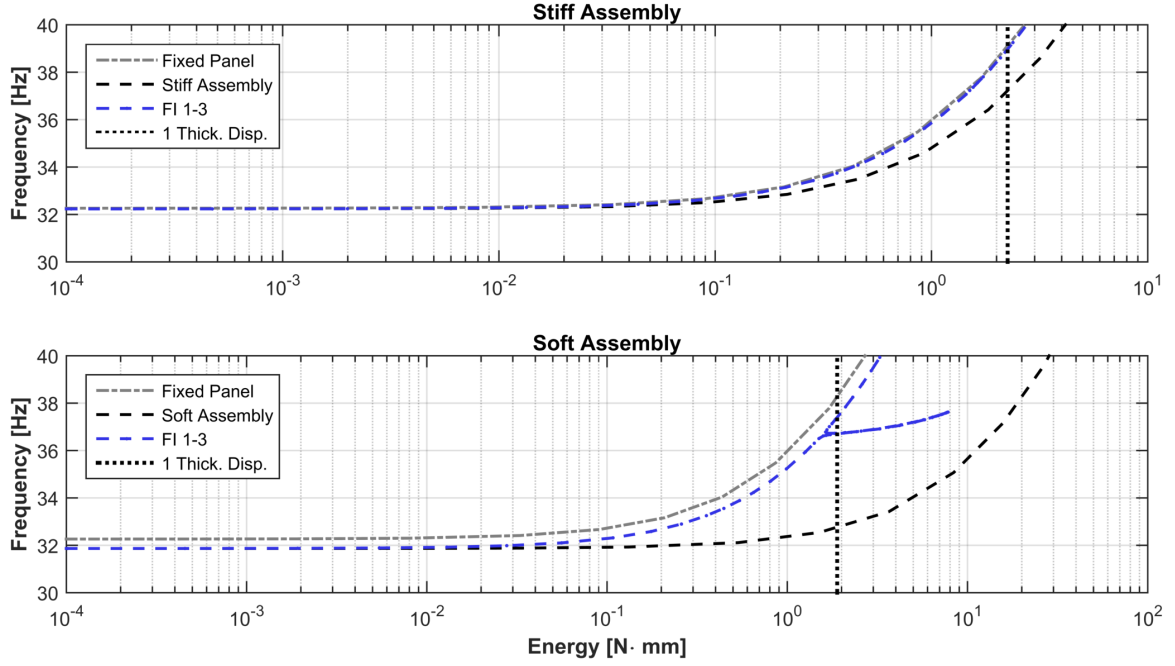


Figure 4.16: *NNMs computed from substructured NLROMs using only fixed interface modes as a basis for the nonlinear forces and fully-fixed boundary conditions for the ICE load cases.*

that the nonlinear stiffness is not determined appropriately when the panel boundaries are fully fixed. Since the linear substructuring is still accurate, the NNM backbone of the soft assembly still maintains the correct linear natural frequency at low amplitudes, but ends up tracking the fixed panel’s frequency behavior at higher energies.

These results are exactly what should be expected from the ICE method, since in neither case is the panel’s nonlinear stiffness affected by the underlying stiffness of its boundaries – the fixed interface modes of the panel are identical in both assemblies. Including characteristic constraint modes in the force basis would at least provide some measure of differentiation between the two models; as discussed earlier, however, the CC modes cannot be included if the boundary nodes are fixed, and it is not possible to apply load combinations with FI and CC force vectors if disparate boundary conditions are used on the two subsets of modes. The fixed set of boundary conditions cannot be used to compute component NLROMs for this model.

Static Reduction of Interface Stiffness

A natural method to overcome the difficulty of boundary condition specification is to place component finite element models on a linear base which represents the underlying stiffness of the assembly. This

information can be determined directly from the component stiffness matrices and the substructure's assembly matrix. The only difficulty lies in omitting the stiffness of the nonlinear component of interest. The procedure is described below; the reader may find Section 3.2 useful as a reference to the nomenclature in use.

The linear assembly interface stiffness, as seen by each component, can be determined from the system matrices used to create the substructured assembly. It is convenient to partition the model using the *unassembled* set of boundary degrees of freedom, \hat{b} , along with the *assembled* set of boundary degrees of freedom \hat{a} . Figure 4.17 illustrates the nomenclature by using MATLAB's *spy* command on the system assembly matrix \mathbf{L} .

Unassembled coordinates are displayed along the y axis and assembled coordinates along the x axis; the fixed interface modal coordinates at the left of the plot can be disregarded. The boundary DOF are visible at right, and the set of coordinates on the x axis from 16 to 99 comprises the set \hat{a} . The associated y axis coordinates forms the set \hat{b} . These partition sets yield a stiffness matrix $\hat{\mathbf{K}}_{\hat{b}\hat{b}}$ (which is obtained from the unassembled matrix $\hat{\mathbf{K}}_{CB}$) and an assembly matrix $\mathbf{L}_{\hat{b}\hat{a}}$ (which corresponds to the unshaded portion of Figure 4.17).

To determine the interface stiffness as seen by the j^{th} component, the subset of boundary coordinates in \hat{b} belonging to component j – the panel, in this instance – are determined and designated as set \hat{j} . Their corresponding rows are zeroed to leave an augmented assembly matrix $\mathbf{L}_{\hat{b}\hat{a}}^{\hat{j}}$ (the unshaded portion of Figure 4.17 which lies *above* the dashed line will contain the only nonzero entries). This decouples component j from the rest of the assembly – clearly, the stiffness corresponding to this component should not be included in the boundary stiffness calculation. Once $\mathbf{L}_{\hat{b}\hat{a}}^{\hat{j}}$ is formed, an “augmented” boundary stiffness matrix is computed,

$$\hat{\mathbf{K}}^{\hat{j}} = (\mathbf{L}_{\hat{b}\hat{a}}^{\hat{j}})^T \hat{\mathbf{K}}_{\hat{b}\hat{b}} \mathbf{L}_{\hat{b}\hat{a}}^{\hat{j}}$$

which is the assembled stiffness matrix of the system, absent component j . This matrix is in turn partitioned to the boundaries of component j along with the remaining boundary degrees of freedom, \hat{i} , which is the relative complement of \hat{j} with respect to \hat{b} ; i.e. \hat{i} contains all of the indices from \hat{b} which

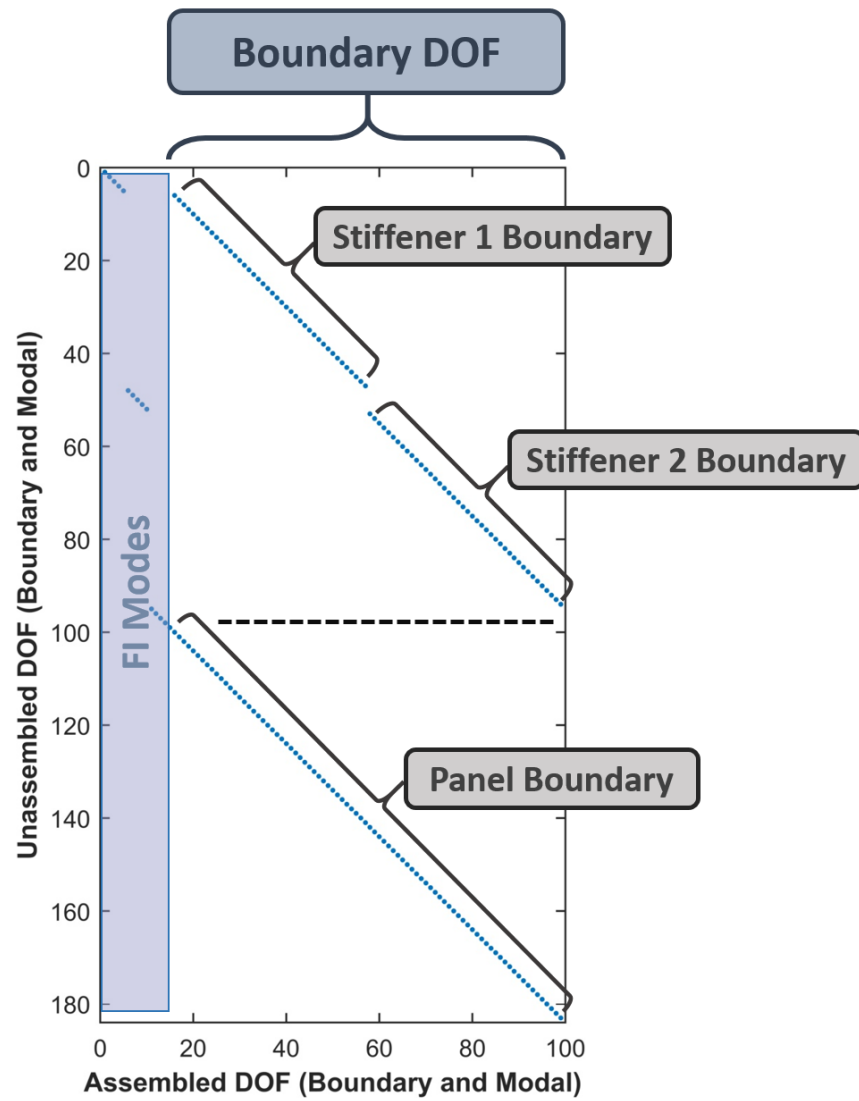


Figure 4.17: Annotated plot of MATLAB's *spy* command applied to the system assembly matrix \mathbf{L} of this section's example.

are not found in \hat{j} . With this partition, the static system of equations for the augmented assembly is

$$\begin{bmatrix} \hat{\mathbf{K}}_{ii}^{\hat{j}} & \hat{\mathbf{K}}_{ij}^{\hat{j}} \\ \hat{\mathbf{K}}_{ji}^{\hat{j}} & \hat{\mathbf{K}}_{jj}^{\hat{j}} \end{bmatrix} \begin{Bmatrix} \hat{\mathbf{q}}_i \\ \hat{\mathbf{q}}_j \end{Bmatrix} = \begin{Bmatrix} \mathbf{0} \\ \mathbf{f} \end{Bmatrix} \quad (4.1)$$

Note that $\hat{\mathbf{q}}_j = \mathbf{x}_b^j$, the boundary set of degrees of freedom on component j . From the top row, the familiar static reduction is obtained;

$$\hat{\mathbf{q}}_i = -(\hat{\mathbf{K}}_{ii}^{\hat{j}})^{-1} \hat{\mathbf{K}}_{ij}^{\hat{j}} \mathbf{x}_b^j$$

Using this relation in the bottom row leads to a force/displacement expression for the boundary of interest:

$$[\hat{\mathbf{K}}_{jj}^{\hat{j}} - \hat{\mathbf{K}}_{ji}^{\hat{j}} (\hat{\mathbf{K}}_{ii}^{\hat{j}})^{-1} \hat{\mathbf{K}}_{ij}^{\hat{j}}] \mathbf{x}_b^j = \hat{\mathbf{K}}_b^{\hat{j}} \mathbf{x}_b^j = \mathbf{f} \quad (4.2)$$

$\hat{\mathbf{K}}_b^{\hat{j}}$, the Schur complement of $\hat{\mathbf{K}}_{jj}^{\hat{j}}$ from (4.1), is the interface stiffness matrix as seen by the j^{th} component. Once obtained, two approaches are possible:

- The full matrix can be applied to the nonlinear component of interest within the FEA solver used for NLROM construction. This approach can be cumbersome, particularly for commercial codes.
- The matrix can be statically reduced to each degree of freedom, resulting in an approximation that is analogous to a set of direct spring connections to ground at each DOF. Such a set of springs is straightforward to apply to the boundaries of a component.

The latter approach was used here. Figure 4.18 compares with the linear stiffness at each DOF computed with the process above to values obtained from a series of static, linear perturbation load cases performed on the FEA model in sequence on the stiffener boundaries.

4.2.4 Nonlinear Substructuring with Statically Reduced Interface Stiffness

With boundary stiffnesses obtained from the process above, load cases including both the fixed-interface and characteristic constraint modes can be used, and both types of modes may now be included in the nonlinear force basis. Figure 4.19 depicts the NNMs associated with models constructed from a different

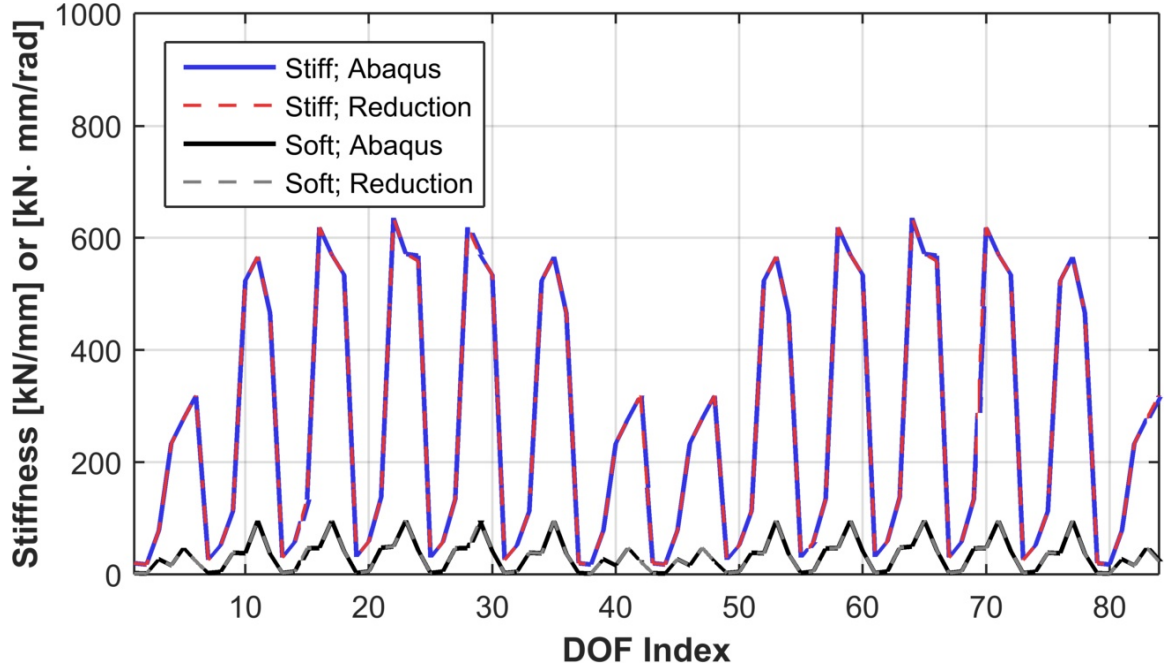


Figure 4.18: *Statically reduced boundary stiffnesses computed using Equations (4.1) and (4.2) compared to manually obtained linear stiffness values from Abaqus static FEA simulations.*

sets of fixed interface and characteristic constraint modes. For two of the NLROMs, only the first three FI modes were used; two others included the first CC mode as well. (CC mode 1 is a dominant “bending” characteristic constraint mode, see Table 4.12).

NNMs associated with the FI-only models show slight softening relative to the fully-fixed panel, but are still quite far from the desired truth backbones. Additionally, the NNMs computed from the combined FI/CC basis set do not converge well, with both models failing well before reaching a displacement level of one thickness. Addressing the first issue, the linear approximation to the boundary conditions is clearly insufficiently accurate to produce valid NLROMs using implicit condensation. This is surprising, given that the stiffeners do not undergo large deformations compared to the deformations of the panel, but there is little to be done. It remains an open question whether using the fully-coupled stiffness matrix from (4.2) will lead to an accurate NLROM, but such a procedure was not attempted due to the difficulty involved. It may also be the case that the boundary stiffness experienced by each node, rather than stiffness coupling between nodes, dominates membrane stretching in the panel; in which case it is the linear boundary approximation itself, rather than the static reduction, that is at fault for the poor models.

The convergence issues associated with NLROMs containing fixed interface mode one is a separate

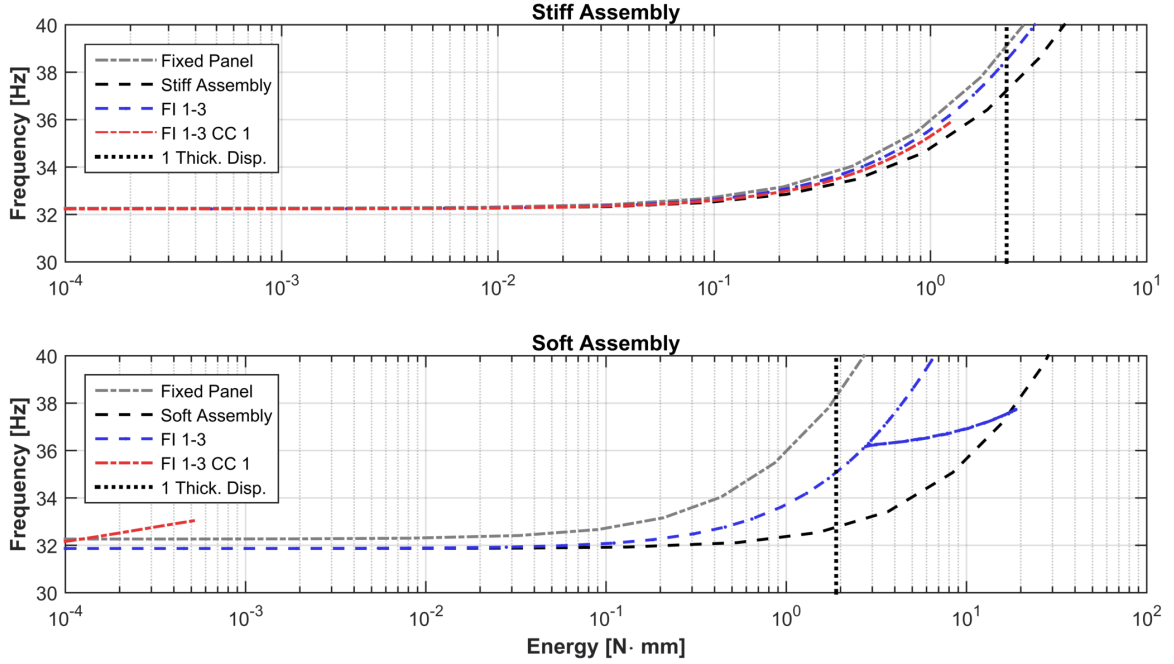


Figure 4.19: *NNMs computed from substructured NLROMs using FI and CC modes as a basis for the nonlinear forces, with grounded springs applied at the boundaries according to static reduction of the stiffness matrix in (4.2). In both cases, including CC mode 1 led to a poor nonlinear fit and spurious/non-convergent NNM backbones.*

issue, and is related to the similarities between the deformations of the panel's first FI mode and the first CC mode of the assembly (refer to Tables 4.10 and 4.12 for visual depictions of the FI and CC modes, respectively). The consequences of this similarity can be observed from the displacement error metrics of each of the above nonlinear models, which are shown in Table 4.14.

	Disp. Error [%]	Force Error [%]
FI 1-3; Stiff Assembly	3.47	0.116
FI 1-3; CC 1; Stiff Assembly	5.88	0.704
FI 1-3; Soft Assembly	32.0	0.0157
FI 1-3; CC 1; Soft Assembly	44.0	1.50

Table 4.14: *Fit properties of NLROMs constructed using component finite element models grounded to statically reduced stiffness at each boundary degree of freedom.*

In both cases, adding the characteristic constraint mode to the basis set increased both the displacement error and force error residuals from the NLROM construction process, leading to poor coefficient fits for the nonlinear restoring force.

Both the inaccurate boundary condition and poor distinction between load basis vectors must be rectified prior to obtaining accurate NLROMs. It turns out that the QR transformation discussed earlier

offers a means to include the CC mode displacements in the basis, however, refinement of the system boundary conditions was determined to be the more pressing need, and is addressed immediately in the following section.

Full-Order *in Situ* Substructuring Method

The results above display that a linear approximation to the component boundary conditions is not sufficiently accurate for use with the implicit condensation method. Rather than attempting to formulate more esoteric representations for the boundary stiffness, it is convenient to simply refer to the most accurate possible representation: A full-order finite element model of the assembly, which provides a limiting case for the utility of nonlinear substructuring given the most accurate possible component boundaries. The procedure is straightforward – ICE load cases are applied to the subset of DOF corresponding to the component of interest in the FEM, while the remaining DOF are left unloaded. The resulting displacements of that DOF subset are extracted and used in the NLROM construction procedure as per usual, leading to a set of coefficient specifications. Since it takes place within the full-order model of the assembly, this approach is referred to as the *in situ* substructuring method. The procedure may initially seem indistinguishable from the construction of a monolithic NLROM of the assembly; it is critical to realize that the loads in this instance are being applied only to single components, as opposed to the monolithic approach which uses modes of the entire assembly. Practically speaking, this still dramatically reduces the number of load cases required to specify an NLROM, as will be discussed below in Section 4.4.

Sets of modes identical to those from Figure 4.19 were used with the *in situ* procedure and backbones of the first NNM were again generated, with the resulting curves shown in Figure 4.20. As one would hope, the NNM backbones of the substructured models finally lie close to those of their respective assemblies. The stiff structure shows nearly perfect agreement, although a slight discrepancy and unexpected internal resonance is visible in the NNM backbone of the soft structure.

Again, however, models including the first CC mode do not converge to appreciable energy levels. Since the boundary condition issue has been addressed for now, the convergence issue is targeted using an alternate basis for the NLROM’s nonlinear restoring force; the QR transformation is selected for its more intuitive mode selection process compared to the SVD transformation. The first three QR vectors correspond to the first three FI modes of the panel, while QR vector six corresponds to the components of CC mode 1 orthogonal to all of the panel’s fixed interface modes. These four vectors were used to

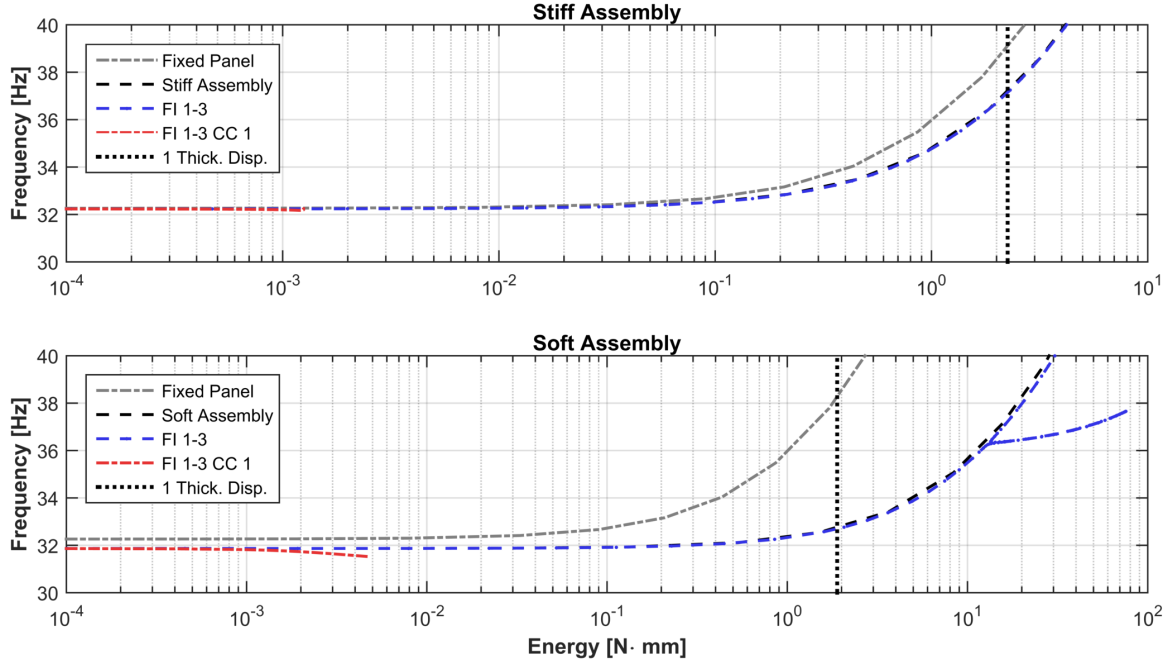


Figure 4.20: *NNMs computed from substructured NLROMs using FI and CC modes as a basis for the nonlinear forces. In both cases, including CC mode 1 led to a poor nonlinear fit and spurious/non-convergent NNM backbone.*

construct two additional NLROMs of the assembly. The impact on displacement and force error metrics is summarized in Table 4.15. The QR basis shows a clear advantage in displacement error over both of the FI/CC modesets, although the force residuals are significantly higher in both cases.

	Disp. Error [%]	Force Error [%]
FI 1-3; Stiff Assembly	1.60	0.106
FI 1-3; CC 1; Stiff Assembly	19.0	0.674
FI 1-3; Soft Assembly	13.7	2.76
FI 1-3; CC 1; Soft Assembly	79.2	4.83
QR 1-3, 6; Stiff Assembly	1.20	6.26
QR 1-3, 6; Soft Assembly	1.95	14.2

Table 4.15: *Fit properties of NLROMs constructed via the in situ substructuring technique.*

The difficulty in NLROM construction with the CC mode included can be understood much more clearly by using a MAC check on the fixed interface/characteristic constraint mode set, along with the resultant displacements from nonlinear FEA, as shown in Figure 4.21. Fixed interface modes 1 and 2 are physically very similar to CC modes 1 and 3 (leftmost plots), despite these modes being nearly orthogonal when weighted by the component's stiffness matrix (middle plots). As a result, the displacements from nonlinear FEA are extremely difficult to correctly distinguish from each other (rightmost plots).

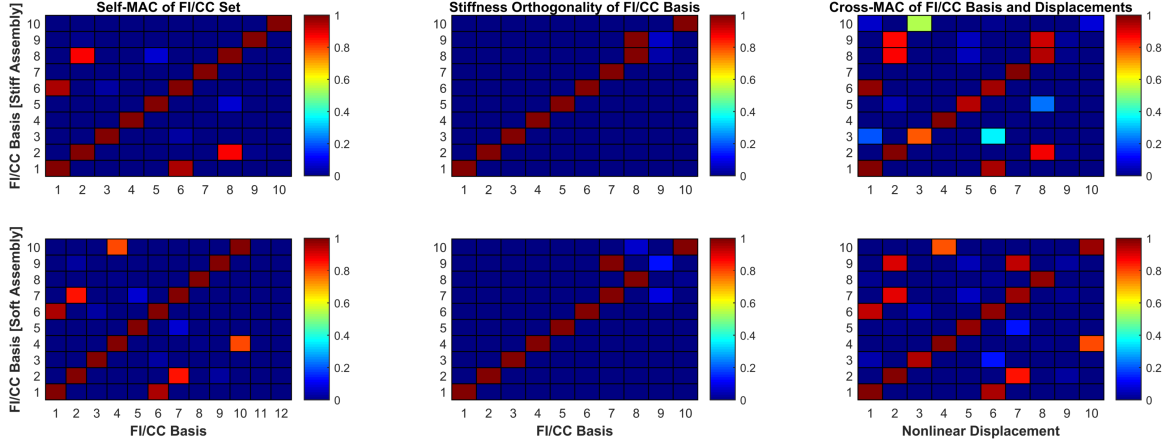


Figure 4.21: *Evaluation of the FI/CC modeset as a nonlinear force basis. Left: Self-MAC of the FI/CC modeset. Center: Inner product of the modeset, weighted by the component's stiffness matrix and normalized to the absolute maximum element in each row. Right: Cross-MAC of the FI/CC modeset and resulting displacements obtained from nonlinear FEA.*

The QR-transformed basis, however, alleviates this issue, as seen in Figure 4.22. At left is a cross-MAC comparison between the QR basis and physical FI/CC basis; vectors 6 and 8 are no longer closely associated with the first two fixed interface modes. Even though the basis is heavily coupled through the stiffness matrix, the resulting displacements are much more clearly differentiated from each other.

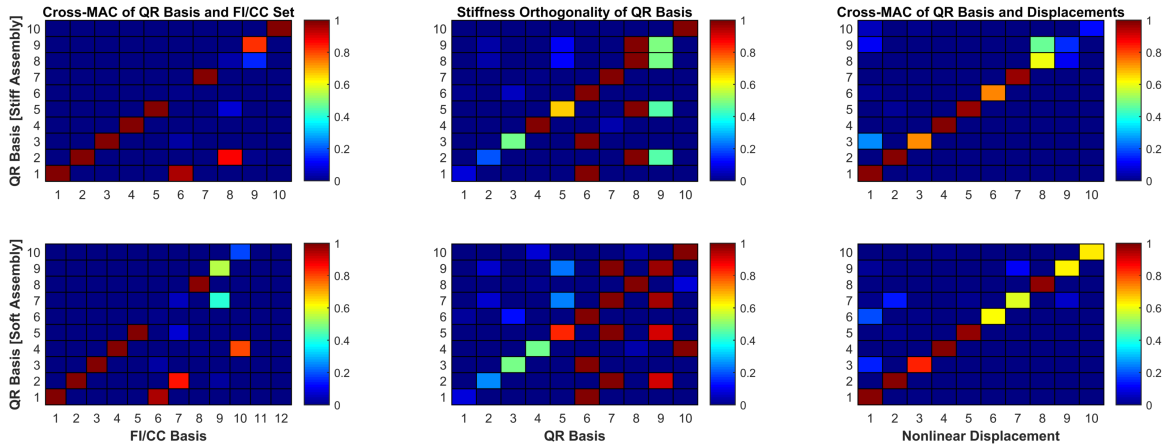


Figure 4.22: *Evaluation of the transformed QR vectors as a nonlinear force basis. Left: Cross-MAC of the FI/CC modeset and QR basis. Center: Inner product of the QR basis, weighted by the component's stiffness matrix and normalized to the absolute maximum element in each row. Right: Cross-MAC of the QR basis and resulting displacements obtained from nonlinear FEA.*

As a result of these differences, the NLROMs computed from this QR basis not only converge to suitable energy levels, but are more accurate than their counterparts computed with the fixed-interface modes only. The resulting backbones of NNM 1 from the QR basis NLROMs are shown in Figure 4.23.

The models shown here use QR modes 1, 2, 3, and 6; these correspond to FI modes 1, 2, and 3, along with the remnant of CC mode 1 which was orthogonal (unweighted) to FI mode 1. The backbone of the stiff structure was already indistinguishable from that of its corresponding assembly NLROM, but the soft assembly backbone has now shifted directly onto the truth curve. Though the difference is slight, the shift is still significant: in a more sophisticated model, omission of constraint deformations can alter the nonlinear dynamics to a much greater extent. (Recall, for instance, the consequences of omitting CC modes for the coupled plates of Section 4.1, as shown in Figure 4.9). For this assembly, only the alternate QR basis was suitable for constructing an NLROM using the implicit condensation procedure.

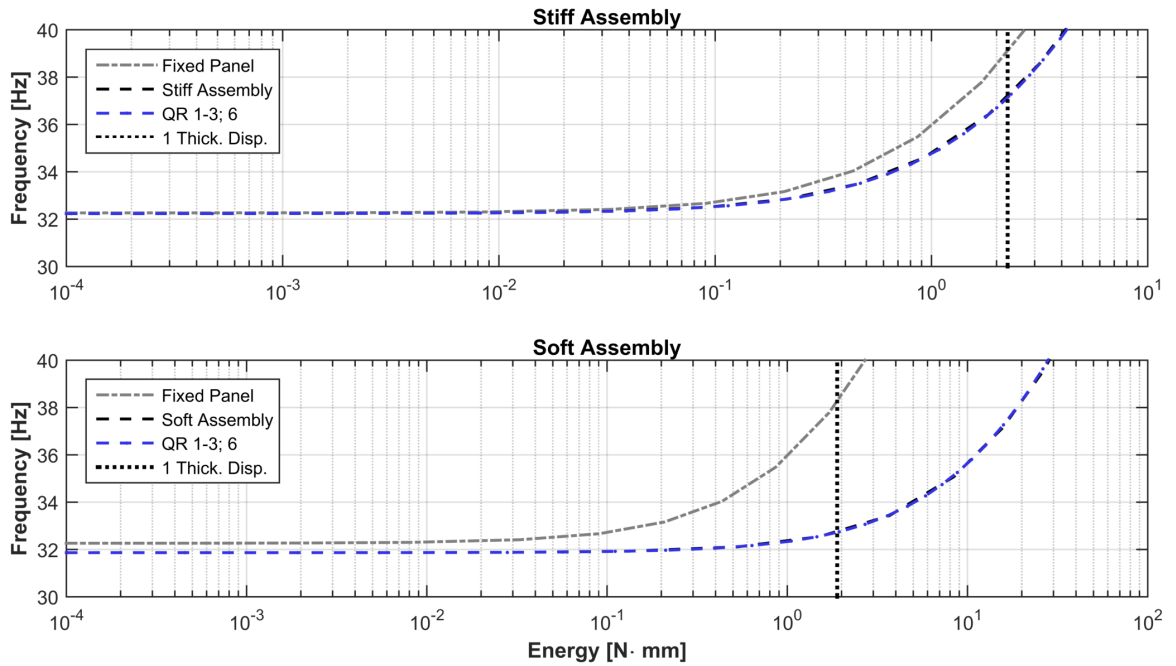


Figure 4.23: NNMs computed from substructured NLROMs using vectors from a QR factorization of the FI and CC modeset. Including QR mode 6, corresponding to the component of CC mode 1 which was orthogonal to the FI modes, led to a more accurate NNM for the soft system.

4.2.5 Discussion

The panel/stiffener model examined here demonstrated two main challenges that were not experienced with the plate substructuring problem of Section 4.1. First, the key panel component was not constrained in the unassembled state, so loads could not be arbitrarily applied to the panel without somehow modifying the boundary conditions. Attempts to model the structure's boundary conditions using linear, statically reduced stiffnesses – grounding springs at each degree of freedom – yielded inaccurate nonlinear models. However, an *in situ* technique which simply used a full-order finite element model of

the assembly to apply the implicit condensation procedure proved successful. Use of the fully-coupled boundary stiffness matrix at each component interface may yet produce accurate NLROMs, however, in order to place an upper bound on the accuracy required from a boundary representation, the *in situ* method was used instead.

A second difficulty arose in attempting to include both fixed interface and characteristic constraint modes in the NLROM force basis. The deformations spanned by the first three FI modes and first CC mode were required for an accurate NLROM, however, all models using these four basis vectors led to poor curve fits, due to the similarities between FI and CC mode 1. It is critical to note that, even though the fixed interface and characteristic constraint modes are nearly orthogonal to each other through the component stiffness matrix, the resulting deformations from a nonlinear static solution are not necessarily well-differentiated. As a result, mixing the FI and CC modes led to higher displacement residuals and poor nonlinear coefficient fits.

The alternate bases examined in Section 4.1.3 were the key to circumventing this issue. By performing a QR factorization of the FI/CC modeset of interest, a nonlinear force basis resulting in a good coefficient fit was obtained. Since it allowed inclusion of displacements associated with boundary motion, this basis provided a more accurate NLROM for the assembly on soft supports (the stiff-support version was not noticeably affected). It may be the case that, for panels mounted on stiffeners, force vectors obtained from low fixed interface and characteristic constraint modes yield similar displacements. If so, use of an alternate basis such as that obtained from a QR factorization will be critical to obtaining accurate NLROMs of these assemblies.

4.3 Two Plate and Frame Model

Finally, an assembly with multiple nonlinear components was considered. This third assembly is similar to Kuether's plate model in Section 4.1, with the addition of a supporting frame which secures each plate; the two plates are no longer directly connected to each other. The assembled structure is shown in Figure 4.24. The outer support is one inch wide with material properties identical to those given for the plates in Table 4.1, the support thickness, however, is five times that of each plate, amounting to 0.155 inches. This is intended to keep support deformations small relative to those of the plates for lower modes of the assembly. The support is meshed with 244 S4R elements for a total of 363 nodes and 2178 degrees of freedom.

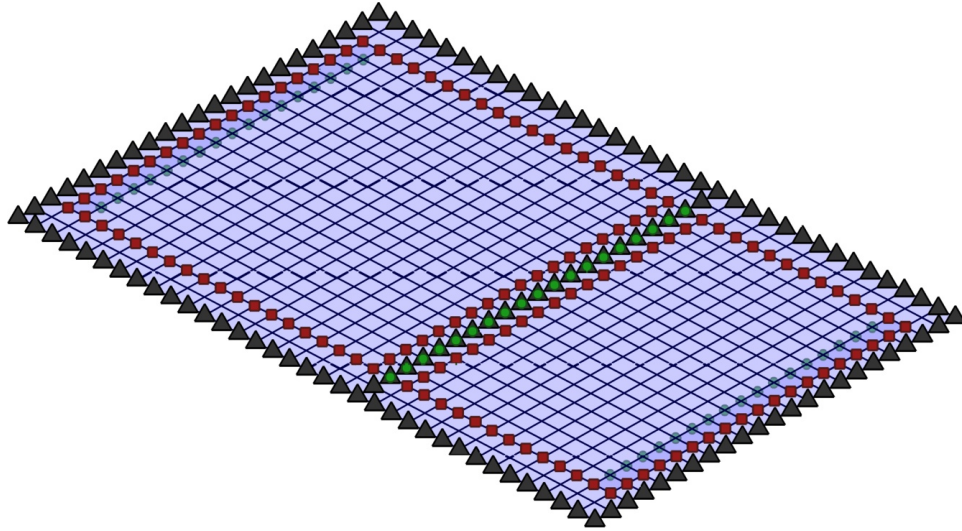


Figure 4.24: *Assembled plate/support model. Black triangles denote boundary conditions (all pinned in this case) while red squares denote coupling points (translational and rotational degrees of freedom). Green circles denote potential coupling nodes which were not used by this assembly; these uncoupled degrees of freedom are included in the internal set, not the boundary set.*

4.3.1 Linear Substructuring

Five fixed interface modes were retained for each component along with ten characteristic constraint modes, for a total of 25 degrees of freedom in the substructured assembly. Fixed interface modes of each plate may be reviewed in Tables 4.3 and 4.4; FI modes of the frame are not shown but ranged from 19.9 to 20.8 kHz. As with the previous example, several fixed interface modes of the frame were retained, despite their extremely high frequencies, in order to obtain more than a handful of system vibration modes. The first ten assembly vibration are shown in Table 4.17. Due to the stiffness of the support between the plates, the first few vibration modes are highly localized to each plate, while characteristic constraint modes are much more global in nature.

As with the other models, a modal assurance check was performed between the substructured modeshapes and modeshapes of a full-order finite element assembly. The MAC results, along with comparisons of frequency errors, are shown in Figure 4.25. Good agreement is maintained up to mode six at 395 Hz, after which the model loses accuracy. Tabulated values for the modal comparisons are given in Appendix B, Table B.6.

Table 4.16: *Retained characteristic constraint modes of the plate/support assembly.*

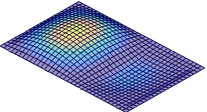
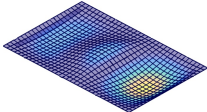
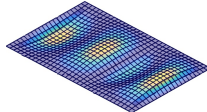
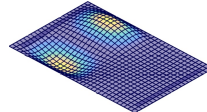
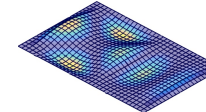
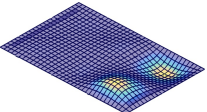
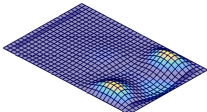
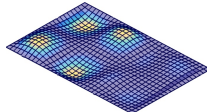
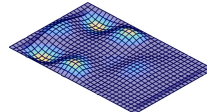
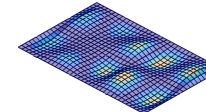
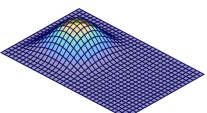
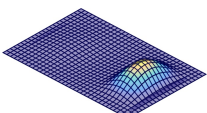
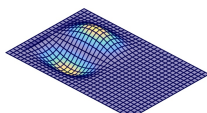
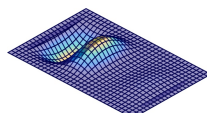
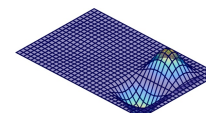
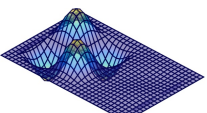
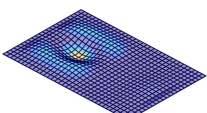
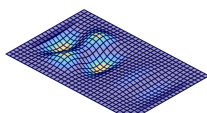
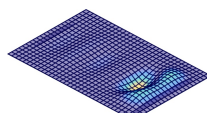
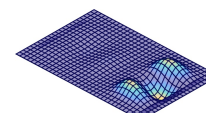
				
Mode 1: 307.4 Hz	Mode 2: 458.3 Hz	Mode 3: 517.9 Hz	Mode 4: 629.4 Hz	Mode 5: 805.7 Hz
				
Mode 6: 826.7 Hz	Mode 7: 1.12 kHz	Mode 8: 1.16 kHz	Mode 9: 1.45 kHz	Mode 10: 1.54 kHz

Table 4.17: *First ten vibration modes of the plate/support assembly.*

				
Mode 1: 125.1 Hz	Mode 2: 209.5 Hz	Mode 3: 255.0 Hz	Mode 4: 261.5 Hz	Mode 5: 336.4 Hz
				
Mode 6: 395.1 Hz	Mode 7: 437.3 Hz	Mode 8: 470.5 Hz	Mode 9: 515.6 Hz	Mode 10: 538.3 Hz

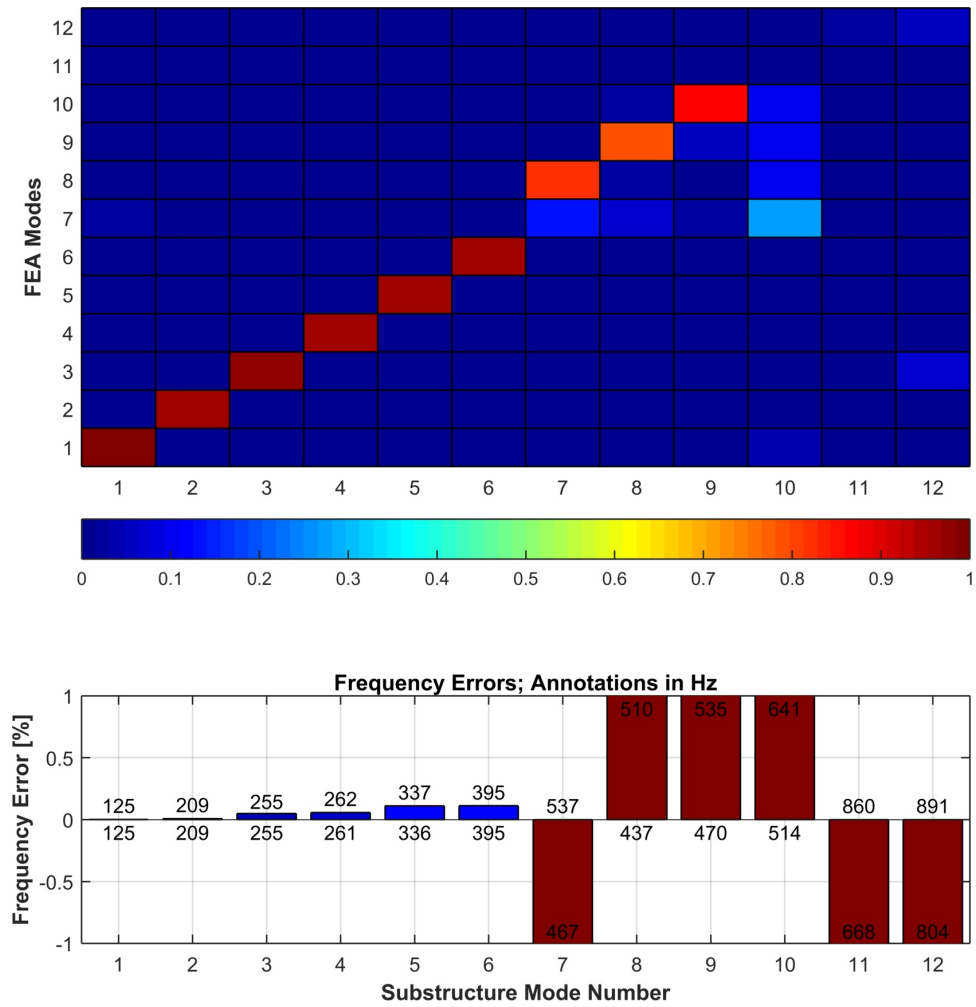


Figure 4.25: (Top): Cross-MAC between full-order FEA truth modes and substructure modes. (Bottom): Frequency errors between truth and substructure modes, based on matching MAC value; frequency values along the horizontal axis are full-order values while those adjacent to error bars are the substructured values.

4.3.2 Reference Nonlinear Model

Construction of a monolithic NLROM begins with a consideration of modes which are likely to interact spatially. From Table 4.17, the first mode of the assembly is a bending mode predominantly in the 9×9 component. Further examination of the modeshapes reveals asymmetric bending displacement in mode two (very slight) along with modes seven (a third bending mode oriented along the long axis of the assembly) and nine (a third bending mode oriented along the short assembly axis). All of these modes could be expected to contribute to a large deflection in the first NNM of the assembly, and were used as basis vectors in a series of nonlinear reduced order models constructed from a full assembly FEM. A near 3:1 frequency ratio also exists between modes one and six, but it is unlikely that these two will interact with each other based on the discrepancies between their shapes. Resulting backbones of the first NNM are plotted in Figure 4.26. Due to convergence issues with dynamic simulations of the full-order finite element model, no periodicity results are shown for these NNM backbones.

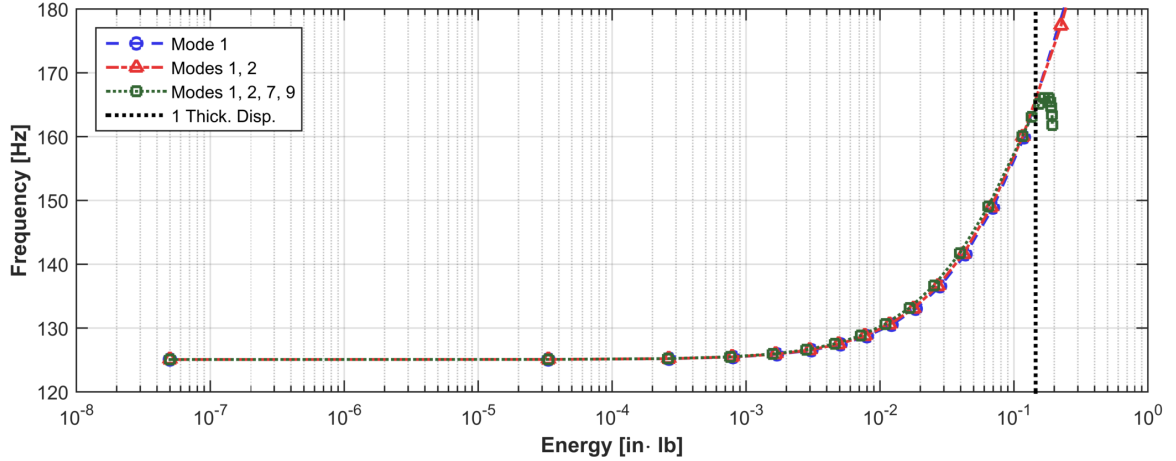


Figure 4.26: *Backbones of the first NNM for the two plate and frame assembly, computed using subsets of modes one, two, seven, and nine as nonlinear basis vectors. Dashed vertical line corresponds to a displacement of one plate thickness (0.031 inches).*

The backbones computed with modes one alone along with modes one and two agree well, but the model using a basis set of modes one, two, seven, and nine diverges non-physically just past the one-thickness energy level. This illustrates the difficulty of applying nonlinear reduced order modeling techniques to even marginally complicated structures – adding additional modes does not guarantee better accuracy, and can even result in a poor fit. Such difficulties are, of course, additional motivation for the pursuit of nonlinear substructuring techniques. Since the NNM backbone curves of all three models generally agree up to one thickness, however, further refinements to the NLROMs were not

pursued.

4.3.3 Nonlinear Substructuring

Only the two panels were treated as nonlinear components for the models below. All five fixed interface and ten characteristic constraint modes were included in the nonlinear basis of each plate; this set of fifteen modes required 4,090 load cases per component for determination of the NLROM coefficients. A total of five nonlinear models were constructed. Four were generated using a combination of:

- Either the natural FI/CC basis set or the QR transformed basis set for each component
- Either linear boundary conditions via static reduction, as per Section 4.2.3 or *in situ* boundary conditions within the full-order FEM

A fifth NLROM used fixed interface modes only on fully-fixed boundary conditions. Once each model was constructed, a backbone curve of the first nonlinear normal mode was computed. The five resulting curves are shown in Figure 4.27.

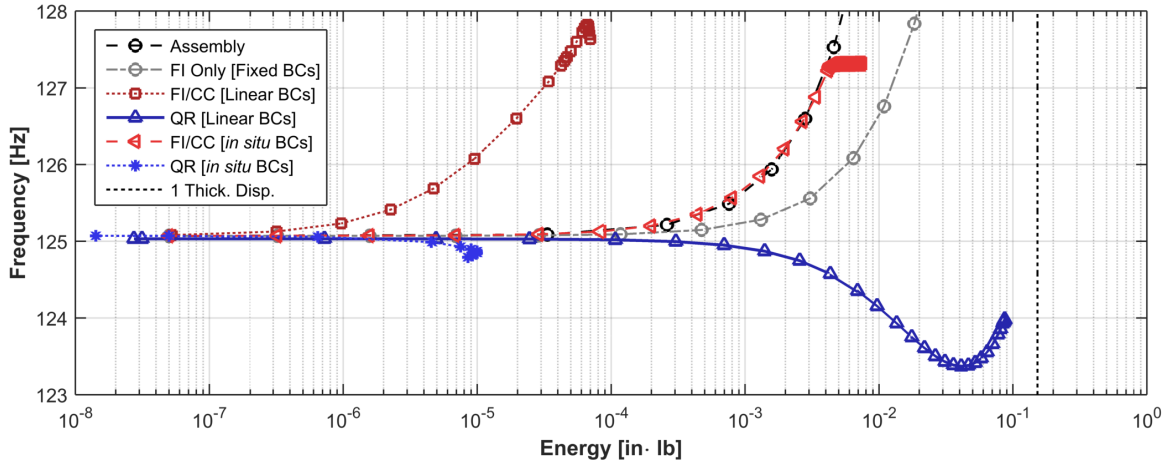


Figure 4.27: *NNMs computed from substructured NLROMs of the two plate and frame assembly. Dashed vertical line corresponds to a displacement of one plate thickness (0.031 inches).*

As with the models examined previously, the FI-only model with fixed BCs is too soft – the structure deforms significantly into the shape of the first characteristic constraint mode, and when no nonlinear stiffening is associated with this mode, the resulting NNM is too low in frequency – and the FI/CC basis model computed using linear, statically reduced boundaries is far too stiff. In a departure from

the results observed so far, neither QR vector model behaves correctly, with both showing non-physical softening behavior. In the case of the *in situ* QR model, convergence is lost almost immediately.

Despite these failures, the FI/CC *in situ* model lines up with the assembly NLROM before jumping onto an internal resonance and failing to converge. Efforts to skip this resonance and compute further up the backbone curve were not successful. Although the NLROM only manages to display a frequency shift of 2 Hz (1.6%), the ability to track the backbone curve for even a limited energy/frequency range is still taken as a qualified success.

Displacement and force error residuals for these four NLROMs are given in Table 4.18. A point of interest is that both of the QR models display relatively high displacement error levels, although there is no indication that the errors are sufficiently high to expect such spurious NNM backbones. Both FI/CC models display similar, fairly low error levels.

Basis Type	9 x 9 Plate		9 x 6 Plate	
	Disp. Error [%]	Force Error [%]	Disp. Error [%]	Force Error [%]
FI/CC [Linear BCs]	3.08	0.360	2.39	0.279
QR [Linear BCs]	14.5	1.15	30.2	1.64
FI/CC [<i>in situ</i> BCs]	2.40	0.313	3.18	0.337
QR [<i>in situ</i> BCs]	9.03	9.47	5.85	9.54

Table 4.18: *Fit properties of the two-plate and frame NLROMs using FI/CC and QR bases on both linear, statically reduced boundaries and in situ boundaries from the full-order FEM.*

4.3.4 Discussion

Introduction of a second nonlinear component on a support frame caused the *in situ* QR method to fail, but did admit a moderately accurate NLROM based on the FI/CC modes. Both of these results are in contradiction to those observed in Section 4.2. The exact causes for this failure cannot be observed directly, but potential mechanisms can be inferred.

With respect to the QR-transformed basis, a possibility for such poor performance is that some of the factored QR directions pushed the structural components into directions which exhibited softening behavior and would have eventually buckled. To obtain an orthogonal basis, the factorization process removes the bending-dominant deflections from each characteristic constraint mode, leaving components that are dominant in the plane of the plate. Attempting to obtain deflections on the order of the thickness using such deformations likely pushed the model towards a buckled state, causing a softening behavior to be captured by the nonlinear model.

As expected from the previous section, an NLROM constructed using the FI/CC modes on a linear, statically reduced set of constraint boundaries was far stiffer than expected. The *in situ* modeling procedure was once again successful, however, in generating NLROMs with accurate force coefficients. Convergence difficulties were still apparent, unfortunately. The most likely cause for such issues is “double-counting” of nonlinearity between the two components. Consider the situation when a load is applied to (for example) the 9×9 plate within the full-order finite element program: Both plates will experience a deflection, and the stiffness of the 9×6 plate will contribute to the overall resistance to the load. When the resulting deflections are brought back into MATLAB for NLROM fitting, the additional stiffness of the 9×6 plate will be implicitly included in the nonlinear restoring force, and will ultimately lead to a set of coefficients that overpredict the nonlinear stiffness of the 9×9 plate. This error will similarly affect the 9×6 plate, and in general will compound as more nonlinear components are added to the model.

It is not immediately obvious how to circumvent this difficulty. The simple removal of nearby nonlinear components from the full-order FEM is an option, but these neighboring components are essential to obtaining the correct boundary stiffness for a component. Chapter 5 considers methods which may be able to overcome the problem of implicit nonlinear coupling between components from the *in situ* modeling process.

4.4 Discussion and Future Prospects

Component mode synthesis of geometrically nonlinear components is significantly more challenging than performing the equivalent procedure with linear structural models. Techniques that are appropriate for a certain assembly may be inappropriate for another. Even the seemingly simple task of assembling structures in which the nonlinear components are constrained by underlying supports faces serious complication. To enable accurate modeling of such structural assemblies, two key concepts were explored in this chapter: Use of alternate basis functions to model the nonlinear restoring force of an NLROM, and appropriate boundary conditions for components in order to obtain accurate NLROM coefficients.

Regarding the former topic, the natural basis of fixed interface modes and characteristic constraint modes is not always ideal to correctly capture the space of a component’s nonlinear displacements and resultant restoring forces. In Section 4.1, both singular value decomposition and QR factorizations were used to arrive at alternate nonlinear force bases; both methods proved to function equally as well as

the initial set of fixed interface and characteristic constraint modes on the initial two-plate model. The QR basis did not perform well when using a reduced set of basis modes for the NLROM. The FI/CC modeset, on the other hand, was able to compute backbones accurately with just a few modes, at the cost of a reduced envelope of validity with respect to energy.

The beam and stiffener assembly of Section 4.2 admitted an accurate model *only* when using the QR-factorized basis. Due to similarities between the fixed interface and characteristic constraint modes, deformations associated with those load vectors could not be distinguished during the NLROM construction process, and NLROMs using the FI/CC basis were not valid. The plate and frame model of Section 4.3, on the other hand, yielded accurate NLROMs when using the FI/CC basis, but not from the QR basis. With such varied experiences, no definitive statements on a superior load basis can be made. Instead, it should only be noted that using alternate vector spaces to define the nonlinear restoring force of an ICE-based NLROM is a valid strategy that is worth consideration if the set of fixed interface and characteristic constraint modes causes trouble during the coefficient determination procedure.

A separate issue is application of appropriate boundary conditions to the assembly components during NLROM construction. When natural boundary conditions already exist on a component, as with the pinned plates in Section 4.1, this is not a concern. However, when the only constraints on a component are those from other parts in the assembly, then it is not immediately obvious which boundary conditions to apply during the implicit condensation procedure. The part's fixed interface modes relate to a situation with all boundary nodes constrained, but the characteristic constraint modes are not computed from such a state. Leaving the assembly free-free is not an option without using inertia relief procedures on the model, and, further, the nonlinear behavior exhibited by a structure is largely dependent upon the boundary conditions of that structure, meaning that an inertia relief procedure with no external boundary stiffness applied would not be expected to correctly capture the nonlinearity of interest. An accurate set of boundary conditions must be applied to the component prior to constructing an NLROM with the existing implicit condensation technique.

Two possible boundary formulations were examined. First, a set of linear boundary conditions was obtained by statically reducing the effective stiffness of the remainder of the substructure to each boundary degree of freedom. Each stiffness value was enforced through the application of a grounding spring within the Abaqus FEA software in use here. Unfortunately, this method was not successful, and resulted in models that were uniformly too stiff relative to the true NLROMs of the assembly.

At the upper bound of accuracy lies the full-order FEM of the assembly being examined. Assuming

such a model is available, loads can be applied to the subset of degrees of freedom which correspond to a component of interest; resulting deformations can be similarly extracted. This use of the FEM to construct NLROMs of in-place components is referred to as the *in situ* boundary condition process, and the procedure did indeed yield accurate NLROMs for the latter two examples in this chapter. As such, it is clear that the implicit condensation process is viable for constructing NLROMs for assemblies with boundary-free components.

A remaining question to be addressed is whether a more modular and procedure can be devised to take the place of the *in situ* construction process. The desire for modularity is based not only on convenience, but on accuracy of the resulting NLROMs. When multiple nonlinear components are present in close proximity to each other, loads applied to one component will induce displacements in neighboring parts; it is possible and indeed likely that these displacements will contaminate the nonlinear coefficients obtained for the component of interest. Such contamination is a possible culprit for the NNM convergence issues observed in Section 4.3, and will be of greater concern for assemblies with larger numbers of nonlinear components.

A word on computational efficiency is also in order. While it is by no means desirable to resort to a full-order finite element model in order to obtain a component NLROM, it is not a disqualifying requirement. The key benefit of a substructuring approach in specifying NLROMs is the reduction in load cases required to construct a model. Due to the cubic order of growth of these load cases, complicated, built-up geometries which require tens of modes to model quickly become prohibitive. Figure 4.28 illustrates this principle.

Consider a model which requires 30 modes in the nonlinear basis. A total of 34,280 load cases are required to specify this NLROM. Were the model split into nine nonlinear components of interest, a slightly reduced number of load cases (29,736) would be necessary if each component required 14 modes. Should each component's nonlinear basis be reduced to 10 modes, 10,440 load cases would be needed; at 5 modes, the count drops to 1,160. Even if each of these load cases were run on the full-order finite element model, a dramatic savings in construction time would be achieved.

The work here has pushed forward the boundaries of geometrically nonlinear substructuring techniques by extending implicit condensation-based models from assemblies featuring fully constrained subcomponents to those with components free of natural boundary conditions, such as panel and stiffener assemblies. These types of structures are ubiquitous in the aerospace applications of interest. To bring the substructuring techniques discussed in here to maturity, further work is necessary to efficiently

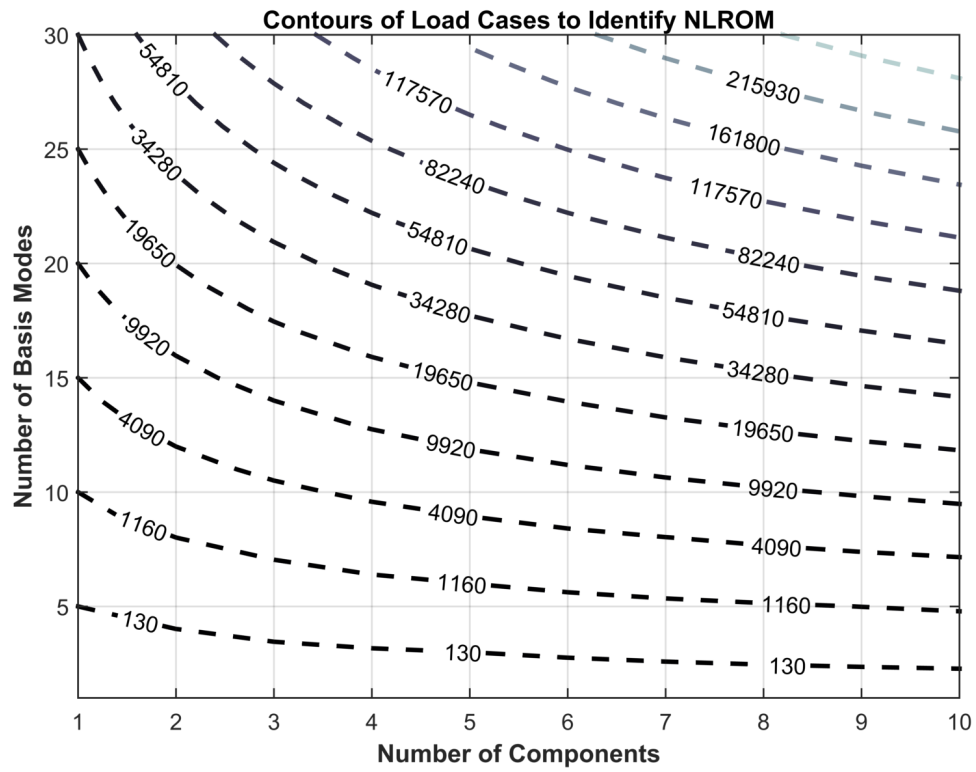


Figure 4.28: Contours of required load cases to specify an ICE NLROM as a function of component count and number of basis modes per component. Contours correspond to single-component models at multiples of five basis modes.

and accurately model component boundary conditions, decouple nonlinear restoring force contributions between different components, and automate or improve the basis selection process for each nonlinear component in the model.

Chapter 5

Future Prospects

Since their introduction, nonlinear reduced order models based on non-intrusive finite element techniques have moved from modeling simple components to complex assemblies with a high degree of accuracy. To expand their application to industrial scale vehicle models, however, substructuring techniques of some sort will almost surely be necessary. This work has broadened the envelope of systems which may be modeled using nonlinear component mode synthesis techniques, specifically, by considering panel/stiffener type assemblies. Despite these gains, further study is necessary before nonlinear substructuring can be performed as reliably and automatically as the linear counterpart. Three key areas for examination include the use of an enforced displacement method to generate component reduced order models, consideration of alternate substructuring methods to form the nonlinear basis of each component, and determination of an efficient method to represent each component's boundary stiffness with sufficient accuracy.

Enforced Displacement Technique

All of the reduced order models constructed in this work used the implicit condensation method for coefficient specification rather than the enforced displacement procedure, as explained in Section 2.2. As a result of this choice, the unconstrained panel components studied in Chapter 4 proved troublesome to model, since the static finite element routines used to perform coefficient specification could not be used to solve for the displacements of an unconstrained model. It is immediately obvious that the enforced displacement procedure suffers from no such limitation, and would be an excellent candidate

for construction of component NLROMs.

The situation is complicated, however, by the requirement for “dual mode” basis vectors within the enforced displacement mode set. These dual modes, corresponding to membrane-dominant displacements of the structure, are usually obtained by applying *static loads* to the finite element model of interest, which brings the question of boundary conditions back to the fore: Not only must boundary conditions be specified on the applied load model, but it seems natural that dual modes obtained using a model with an inaccurate boundary representation will lead to poor NLROMs.

This caveat hardly disqualifies the enforced displacement technique, but rather serves as a reminder that one cannot escape the question of boundary representation when trying to model geometrically nonlinear subcomponents. With this in mind, the following enforced displacement CMS procedure is proposed for future study:

- After obtaining a basis of FI and CC modes or some transformation thereof, obtain each component’s desired set of dual modes from an *in situ* procedure using the full assembly finite element model, as performed here.
- Apply the enforced displacement method to each component finite element model with no modifications made to the natural boundary conditions.

The kinematics of the dual modes obtained using an accurate boundary representation should be of sufficient accuracy to obtain nonlinear stiffness coefficients which match those of the assembled component. Assuming it functions correctly, this procedure has three key advantages over that presented here. First, the assembly finite element model would be required only for a small set of static load cases, after which the smaller, component-level finite element models would be used exclusively. Second, the use of isolated FE models for coefficient determination would eliminate any unwanted coupling between the nonlinear stiffness of adjacent components which results from the implicit condensation *in situ* procedure. Finally, the reduction in required load cases for the enforced displacement method relative to ICE will reduce the computational cost of the procedure to a greater extent, assuming a small enough set of dual modes can be used with each component.

Alternate Substructuring Methodologies

Aside from alternate strategies for obtaining nonlinear force coefficients, alternate strategies for obtaining component basis vectors are also available. For example, the dual Craig-Bampton with free interface modes and reduced residual flexibility modes [44] is analogous to the fixed interface and characteristic constraint mode formulation used here; the use of free interface modes and their nonzero displacements at the boundaries may prove advantageous in modeling nonlinear assemblies with relatively flexible supporting structures.

Further investigation into various types of interface reduction is also in order. “Local” characteristic constraint modes, which perform interface reduction at the component level rather than at the system level, are a topic of current research interest; see, for example, the method proposed by Hong et. al [38]. Local interface reductions may require fewer modes per component to obtain accurate linear models than their system level counterparts, meaning that fewer characteristic constraint modes would need to be considered for inclusion in the nonlinear basis. Consider, for example, the structure in Section 4.3, which used five fixed interface modes per component and ten system level constraint modes. If the same deformations could be represented using, perhaps, five local constraint modes per component, then the total count of modal coordinates in the assembly would climb from 25 to 30, but only 10 (at most) modal coordinates could be included in each NLROM, down from 15. For larger structures, which might require tens or hundreds of characteristic constraint modes (i.e. the multi-bay panel of Section 3.4 and its 35 characteristic modes), the use of local CC modes might be a necessity to obtain feasible static load case counts for component NLROMs.

Finally, the application of so-called “Robin-like” boundary conditions may be relevant to the problem at hand. Robin boundary conditions are a linear combination of the Dirichlet (zero displacement) boundary conditions represented by the fixed-interface modes of the traditional Craig-Bampton method and the Neumann (zero stiffness) boundary conditions represented by free-interface modes of the Dual Craig-Bampton method – in essence, a set of springs located along the structure’s boundaries. Gruber, Rutzmoser, and Rixen propose in [45] a generalized Craig-Bampton method to use such a formulation without specifying a static reduction for use on component boundaries; the static interface reduction process described in Section 4.2.3 is an excellent candidate for this purpose. Given the intimate connection between NLROMs and component boundaries, it seems natural that a linear substructuring technique designed to recognize the surrounding boundary stiffness would be advantageous for nonlinear component mode synthesis.

Accurate Boundary Representations

It is somewhat surprising that the linear boundary approximation attempted in Sections 4.2 and 4.3 was not sufficiently accurate to generate component NLROMs; further, it is unclear whether the discrepancy arises due to the secondary static reduction to each individual degree of freedom, or due to the assumption of linearity itself. An evaluation of the former approximation, performed by coupling the full boundary stiffness matrices to the nonlinear component boundaries, should be conducted as soon as practical.

In the event that fully coupled boundary stiffness matrices still do not produce valid NLROMs, alternatives to the full-order *in situ* process may exist. Since an NLROM of each component can be used to obtain a good approximation of that component's static stiffness, one can imagine a process in which nonlinear component models are built in a "ground up" fashion: NLROMs of any fully constrained support structure can be built initially, then their nonlinear boundary stiffnesses statically reduced to obtain polynomial expressions for use as the boundary conditions of any attached components. These components, in turn, can then be targeted for NLROM construction until the entire assembly has is represented with nonlinear models. This approach is theoretically possible, but presents several obvious hurdles: Aside from the difficulty of statically reducing polynomial expressions (which could be performed with symbolic mathematical software), the specification of arbitrary nonlinear stiffness functions is not straightforward for most commercial FEA codes (such as Abaqus), and in the general case requires the use of user defined spring elements.

Alternatively, it may also be possible to model *in situ* only a subset of the full-order finite element model, namely, the structure only immediately surrounding the component of interest. An appropriate simulation radius could be based either on component connectivity or a simple distance metric and could reduce the overall computational cost for NLROMs based on very large assemblies.

The topics listed above are only a small set of the research challenges and opportunities involving geometrically nonlinear substructuring. This thesis demonstrated that the selection of each component's basis set is of critical importance in obtaining an accurate NLROM, and that an accurate representation of the component boundary stiffness is a requirement for validity as well. Despite the difficulty of performing component mode synthesis on nonlinear components, the methods are viable and the payoffs in computational efficiency can be immense.

Appendices

Appendix A

Characteristic Constraint Mode Example

This appendix overviews the workflow required to use the MATLAB toolset written for this thesis. The description is supplemented by portions of MATLAB code which were used to create the multi-bay panel example of Section 3.4. To actually create this model, the reader must possess, in addition to relevant MATLAB class files, the component Abaqus input files and the Python interface used to read Abaqus output databases. Prior to describing the MATLAB portion of the workflow, a note on the creation of Abaqus input files for use with the toolset is in order.

Abaqus Input Files

Abaqus input files may be created manually or generated from the Abaqus CAE application. For complicated models, the latter is preferred. The substructuring module requires separate Abaqus models of each component, and certain routines (e.g. the *in situ* nonlinear substructuring method) also require a model of the full assembly. These models are used to generate the ABINT components as described below. The user should ensure that each model has a fully defined mesh and correctly specified material/section properties. A simple free-free modal step is a straightforward way to ensure that a model is behaving as expected.

ABINT requires that an Abaqus/Standard analysis step be associated with each model – any structural analysis type will suffice, although a modal step is usually the easiest to request. Once the model

and an analysis step are requested, the input file may be written from Abaqus/CAE and placed into a convenient location for use with the ABINT module via MATLAB.

ABINT/CBICE Component Creation

The workflow proceeds in a roughly ground-up manner, with each module used in the order it was presented in Section 3.3. First, the ABINT and CBICE modules are used to read an Abaqus input deck and create a component which can be supplied to the CCSS substructuring class.

The snippet below creates an ABINT object. Relative directory paths are defined and passed to the ABINT constructor. The path *workingDir* corresponds to the directory used for Abaqus scratch files, *filepathAbint* directs the object to a save location when the *save* method is later called, and *pythonpath* directs the object to the location of the Abaqus Python interface file.

```
workingDir = 'C:\Temp';
filepathAbint = 'ABINTs';
filepathCbice = 'CBROMs';
pythonpath = '..\python';

% Make ABINT object and save for later
ab = ABINT(workingDir, filepathAbint, pythonpath);
% Read an input file
inputPath = '..\SchonemanMBPAbaqus\Abaqus Storage\models\S_stiffener';
inputFile = 'S_Stiffener_SS';
ab = ab.readInp(inputPath, inputFile);
ab = ab.getDof();
[M, K] = ab.matrix([]);
save(ab);
```

The key function call is *readInp* which specifies an input file and path to be read. Optional calls below are *getDof*, which obtains the degree of freedom vector of the part for later use, and *matrix*, which obtains the mass and stiffness matrices that are used shortly. The use of an empty array (brackets) in the call to *matrix* indicates that no boundary conditions are specified, so that the free-free stiffness matrix is obtained.

Now, a CBICE object is created using the ABINT object created above. The *mind*, *thick*, and *linDispLC* arguments are deprecated and remain only for backwards compatibility; *filepathCbice* gives the object a filepath on which to save itself when *save* is called. Note that, after creation, the mass and stiffness matrices are stored in the *linMode* structure of CBICE, this action will be explained below.

```
% Make CBICE object and save
linDispLC = 1; mind = 1; thick = 1;
cbi = CBICE(ab, mind, thick, linDispLC, workingDir, filepathCbice);
cbi.linModel.M = M; cbi.linModel.K = K;
```

```
save(cbi);
```

This process must be repeated for all distinct components in the model.

CCSS Object Creation and Substructuring

Afterwards, the CCSS object can be created and substructuring can be performed. Creating an empty CCSS object requires only a path for the object to save to (*filepathCCSS*) along with a name for the saved file (*filename*).

```
filepathCbss = 'CBSSs';
filename = 'mbpanel_CC';
ccs = CCSS(filepathCbss, filename);
```

Once the CCSS object is created, CBICE components must be added. Assume that the variables *S_stiffener*, *hat_stiffener*, and *panel* used below correspond to CBICE models of the appropriate component. Locating the component is achieved using *refNode* and *location*; these specify a reference node on the model and the location in space where that node should be placed (no rotational capability exists for components). Two $n \times 7$ arrays must be created to define *boundary*, the set of fixed boundary degrees of freedom, and *conn*, the set of potential attachment DOF; *n* is the number of *nodes* in each set. The first column is the Abaqus node number of the applicable node, while columns two through seven correspond to the three displacement and three rotational degrees of freedom. Nonzero entries correspond to DOF which are fixed (for *boundary*) or available for coupling (for *conn*). Finally, *nModes* specifies the number of fixed interface modes should be retained in the component.

Once these values are specified, the snippet below uses a loop to place four copies of the component into CCSS, each offset by a different amount.

```
% Reference node, base location, and offset for SS stiffeners
refNod = 13882;
location = [0, 0, 0];
offset = [18.75, 0, 0];

% Boundary and connsector sets for SS stiffeners
nBC = size(S_stiffener.abint.nodeSets.BCDOF, 1);
boundary = [S_stiffener.abint.nodeSets.BCDOF, ones(nBC, 6)]; % All fixed
nBC = size(S_stiffener.abint.nodeSets.RETAINEDDOFS, 1);
conn = [S_stiffener.abint.nodeSets.RETAINEDDOFS, ones(nBC, 6)]; % All fixed

% Number of FI modes to retain
nModes = 5;

% Add S stiffeners
for i = 0:3
    ccs = ccs.addPart(S_stiffener, refNode, location + i*offset, boundary, conn, nModes);
end
```

Placing the hat stiffener components is identical, except that an alternate syntax is used to specify the FI mode count: When a vector of length 2 is passed instead of a scalar, it serves as a frequency

range for the retained fixed interface modes. Note also that the *boundaryHat* variable is empty as the hat stiffeners have no natural boundary conditions.

```
% Reference node, bas location, and offset for hat stiffeners
refNodeHat = 6050;
locationHat = [-196.9E-03,750.E-03,1.280102];
offsetHat = [0, 0, 7.5];

% Boundary and connector sets for hat stiffeners
boundaryHat = [];
nBC = size(hat_stiffener.abint.nodeSets.RETAINEDDOFS, 1);
connHat = [hat_stiffener.abint.nodeSets.RETAINEDDOFS, ones(nBC, 6)];

% Frequency range of FI modes to retain
freqRange = [0, 750];

% Add hat stiffeners
for i = 0:3
    ccs = ccs.addPart(hat_stiffener, refNodeHat, locationHat + i*offsetHat, ...
                     boundaryHat, connHat, freqRange);
end
```

Placement of the nine panels occurs similarly.

```
% Add all 9 panels
refNode = 3929;
nBC = size(panel.abint.nodeSets.RETAINEDDOFS, 1);
connectors = [panel.abint.nodeSets.RETAINEDDOFS, ones(nBC, 6)]; % Fully clamped
location = [57.537399, 750.E-03, 23.780012];
xOffset = [18.75, 0, 0]; zOffset = [0, 0, 7.5];
boundary = [];

% Number of FI modes to retain
nModes = 5;

% Add 9 panels
for i = 0:2 % x offset
    for j = 0:2 % y offset
        loc = location - i*xOffset - j*zOffset;
        ccs = ccs.addPart(panel, refNode, loc, boundary, connectors, 5);
    end
end
```

Once all components are included, the connection array must be built using *makeConnections*, which compares the location of each eligible attachment node and determines which degrees of freedom should be connected. Then, Craig-Bampton models of each component are built using *buildCBModels*. The optional 'matlab' argument tells CCSS to use the stored mass and stiffness matrices within CBICE to perform the requisite modal analysis – if they are available. Since these were stored earlier when the CBICE objects were created, this is an available option; performing modal analysis within MATLAB is

usually much quicker than sending out an analysis request to Abaqus and waiting for the results. If the mass and stiffness matrices are not stored, Abaqus is used to obtain the component modes; after the first call to *buildCBModels*, the system matrices of each component will be stored and available.

Once the connections are made, it is helpful to call *plot* and examine the location, boundary conditions, and connections of each component.

```
% Build the connection array
ccs = ccs.makeConnections();

% Build the CB model of each part
ccs = ccs.buildCBModels('matlab');
ccs.plot();
```

Finally, modal analysis of the system is performed using *buildCBSystem*, which assembles the system and performs a modal analysis to obtain the requested number of modes. Once complete, a full-order Abaqus output database can be loaded for verification using *loadOdb*. The database read process can be quite long for large models. Upon loading, *makeMac* compares each mode of the structure on a node-by-node basis using physical location to determine which degrees of freedom should be compared; the function reports the number of matched and non-matched nodes. (All reported results in this thesis had properly matched nodes.) After the MAC is computed, both comparison plots and tables can be generated.

```
% Perform system modal analysis
nModes = 50;
ccs = ccs.buildCBSystem(nModes);

% Load full-order results for comparison
odbpath = 'C:\Temp';
odbfile = 'mbpanel';
pythonpath = '../python';
ccs = ccs.loadOdb(odbpath, odbfile, pythonpath)

% Make MAC comparison, plot results, and output table
ccs = ccs.makeMac();
errorMax = 2.5; nModes = 35;
ccs.comparePlot(errorMax, nModes);
nModes = 20;
ccs.compareTable(nModes);
```

This completes the overview of linear modeling with the MATLAB toolset used for this work. Nonlinear modeling is not covered, as there are only a handful of methods that need be considered, but their use requires in-depth familiarity with the toolset. Once a user becomes proficient with constructing linear substructures using CCSS and the associated methods, they can use the available documentation and examples to familiarize with the nonlinear methods.

Appendix B

Numerical Substructuring Verification Metrics

The tables below give numerical metrics for the substructures considered in this work to supplement the figures shown in the body of the text. The column labels for each table below are interpreted as follows:

- **Mode:** Substructure mode number
- **Match Mode:** FEA mode with the highest MAC value relative to the substructure mode, not necessarily located along the MAC diagonal
- **SS Freq:** Frequency of the substructure mode
- **Ab Freq:** Frequency of the FEA mode
- **Error [%]:** Percentage error of the substructure frequency relative to the FEA frequency
- **MAC:** Highest MAC value of the FEA modes relative to the substructure mode, ideally 1.00
- **Off-Mode MAC:** Second-highest MAC value of the FEA modes relative to the substructure mode, ideally 0.00

Section 3.4 – Multi Bay Panel; CB Model

Mode	Match Mode	SS Freq	Ab Freq	Error [%]	MAC	Off-Mode MAC
1	1	114.33	114.98	-0.57	0.99	0.022
2	2	120.79	121.31	-0.43	0.99	0.011
3	3	125.19	125.77	-0.46	0.99	0.026
4	4	130.91	131.67	-0.58	0.97	0.023
5	5	131.93	132.19	-0.19	0.97	0.027
6	6	142.07	142.84	-0.54	0.98	0.005
7	8	143.49	144.91	-0.98	0.94	0.107
8	7	142.44	143.29	-0.59	0.94	0.046
9	9	151.29	153.16	-1.22	0.99	0.006
10	10	192.03	192.35	-0.17	1.00	0.001
11	11	195.40	195.71	-0.16	1.00	0.001
12	12	201.29	201.53	-0.12	1.00	0.001
13	13	203.44	203.73	-0.14	0.99	0.001
14	14	205.75	206.14	-0.19	0.99	0.001
15	15	210.51	210.89	-0.18	0.99	0.002
16	17	218.76	219.24	-0.22	0.96	0.037
17	16	218.28	218.68	-0.18	0.95	0.042
18	18	220.61	221.05	-0.20	0.99	0.006
19	19	247.61	244.83	1.13	0.87	0.112
20	20	251.79	248.23	1.44	0.87	0.103

Table B.1: *Tabulated comparison between full-order modal analysis and Craig-Bampton CMS modal analysis of the multi-bay panel.*

Section 3.4 – Multi Bay Panel; CC Model

Mode	Match Mode	SS Freq	Ab Freq	Error [%]	MAC	Off-Mode MAC
1	1	114.33	114.98	-0.57	0.99	0.020
2	2	120.79	121.31	-0.43	0.99	0.014
3	3	125.19	125.77	-0.46	0.99	0.025
4	4	130.91	131.67	-0.58	0.97	0.023
5	5	131.93	132.19	-0.19	0.97	0.027
6	6	142.08	142.84	-0.53	0.98	0.005
7	7	142.45	143.29	-0.58	0.94	0.112
8	8	143.51	144.91	-0.97	0.94	0.080
9	9	151.31	153.16	-1.21	0.99	0.009
10	10	192.19	192.35	-0.09	0.99	0.001
11	11	195.63	195.71	-0.04	0.99	0.001
12	12	201.45	201.53	-0.04	1.00	0.001
13	13	203.74	203.73	0.00	0.99	0.001
14	14	206.18	206.14	0.02	0.99	0.001
15	15	211.38	210.89	0.23	0.99	0.002
16	16	219.93	218.68	0.57	0.98	0.005
17	17	220.38	219.24	0.52	0.98	0.002
18	18	222.87	221.05	0.82	0.98	0.007
19	19	247.67	244.83	1.16	0.87	0.111
20	20	251.89	248.23	1.47	0.87	0.102

Table B.2: *Tabulated comparison between full-order modal analysis and characteristic constraint CMS modal analysis of the multi-bay panel.*

Section 4.1 – Pinned Plate Assembly

Mode	Match Mode	SS Freq	Ab Freq	Error [%]	MAC	Off-Mode MAC
1	1	78.38	78.38	-0.00	1.00	0.000
2	2	135.08	135.07	0.01	1.00	0.002
3	3	185.65	185.65	0.00	1.00	0.001
4	4	202.98	202.96	0.01	1.00	0.003
5	5	239.50	239.47	0.01	1.00	0.001
6	6	306.41	306.35	0.02	1.00	0.001
7	7	366.28	365.69	0.16	1.00	0.000
8	8	368.26	368.24	0.01	1.00	0.000
9	9	419.79	419.71	0.02	1.00	0.000
10	10	434.20	434.13	0.02	1.00	0.003
11	11	476.25	474.42	0.39	0.99	0.001
12	12	485.64	485.53	0.02	1.00	0.001
13	13	533.83	533.66	0.03	1.00	0.001
14	14	627.79	627.67	0.02	1.00	0.001
15	16	659.39	657.05	0.36	0.97	0.001
16	15	662.11	656.67	0.83	0.99	0.000
17	17	677.99	677.49	0.07	1.00	0.000
18	18	706.57	706.39	0.03	1.00	0.000
19	19	743.12	742.43	0.09	1.00	0.000
20	20	1361.10	762.33	78.54	0.39	0.007

Table B.3: *Tabulated comparison between full-order modal analysis and characteristic constraint CMS modal analysis of the pinned plate assembly.*

Section 4.2 – Panel/Stiffener Assembly [soft]

Mode	Match Mode	SS Freq	Ab Freq	Error [%]	MAC	Off-Mode MAC
1	1	31.87	31.87	-0.00	1.00	0.000
2	2	88.52	88.52	0.00	1.00	0.000
3	3	176.04	176.00	0.02	1.00	0.000
4	4	197.15	197.15	0.00	1.00	0.000
5	5	296.01	295.95	0.02	1.00	0.000
6	9	947.42	648.54	46.09	0.59	0.020
7	8	1033.53	609.13	69.67	0.67	0.000
8	12	2403.78	892.47	169.34	0.47	0.002
9	11	2584.16	833.41	210.07	0.59	0.015
10	6	3100.57	398.71	677.65	0.98	0.001

Table B.4: *Tabulated comparison between full-order modal analysis and characteristic constraint CMS modal analysis of the soft panel/stiffener assembly.*

Section 4.2 – Panel/Stiffener Assembly [stiff]

Mode	Match Mode	SS Freq	Ab Freq	Error [%]	MAC	Off-Mode MAC
1	1	32.23	32.23	-0.00	1.00	0.000
2	2	89.61	89.61	-0.00	1.00	0.000
3	3	178.04	178.04	-0.00	1.00	0.000
4	4	198.59	198.47	0.06	1.00	0.000
5	5	299.74	299.74	0.00	1.00	0.001
6	8	1583.35	613.60	158.04	0.00	0.000
7	9	3843.29	657.98	484.10	0.64	0.001
8	6	4461.41	401.45	1011.32	0.00	0.000
9	10	8689.48	839.85	934.65	0.58	0.002
10	8	11630.92	613.60	1795.52	0.00	0.000

Table B.5: *Tabulated comparison between full-order modal analysis and characteristic constraint CMS modal analysis of the stiff panel/stiffener assembly.*

Section 4.3 – Plate/Frame Assembly [soft]

Mode	Match Mode	SS Freq	Ab Freq	Error [%]	MAC	Off-Mode MAC
1	1	125.07	125.07	0.00	0.99	0.026
2	2	209.50	209.48	0.01	0.97	0.031
3	3	255.02	254.89	0.05	0.99	0.066
4	4	261.54	261.39	0.06	0.97	0.023
5	5	336.63	336.25	0.11	0.97	0.076
6	6	395.23	394.79	0.11	0.97	0.068
7	10	466.55	537.20	-13.15	0.27	0.126
8	7	509.79	436.53	16.78	0.83	0.096
9	8	534.78	470.17	13.74	0.79	0.088
10	9	641.25	513.71	24.83	0.88	0.101
11	19	667.79	859.77	-22.33	0.18	0.030
12	20	804.12	890.88	-9.74	0.06	0.050
13	11	885.84	604.67	46.50	0.79	0.113
14	12	977.12	609.46	60.33	0.51	0.120
15	13	1146.30	664.34	72.55	0.17	0.115

Table B.6: *Tabulated comparison between full-order modal analysis and characteristic constraint CMS modal analysis of the plate/frame assembly.*

Bibliography

- [1] R. W. Gordon and J. J. Hollkamp, “Reduced-order models for acoustic response prediction,” Tech. Rep. AFRL-RBWP-TR-2011-3040, Air Force Research Laboratory, 2011.
- [2] N. Teunisse, P. Tiso, L. Demasi, and R. Cavallaro, “Computational reduced order methods for structurally nonlinear joined wings,” in *56th AIAA/ASCE/AHS/ASC Structures, Structural Dynamics, and Materials Conference*, (Kissimmee, Florida), January 2015.
- [3] J. Wang, C. Tzikang, D. W. Sleight, and A. Tessler, “Simulating nonlinear deformations of solar sail membranes using explicit time integration,” in *45th AIAA/ASCE/AHS/ASC Structures, Structural Dynamics, and Materials Conference*, (Palm Springs, California), March 2004.
- [4] E. J. Tuegel, A. R. Ingraffea, T. G. Eason, and M. S. Spottswood, “Reengineering aircraft structural life prediction using a digital twin,” *International Journal of Aerospace Engineering*, vol. 2011, 2011.
- [5] M. Nash, *Nonlinear Structural Dynamics by Finite Element Modal Synthesis*. PhD thesis, Department of Aeronautics, Imperial College, 1977.
- [6] D. J. Segalman and C. R. Dohrmann, “Method for calculating the dynamics of rotating flexible structures, part 1: Derivation,” *Journal of Vibration and Acoustics, Transactions of the ASME*, vol. 118, pp. 313–317, 1996.
- [7] D. J. Segalman and C. R. Dohrmann, “Method for calculating the dynamics of rotating flexible structures, part 2: Example calculations,” *Journal of Vibration and Acoustics, Transactions of the ASME*, vol. 118, pp. 318–322, 1996.
- [8] M. I. McEwan, J. Wright, J. E. Cooper, and A. Y. T. Leung, “A combined modal/finite element analysis technique for the dynamic response of a non-linear beam to harmonic excitation,” *Journal of Sound and Vibration*, vol. 243, pp. 601–624, 2001.
- [9] A. A. Muravyov and S. A. Rizzi, “Determination of nonlinear stiffness with application to random vibration of geometrically nonlinear structures,” *Computers and Structures*, vol. 81, pp. 1513–1523, 2003.
- [10] M. P. Mignolet, A. Przekop, S. A. Rizzi, and S. M. Spottswood, “A review of indirect/non-intrusive reduced order modeling of nonlinear geometric structures,” *Journal of Sound and Vibration*, vol. 332, pp. 2437–2460, 2013.
- [11] J. J. Hollkamp, R. W. Gordon, and S. M. Spottswood, “Nonlinear modal models for sonic fatigue response prediction: a comparison of methods,” *Journal of Sound and Vibration*, vol. 284, pp. 1145–1163, 2005.
- [12] M. C. Bampton and R. R. CRAIG, JR, “Coupling of substructures for dynamic analyses,” *AIAA Journal*, vol. 6, no. 7, pp. 1313–1319, 1968.

- [13] R. J. Kuether and M. S. Allen, "Substructuring with nonlinear reduced order models and interface reduction with characteristic constraint modes," in *55th AIAA/ASME/ASCE/AHS/ASC Structures, Structural Dynamics, and Materials Conference*, 2014.
- [14] R. J. Kuether, M. R. Brake, and M. S. Allen, "Evaluating convergence of reduced order models using nonlinear normal modes," *Model Validation and Uncertainty Quantification*, vol. 3, pp. 287–300, 2014.
- [15] R. J. Kuether, M. S. Allen, and J. J. Hollkamp, "Modal substructuring of geometrically nonlinear finite-element models," *AIAA Journal*, vol. 54, no. 2, pp. 691–702, 2015.
- [16] C. Touzé, O. Thomas, and A. Chaigne, "Asymmetric non-linear forced vibrations of free-edge circular plates. part 1: Theory," *Journal of Sound and Vibration*, vol. 258, no. 4, pp. 649–676, 2002.
- [17] M. F. Barone, I. Kalashnikova, M. R. Brake, and D. J. Segalman, "Reduced order modeling of fluid/structure interaction," *Sandia National Laboratories Report, SAND No.*, vol. 7189, 2009.
- [18] M. Amabili, A. Sarkar, and M. Paidoussis, "Reduced-order models for nonlinear vibrations of cylindrical shells via the proper orthogonal decomposition method," *Journal of Fluids and Structures*, vol. 18, no. 2, pp. 227–250, 2003.
- [19] J. B. Rutzmoser and D. J. Rixen, "Model order reduction for geometric nonlinear structures with variable state-dependent basis," *Dynamics of Coupled Structures*, vol. 1, pp. 455–462, 2014.
- [20] S. D. Senturia, *Microsystem Design*. Norwell, MA: Kluwer Academic Publishers, 2001.
- [21] C. Grappasonni, G. Habib, T. Detroux, F. Wang, G. Kerschen, and J. S. Jensen, "Practical design of a nonlinear tuned vibration absorber," in *International Conference on Noise and Vibration Engineering*, (Leuven, Belgium), September 2014.
- [22] L. D. Lutes and S. Sarkani, *Random vibrations: analysis of structural and mechanical systems*. Butterworth-Heinemann, 2004.
- [23] M. P. Mignolet, A. G. Radu, and X. Gao, "Validation of reduced order modeling for the prediction of the response and fatigue life of panels subjected to thermo-acoustic effects," in *Proceedings of the 8th International Conference on Recent Advances in Structural Dynamics*, pp. 14–16, 2003.
- [24] R. Perez, X. Wang, A. Matney, and M. P. Mignolet, "Reduced order model for the geometric nonlinear response of complex structures," in *ASME 2012 International Design Engineering Technical Conferences and Computers and Information in Engineering Conference*, pp. 599–613, American Society of Mechanical Engineers, 2012.
- [25] M. S. Allen, R. J. Kuether, B. Deaner, and M. W. Sracic, "A numerical continuation method to compute nonlinear normal modes using modal reduction," in *53rd AIAA/ASCE/AHS/ASC Structures, Structural Dynamics, and Materials Conference*, (Honolulu, Hawaii), 2012.
- [26] R. J. Kuether, B. J. Deaner, J. J. Hollkamp, and M. S. Allen, "Evaluation of geometrically nonlinear reduced-order models with nonlinear normal modes," *AIAA Journal*, vol. 53, no. 11, pp. 3273–3285, 2015.
- [27] X. Wang, R. A. Perez, M. P. Mignolet, R. Capillon, and C. Soize, "Nonlinear reduced order modeling of complex wing models," in *Proceedings of the 54th Structures, Structural Dynamics and Materials Conference*, pp. 8–11, 2013.
- [28] J. D. Schoneman and M. S. Allen, "Investigating nonlinear modal energy transfer in a random load environment," in *Nonlinear Dynamics, Volume 1*, pp. 141–153, Springer, 2016.
- [29] R. M. Rosenberg, "Normal modes of nonlinear dual-mode systems," *Journal of Applied Mechanics*, vol. 27, no. 2, pp. 263–268, 1960.

- [30] S. Shaw and C. Pierre, “Normal modes for non-linear vibratory systems,” *Journal of sound and vibration*, vol. 164, no. 1, pp. 85–124, 1993.
- [31] G. Kerschen, M. Peeters, J. Golinval, and A. F. Vakakis, “Nonlinear normal modes, part i: A useful framework for the structural dynamicist,” *Mechanical Systems and Signal Processing*, vol. 23, no. 1, pp. 170–194, 2009.
- [32] M. Peeters, R. Viguié, G. Sérandour, G. Kerschen, and J.-C. Golinval, “Nonlinear normal modes, part ii: Toward a practical computation using numerical continuation techniques,” *Mechanical systems and signal processing*, vol. 23, no. 1, pp. 195–216, 2009.
- [33] T. Hill, A. Cammarano, S. Neild, and D. Wagg, “Interpreting the forced responses of a two-degree-of-freedom nonlinear oscillator using backbone curves,” *Journal of Sound and Vibration*, vol. 349, pp. 276–288, 2015.
- [34] J. D. Schoneman, M. S. Allen, and R. J. Kuether, “Relationships between nonlinear normal modes and response to random inputs,” *Mechanical Systems and Signal Processing*, vol. 84, Part A, pp. 184 – 199, 2017.
- [35] R. J. Kuether and M. S. Allen, “A numerical approach to directly compute nonlinear normal modes of geometrically nonlinear finite element models,” *Mechanical Systems and Signal Processing*, vol. 46, no. 1, pp. 1–15, 2014.
- [36] M. P. Castanier, Y.-C. Tan, and C. Pierre, “Characteristic constraint modes for component mode synthesis,” *AIAA journal*, vol. 39, no. 6, pp. 1182–1187, 2001.
- [37] D. J. Rixen, “A dual craig - bampton method for dynamic substructuring,” *Journal of Computational and Applied Mathematics*, vol. 168, no. 1-2, pp. 383–391, 2004.
- [38] S.-K. Hong, B. I. Epureanu, and M. P. Castanier, “Next-generation parametric reduced-order models,” *Mechanical Systems and Signal Processing*, vol. 37, no. 1, pp. 403–421, 2013.
- [39] J. J. Hollkamp and R. W. Gordon, “Reduced-order models for nonlinear response prediction: Implicit condensation and expansion,” *Journal of Sound and Vibration*, vol. 318, pp. 1139–1153, 2008.
- [40] The MathWorks, *Object-Oriented Programming in MATLAB*, 2016. Available: <http://www.mathworks.com/discovery/object-oriented-programming.html>.
- [41] A. Przekop, S. A. Rizzi, and D. S. Groen, “Nonlinear acoustic response of an aircraft fuselage sidewall structure by a reduced-order analysis,” 2006.
- [42] R. J. Kuether, *Nonlinear Modal Substructuring of Geometrically Nonlinear Finite Element Models*. PhD thesis, University of Wisconsin - Madison, 2014.
- [43] Dassault Systems Simulia Corp., *Abaqus Theory Manual*, 2012.
- [44] D. J. Rixen, “Interface reduction in the dual craig-bampton method based on dual interface modes,” in *Linking Models and Experiments, Volume 2*, pp. 311–328, Springer, 2011.
- [45] F. M. Gruber, J. B. Rutzmoser, and D. J. Rixen, “Generalized craig-bampton method using robin boundary conditions,” in *Topics in Modal Analysis & Testing, Volume 10*, pp. 111–115, Springer, 2016.